INFORMATION TO USERS

This manuscript has been reproduced from the microfilm master. UMI films the text directly from the original or copy submitted. Thus, some thesis and dissertation copies are in typewriter face, while others may be from any type of computer printer.

The quality of this reproduction is dependent upon the quality of the copy submitted. Broken or indistinct print, colored or poor quality illustrations and photographs, print bleedthrough, substandard margins, and improper alignment can adversely affect reproduction.

In the unlikely event that the author did not send UMI a complete manuscript and there are missing pages, these will be noted. Also, if unauthorized copyright material had to be removed, a note will indicate the deletion.

Oversize materials (e.g., maps, drawings, charts) are reproduced by sectioning the original, beginning at the upper left-hand corner and continuing from left to right in equal sections with small overlaps.

Photographs included in the original manuscript have been reproduced xerographically in this copy. Higher quality 6" x 9" black and white photographic prints are available for any photographs or illustrations appearing in this copy for an additional charge. Contact UMI directly to order.

ProQuest Information and Learning
300 North Zeeb Road, Ann Arbor, MI 48106-1346 USA
800-521-0600

The Evolution of Galaxies in the Hubble Deep Fields

by
Stephen Donald Jermy Gwyn
B.Sc. McGill University 1990
M.Sc. University of Victoria 1995

A Dissertation Submitted in Partial Fulfillment of the
Requirements for the Degree of

DOCTOR OF PHILOSOPHY

in the Department of Physics and Astronomy

We accept this thesis as conforming
to the required standard.

Dr. F. D. A. Hartwick, Supervisor (Department of Physics & Astronomy)

Dr. C. J. Pritchet, Departmental Member (Department of Physics & Astronomy)

Dr. D. Crampton, Departmental Member (Herzberg Institute of Astrophysics)

Dr. A. G. Brolo, Outside Member (Department of Chemistry)

Dr. S. J. Lilly, External Examiner (Herzberg Institute of Astrophysics)

Supervisor: Dr. F. D. A. Hartwick

Abstract

This thesis is a study of several aspects of the evolution of galaxies using photometric redshifts in the Hubble Deep Fields (HDF's). The photometric redshift method is used in the HDF's down to a magnitude limit of $I = 28$. The large sample and the unprecedented depth of the Hubble Deep Fields allow one to trace the evolution of several properties of galaxies from $z = 5$ to the present in a statistical manner. This thesis studies four such aspects:

1. The clustering of galaxies is examined. When the redshift distributions of the HDF-North and the HDF-South are compared, one finds a significantly greater number of galaxies around z=0.5. This suggests the presence of a structure (a very weak cluster or a very strong group) in the HDF-North.

2. The star formation rate density (SFRD) is determined by measuring the UV-luminosity density. After correcting for dust extinction, the star formation rate is found to decrease exponentially with time with an e-folding period of about 4 Gyr.

3. The difference between the the rate of declines of the B band galaxy number density and the luminosity densities are used to examine the merging history of the Universe. While the total B band luminosity density of the Universe decreases only slightly with time since $z = 5$, the number density of galaxies drops considerably more. On average, a present day galaxy is the product of ~ 3 progenitors.

4. The morphology of galaxies is quantified using a "lumpiness" parameter, L, which measures the number of local maxima in the image of a galaxy. Rest-frame B band images are made of both HDF's by k-correcting each pixel of each galaxy in the frames using the photometric redshifts of the parent galaxies. It is found that L increases with increasing absolute brightness and increasing redshift, albeit only slightly.

Examiners:

Dr. F. D. A. Hartwick, Supervisor (Department of Physics & Astronomy)

Dr. C. J. Pritchet, Departmental Member (Department of Physics & Astronomy)

Dr. D. Crampton, Departmental Member (Herzberg Institute of Astrophysics)

Dr. A. G. Brolo, Outside Member (Department of Chemistry)

Dr. S. J. Lilly, External Examiner (Herzberg Institute of Astrophysics)

Contents

List of Tables

List of Figures

Acknowledgments

Many thanks are due to my fellow graduate students, past and present, for many useful conversations, occasionally on the subject of astronomy. Kathleen, Mike, James, Eric, Dave, James (the other one), Luc and David, it's been fun. The same goes for Señor Hudson and Madame Lewis.

It would be impossible to underestimate the importance of coffee or tequila in the preparation of this thesis. I would also like to thank my muses, Messrs. Buffett, Waits, Jagger, Palmer, Knopfler and Ms. Anderson for making my office a bearable place to work.

Thanks are due to Norma Dowler who proof-read this thesis (easier to read than "Ulysses") for the modest fee of a few pecan pies.

I would like to thank His Majesty, King Robert the Bald, fourth King of the Island of Redonda, for naming me his Astronomer Royal.

This research has made use of data obtained from the Canada France Hawaii Telescope (CFHT), which is operated by the National Research Council of Canada, the Centre National de la Recherche Scientifique of France and the University of Hawaii.

Finally, I would especially like to thank my supervisor, Dr. Hartwick. Without his financial support and the innumerable discussions in which he supplied guidance, advice and an unfailing pen, this thesis would have been impossible. His patience during the past 11(!) years has been admirable.

Chapter 1

Introduction

In the beginning, according to the standard model of galaxy formation through hierarchical clustering, the Universe is filled with an almost perfectly smooth distribution of dark matter and a comparatively small amount of baryonic gas. Under the influence of gravity, this dark matter collapses into filaments which in turn collapse onto large clumps of dark matter halos. The gas cools onto these halos, forming disks. In the disks, the gas is transformed into stars. As long as there is a supply of gas, star formation continues and the galaxy will contain young, blue stars. When the gas is depleted, blown out by supernovae, or stripped by interactions with other galaxies, no more stars can form; the stellar population ages. Hot blue stars have relatively short life spans; when they die, they leave behind a population of longer-lived cool red stars. The cool stars are fainter than the hot stars; the galaxies fade as they age. The dark matter halos, and the galaxies inside them, can undergo mergers. If the merger is between two galaxies of different masses, the smaller galaxy will be absorbed by the larger galaxy, which will undergo a burst of star formation as its gas is perturbed. If the merger is between two

galaxies of roughly equal mass, both will be disrupted and will reform into an elliptical galaxy. This elliptical galaxy can then accrete other, smaller galaxies, becoming a bulge in the centre of disk galaxy.

The Hubble Deep Fields are the deepest optical images of the sky yet obtained. Observed with Hubble Space Telescope with week-long exposures, they probe the Universe to the point where the Universe was only a tenth its present age. Because the observations were made from space, beyond the distorting effects of the atmosphere, the quality of the images of the galaxies is extraordinary. Thus, the Hubble Deep Fields are the ideal places in which to study the evolution of galaxies.

The Hubble Deep Fields (HDF's) are so deep in fact that most of the galaxies are too faint to be observed spectroscopically with current telescopes. Only the brightest 10% of the galaxies have spectroscopic redshifts. To learn more about the remaining 90%, one must use photometric redshifts. Indeed, the HDF's and photometric redshifts seem made for each other. While the Hubble Deep Fields contain galaxies at redshifts of $z = 5$, most of these galaxies cannot be observed spectroscopically. Hence, photometric redshifts are needed to study the Hubble Deep Fields. On the other hand, for photometric redshifts to be feasible, one needs an imaging survey in at least four passbands. Further, for photometric redshifts to be useful, this survey must ne largely unstudied spectroscopically. The HDF's meet both these criteria. This thesis is a study of galaxy evolution in the Hubble Deep Fields using photometric redshifts.

Rather than observing narrow spectral features of galaxy spectra, such as lines, the photometric redshift technique concentrates on broad features,

such as the 4000Å break and the overall shape of a spectrum. In this method, the photometry of observed galaxies is converted into low resolution spectral energy distributions (SED's). Redshifts are determined by comparing these SED's to redshifted template galaxy spectra.

The chief advantage of using the photometric redshift technique is speed. In spectroscopy, the light from the galaxy is separated into narrow wavelength bins a few angstroms across. Each bin then receives only a small fraction of the total light from the galaxy. Hence, to achieve a sufficiently high signal-to-noise ratio in each bin, long integration times are required. For photometry, however the bins are much larger, typically 1000Å wide. It requires only a short exposure time to reach the same signal-to-noise ratio. For very faint objects, the exposure times required for spectroscopic observation rapidly become prohibitive. It is possible to measure photometric redshifts in the Hubble Deep Field down to $I_{ST} = 28$.[1] It would take years to obtain spectroscopic redshifts for the same galaxies using Keck, currently the largest telescope in the world.

The main disadvantage of using photometric redshifts is that they are less precise. The uncertainties of spectroscopically measured redshifts are on the order of $\Delta z = \pm 0.001$, while photometric redshift uncertainties are typically $\Delta z = \pm 0.1$. For studying individual galaxies, this level of uncertainty is generally too large. For determining properties of large numbers of galaxies in a statistical manner, however, this uncertainty is quite acceptable.

[1] for simplicity, U_{ST},B_{ST},R_{ST} and I_{ST} will be used to denote magnitudes in the F300W, F450W, F606W and F814W bands respectively. The ST zero-point system is used unless otherwise specified.

To measure photometric redshifts for galaxies, one must first obtain photometry for those galaxies. In particular, accurate colours must be determined. Chapter 2 describes the detection and photometry of galaxies in the HDF images. A sample of 1694 galaxies, complete down to $I_{ST} = 28$ is generated.

Chapter 3 gives a history of the various photometric redshift techniques used in the past and describes in detail the photometric redshift technique used in this thesis. Applying this technique to the photometric sample, we obtain a catalog of galaxies with positions, colours and redshifts. This sample is then used to study the evolution from z=5 to z=0 of four properties of galaxies: clustering, star formation rates, merging and morphologies.

The clustering of galaxies depends on how the dark matter halos are clustered, which in turns depends on the details of how the halos form and evolve. Chapter 4 discusses the clustering of galaxies as measured by the two-point projected spatial correlation function. Different hierarchical models make different predictions about the evolution of the clustering of galaxies as a function of redshift. Although the solid angle subtended by the Hubble Deep Fields is somewhat too small to give very stringent constraints on these models, the difference in number counts and clustering from North to South allows one to say something more definite about the variations in spatial densities of galaxies.

In the last few years, there has been great interest in the evolution of the global star formation rate. Star formation rate density (SFRD) measures the mass of stars created per time interval per unit volume of space, in units of $M_{\odot}yr^{-1}Mpc^{-3}$. In general, the star formation is considered to have been more

rapid in the past. The exact details of its evolution with redshift, however, are the subject of debate. Although most astronomers believe that, at low redshift, the star formation rate density is steadily increasing with redshift from $z = 0$ to $z = 1$, there is some discussion as to the exact rate (Lilly *et al.*, 1996; Cowie *et al.*, 1999, are representative of the two opinions). At high redshift, some (Madau *et al.*, 1996, for example) hold that the SFRD peaks at around $z \sim 1.5$ and declines at higher redshift, while others (Steidel *et al.*, 1999) maintain it remains relatively constant. A complicating factor is the presence of dust in galaxies, which can cause the SFRD to be underestimated by a factor of five. Numerous surveys at different redshifts, using different techniques have been used to measure the SFRD of the Universe. Some of these surveys account for dust and some of which do not. Chapter 5 presents measurements of the star formation rate density over the entire redshift range from $z = 0$ to $z = 4.5$ using a single technique and accounting for dust.

Chapter 6 investigates the merger history of galaxies. It is clear that some, if not most galaxies have undergone mergers in the past. The question is: how many mergers? One approach to answer this question is to look at galaxies and determine what fraction are currently undergoing mergers. One can look for galaxies that are clearly undergoing mergers (disrupted morphologies, tidal tails) or look for galaxies that are close to each other in space, and will likely merge in the near future. Patton (1999) looked at close pairs in the CNOC1 [2] (Yee *et al.*, 1996) and CNOC2 (Yee *et al.*, 2000) surveys and determined the merger rate as a function of redshift out to $z = 0.5$. Another approach is look at the number of galaxies at some

[2]Canadian Network for Observational Cosmology

point in the past and compare it to the number of galaxies at the present. Simplistically, if there is a large number of mergers, there will be significant drop in the number of galaxies. Although there are a number of complicating factors, this approach can be used to determine the overall merger rate.

When one looks at the galaxies in the Hubble Deep Fields, one sees a number of well-formed spiral and regular elliptical galaxies. However, one's eye is caught by the large number of galaxies with very disturbed morphologies, the so-called "train wrecks" and other peculiar objects. When observed spectroscopically, these galaxies are often found to be at high redshift. Therefore, the naive conclusion is that higher redshift galaxies have increasingly irregular morphologies. The morphology of galaxies in the Hubble Deep Field North was studied by Abraham *et al.* (1996) using quantitative measures of morphology as well as visual classifications. Abraham's measure of asymmetry, A, is determined by rotating the image of a galaxy by 180° and subtracting the rotated image from the original. A is defined as half the ratio of the absolute value of the total flux in the self-subtracted image to the total flux in the original image. His measure of central concentration, C is the inverse ratio of the flux within an outer elliptical aperture (whose radius is determined from the intensity-weighted second-order image moments) and the flux within an inner elliptical aperture (whose radius is 0.3 that of the outer). While these parameters can be measured down to $I_{ST} = 24$ in the Hubble Deep Field, fainter galaxies cannot be so classified. Lowering the signal-to-noise ratio of the images of galaxies drives the asymmetry to $A = 0$ and causes the central concentration measurements to be indistinguishable from the seeing disk. Chapter 7 introduces another quantitative measure

of morphology. L, which measures the "lumpiness" of galaxy images, which can be measured to fainter magnitudes. The evolution of L with redshift is traced.

Chapter 2

The Hubble Deep Fields

This chapter describes the methods used for detection and photometry of galaxies in the Hubble Deep Fields, and the definition of the galaxy sample that will be used for the remainder of this thesis.

2.1 Description of the Hubble Deep Fields

The Hubble Deep Fields form the observational basis for this thesis. The Hubble Deep Field North (HDFN) was observed in December 1995 using the Wide Field Planetary Camera (WFPC) on the Hubble Space Telescope. It is centred at Right Ascension $12^h36^m49^s.4$, Declination $+62°12'58''.00$ in J2000.0 coordinates. The field was chosen to be a typical "blank" bit of sky. The Hubble Deep Field South (HDFS) was observed in September/October 1998. Instead of an arbitrary pointing, the area of the sky in the vicinity of the quasar J2233-606 was observed. Several HST instruments were used. The Space Telescope Imaging Spectrograph (STIS) was pointed directly at the quasar while the WFPC and the Near Infrared Camera and Multi-Object

Spectrograph (NICMOS) were observed in parallel on nearby areas of the sky. The HDFS WFPC field is centred at $22^h32^m56^s.22$, -62°33′02″.69 (J2000.0).

Both fields were imaged in four HST filters: F300W, F450W, F606W and F814W. The F300W lies about 500Å to the blue of the Johnson U band. The other three filters are roughly equivalent to the BRI bandpasses respectively. For simplicity, the F300W, F450W, F606W and F814W filters will be referred to as the $UBRI$ filters in this thesis. The responses of these filters are shown in Figure 2.1. The four images of each field are registered to very high accuracy: ~ 0.1 pixels.

The Hubble Deep Fields have been imaged at many other wavelengths from X-ray to radio. Indeed, the HDFN in particular is probably the most carefully studied part of the sky. It has been imaged in X-rays, the UV-optical, infrared, sub-mm, and radio bands. Of potential interest for photometric redshift purposes are the near infrared images. Unfortunately, the two space-based NICMOS images are not publicly available except as HST archival images, which require a degree of further processing before they can be used. Also, the images either do not cover the entire field (Thompson *et al.*, 1999) or are too shallow (Dickinson, 2000). The same can be said of the ground-based images (Hogg *et al.*, 1997; Dickinson *et al.*, 1998; Hogg *et al.*, 1999). Further, in order to compute consistent photometry for both lower resolution infrared images and the higher resolution optical images, it would be necessary to degrade the seeing of the later. The Hubble Deep Field South has also been imaged in other bands (da Costa *et al.*, 1998). However the only imaging data common to both the HDFN and HDFS of identical bandpasses and depth is the $UBRI$ imaging. Therefore, the present analysis

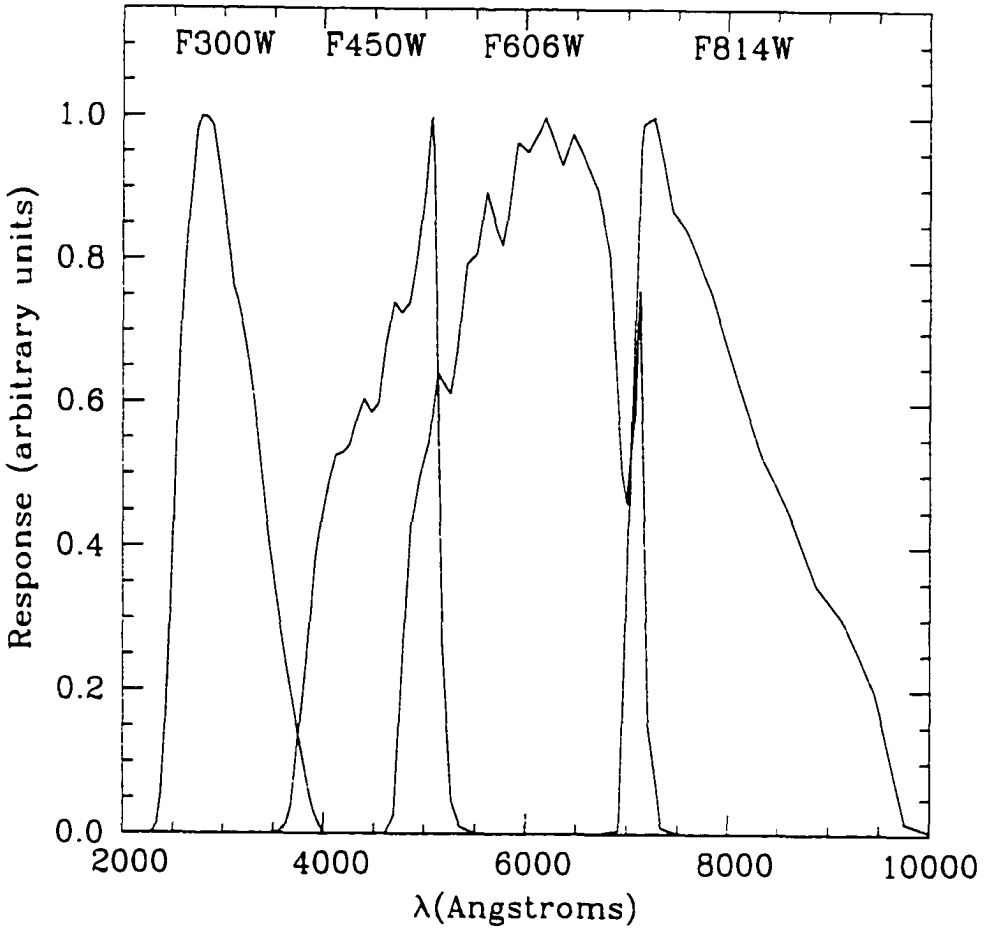

Figure 2.1: Filters used in the HDF's

will be confined to just the *UBRI* data from HST.

Not having infrared data, while slightly vexing, is no great loss. Infrared data is both a help and a hindrance when measuring photometric redshifts. On the plus side, it does extend the wavelength coverage of SED. On the minus side, spectral templates for the rest frame infrared are rare and not reliable. In a blind test of photometric redshifts organized by Hogg *et al.* (1998), the inclusion of infrared data was not found to improve the accuracy of the photometric redshifts significantly.

The HDFN and the HDFS are both freely available electronically at `http://www.stsci.edu/ftp/science/hdf/archive/mosaics.html` and `http://www.stsci.edu/ftp/science/hdfsouth/reduc_wfpc2.html` respectively. The images are available as mosaics of the three Wide Field images plus the smaller Planetary Camera image. The numerous images that make the final mosaic were combined with the "drizzle" algorithm (Fruchter & Hook, 1998); the final pixels are 0.03985 arcseconds on a side. The mosaics measure 4096 × 4096 pixels for the HDFN and 4096 × 4600 pixels for the HDFS. The images as distributed are sky-subtracted. They are scaled in intensity to 1 electron per second; that is to say, they are scaled as if the total exposure had been one second. To return them to the original scale, the images were multiplied by the exposure times given in Table 2.1 which also lists the ST magnitude zeropoint for each image.

Table 2.1: List of observations

Field	Filter	Exposure Time	ST magnitude zeropoint
HDFN	F300W	153700	19.47
HDFN	F450W	120600	21.52
HDFN	F606W	109050	23.21
HDFN	F814W	123600	22.90
HDFS	F300W	140185	19.45
HDFS	F450W	100950	21.53
HDFS	F606W	81275	23.21
HDFS	F814W	100300	22.91

2.2 Detection

The SExtractor package (Bertin & Arnouts, 1996) was used to detect the galaxies in the images and to set up segmentation maps. This package cannot be praised loudly enough. It is easy to download and install on any UNIX (or similar) system. It takes up little disk space. It is easy to use: parameters can be fed to it via default files, command-specific files or on the command line. It is quite fast. It is very well documented. Its main defect is its name, which is short for Source Extractor: searching for documentation for the package usually leads to web sites whose contents have little to do with astronomy.

When searching for galaxies, SExtractor first convolves the image in question with a small filter that can be specified by the user. For this work

the default filter:

$$\begin{bmatrix} 1 & 2 & 1 \\ 2 & 4 & 2 \\ 1 & 2 & 1 \end{bmatrix}$$

was used. Convolving like this improves the signal-to-noise ratio for detection. SExtractor then scans the convolved image, looking for a certain number of contiguous pixels above a certain threshold. In this case, the detection threshold was set to 3 times the standard deviation of the background and the number of pixels was 5. This 3-sigma detection limit works out to a surface brightness threshold of 26.40 magnitudes per square arcsecond in I_{ST}. SExtractor then assigns all pixels contiguous to the object.

The next step is to deblend the galaxies. This is where SExtractor really shines. For each object it detects, it splits the brightness profile into a number of levels, from the peak flux down to the detection threshold. SExtractor then searches downwards through the thresholds looking for secondary peaks in the 2-dimensional brightness distribution. If it finds any, it has to make a decision whether to split the object in two or more sub-objects. The decision to split or not is made using the following criteria: (A) Is the ratio of total brightness in the prospective sub-object to the total brightness of the original object greater than a certain contrast parameter? (B) Is condition (A) true for at least one more sub-object (potentially, the rest of the object)? If both (A) and (B) are true, then the object is split. Contiguous pixels below the current threshold are reassigned to the appropriate sub-object.

The relevant parameters for this multi-thresholding are the number of levels (in this case, 32) the way in which the different levels are spaced (in this case, exponentially) and the contrast parameter (in this case, 0.005).

Bertin & Arnouts, (1996) recommend these values as being the most useful in general. In fact, the exact values are not critical. Changing the number of sub-thresholds by a factor of 2 either way does not make a noticeable difference in the segmentation image; neither does changing the contrast parameter by 50%.

This automatic splitting works remarkably well. Only in the largest, brightest and lumpiest (Sc types and later) galaxies does it fail. Even in these relatively difficult objects, it only fails occasionally. These relatively few cases are quite obvious and are easily corrected by hand. To be on the safe side, all the galaxies in the sample were carefully scrutinized individually by eye to see if any had been split when they should have been merged or merged when they should have been split.

SExtractor produces a catalog with x and y positions and photometry. It also produces a segmentation image. This FITS image is the same size as the original image. It has zeros everywhere that the original image had blank sky. Within the bounds of each object (its "segment"), the pixels have a value equal to the ID number corresponding to the relevant object in the catalog. For an uncrowded object, this will be all the pixels above the isophotal threshold. For a crowded object, the segment will be all the pixels above the isophotal threshold that were not assigned to another object during the deblending procedure. The segmentation image makes it possible to see which pixels were assigned to which object. This is a very interesting and useful diagnostic in its own right, but has other uses for further photometry as will be discussed in the next section. For an example of a segmentation image, see Figure 2.2.

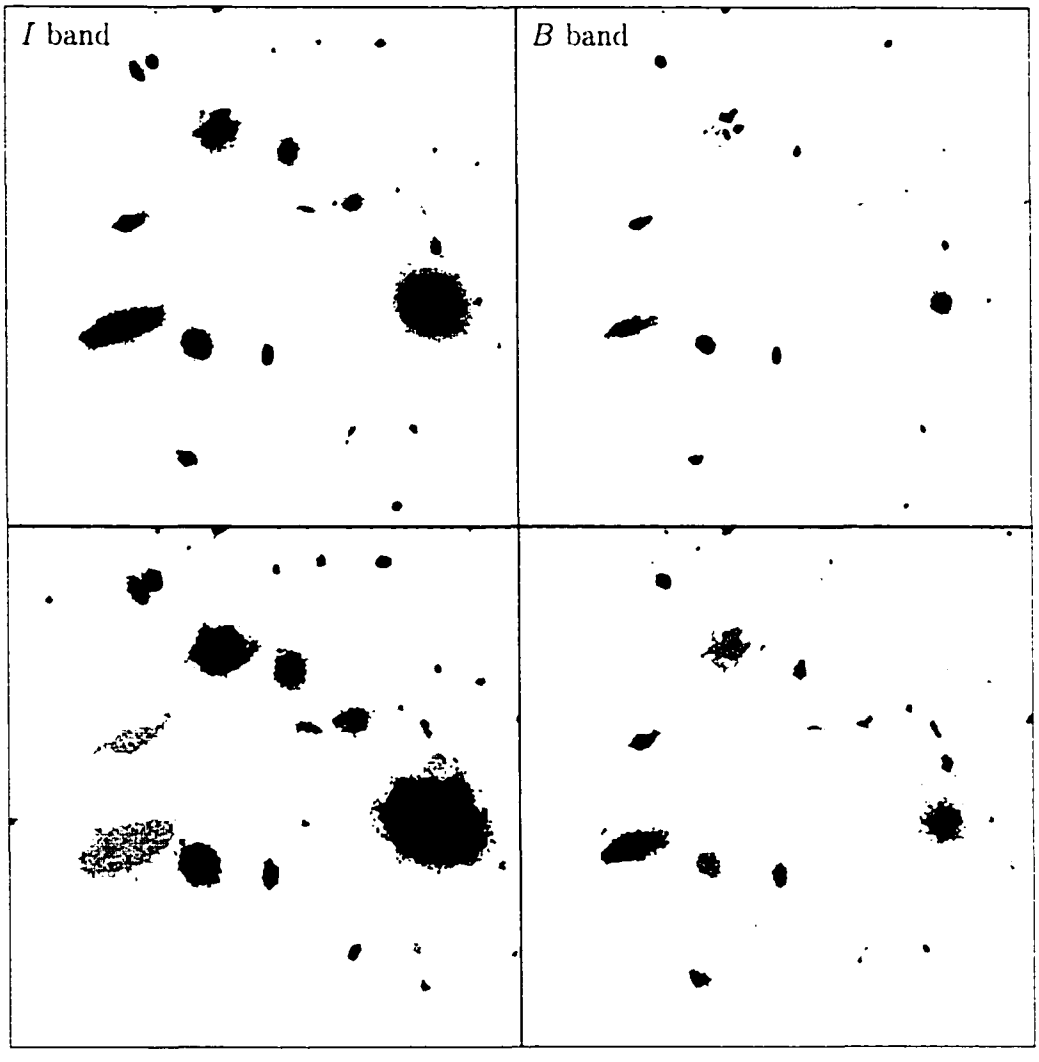

Figure 2.2: Segmentation images in different bands. The upper panels show a subsection of the HDFN in both the I and B bands (left and right respectively). The lower panels show the segmentation image produced by SExtractor for the same subsection. Different shades of grey are used to distinguish different objects. Note the substantial differences in the segmentation image from band to band.

Because of the dithering[1] during the observations, some sections of the HDF images have substantially lower exposure times than the bulk of the image. These sections are located around the edges of the images. Because of the increase in noise, there are many spurious detections in these areas. There is also the occasional legitimate detection, usually a relatively bright object. Rather than try to sort the spurious from the legitimate objects, the edges of the images were masked off. All objects whose centres lay within the masked off areas were rejected.

2.3 Photometry

There are several methods for doing galaxy photometry. The methods resemble each other in as much as they all have some algorithm or rule to decide which pixels of a galaxy image are associated with the galaxy, and then sum the light from these pixels to produce a magnitude. The pixels are all given equal weight, unlike many techniques used in stellar photometry. The methods differ mainly by the way in which the pixels associated with the object are chosen:

- Fixed aperture photometry: This is by far the simplest method. All the pixels within a certain circular radius are used. Of course, not all galaxies are the same size, so fixed aperture photometry will measure a different fraction of the total light from each galaxy. If the aperture radius is too small with respect to the size of the galaxy, some unknown

[1] Dithering: small shifts in the pointing of the telescope to ensure that objects do not always fall on the same pixels of the detector.

light from the galaxy will be lost, making it impossible measure total magnitudes. If the aperture is too large, a fair amount of sky will be included, degrading the signal-to-noise ratio of the photometry.

- Automatic aperture (Kron) photometry: One can match the size of the aperture to the size of the galaxy. The size of the galaxy, r_1, is measured using the Kron algorithm (Kron, 1980):

$$r_1 = \frac{\sum rI(r)}{\sum I(r)} \tag{2.1}$$

  One can then use a circular aperture of radius kr_1, with k some constant, generally 2 or an elliptical aperture with principal axes ϵkr_1 and kr_1/ϵ (where ϵ is the ellipticity of the galaxy) to do the photometry. One can measure accurate total magnitudes with this method.

- Isophotal photometry: In this method, the aperture is not circular, nor any regular geometric shape. It is the set of all pixels associated with a galaxy whose brightness is greater than some threshold. The light from each and every pixel likely to contribute substantially to the total is included. Conversely, no (or at least very few) pixels containing only sky are included.

- Corrected isophotal photometry: Straight isophotal photometry misses a fraction of the light from each galaxy. It depends on the surface brightness of the galaxy: the fraction of light missed is larger for fainter galaxies. However a correction factor, η, can be computed (to second

order) following Maddox *et al.* (1990):

$$\eta \simeq 1 - 0.1961 \left(\frac{At}{I_{iso}}\right) - 0.7512 \left(\frac{At}{I_{iso}}\right)^2 \qquad (2.2)$$

where A is the area within the isophote, t is the isophotal threshold, and I_{iso} is the flux within the isophote.

SExtractor can compute photometry via all these methods. It also can compute a "best" magnitude (known, aptly enough, as `MAG_BEST` in SExtractor terminology) which is either a corrected isophotal magnitude (in the case where a galaxy may be subjected to crowding) or a Kron magnitude (when crowding is not a problem). This "best" magnitude is a robust total magnitude.

The question is: which method of doing galaxy photometry is best for the problem at hand? When measuring photometric redshifts, getting reliable colours is key: systematic errors in the colours should be minimized. The exact same portion of the sky should be measured in all bands. For this purpose, small fixed apertures are ideal. On the other hand, the photometry is also used for generating luminosity functions and k-corrections. For this, accurate total magnitudes are necessary. This is particularly true for the I band, since it is in that band the final galaxy sample will be defined. Small fixed aperture magnitudes do not give good total magnitudes. Isophotal magnitudes are subject to $(1+z)^4$ surface brightness dimming effects which makes measuring luminosity functions by the $1/V_{max}$ method quite complicated.

One can, in principle, measure total magnitudes by the corrected isophotal method or the Kron method in all bands. However, the isophotes and

Kron radii in some bands may be considerably different than in others. This can be clearly seen when comparing the image and segmentation map of the B band image to their counterparts in I as shown in Figure 2.2. Because of these differences, the colours may not be measured on exactly the same parts of the sky, which could lead to inaccurate colours.

The best compromise is to:

- determine the isophote in the I band.
- do photometry in all bands through the I isophote
- determine total magnitudes in the I band by the corrected isophotal method or the Kron method (SExtractor's `MAG_BEST`)
- correct the photometry in all bands by the difference for the I band between `MAG_BEST` and the isophotal photometry.

This procedure has many advantages. The colours are measured consistently, through identical — if irregularly shaped — apertures; hence they are appropriate for photometric redshifts. The magnitudes are total magnitudes, appropriate for sample selection and the measurement of luminosity functions. The correction from isophotal to total magnitudes is small, typically less than 0.1 mag. The only disadvantage is that the I isophotes are usually larger than isophotes in other bands. This means that more sky pixels are included in the other bands, increasing the noise. However, the increase in random errors is more than offset by the decrease in systematic errors.

SExtractor, although admirable in many respects, has one shortcoming: it cannot process many images simultaneously. This makes multi-colour

photometry following the method described above a bit problematic. To this end, a new program[2] was written. It performs photometry on all four images simultaneously, through identical apertures. It takes as input data the object catalog and the segmentation image produced by SExtractor, as well as all four *UBRI* data images. For each object in the catalog, the program first determines which segment to use based on the x and y coordinates from the catalog. Next, the program sums all the flux in that segment in each of the four bands. (Since the segmentation image reflects both the isophotes and the deblending described in the previous section this is effectively "deblended isophotal" photometry.) This total flux in each band is converted into a magnitude in the usual way: magnitude= $-2.5\log(\text{Flux})$. The magnitude is corrected for the zero-point and the exposure time. The magnitude in each band is further corrected by the difference between the isophotal magnitude and the total (`MAG_BEST`) magnitude in the *I* band. Since the images are sky-subtracted as part of the HST pipeline, no correction for sky background is made. This method is made easier by the fact the HDF images in each band are registered to very high accuracy.

The uncertainty in the total flux, σ_F, is calculated as follows:

$$\sigma_F = \sqrt{F + n_{pix}\sigma_{sky}^2} \tag{2.3}$$

where F is the total flux in the aperture, and n_{pix} is the number of pixels in the aperture. The variance in the sky, σ_{sky}^2, is calculated once per image. It is measured in 20 or so blank sections of the sky, each of which is 50×50

[2]for those interested in such details, the program was written in FORTRAN, using the FITSIO libraries

pixels. The uncertainty in the corresponding magnitude, σ_m, is given by:

$$\sigma_m = 2.5 \log\left(1 + \frac{\sigma_F}{F}\right) \tag{2.4}$$

The method described above was applied to the Hubble Deep Fields. The results are shown in Figures 2.3 and 2.4. Figure 2.3 shows the number counts in all four bands. Figure 2.4 shows the number counts in the I band split by field. Note the difference in the number counts between the HDF North and the HDF South. This difference will be examined more closely in Chapter 4.

2.4 The sample

Having measured photometry for the galaxies, the next step is to construct a well-defined sample of galaxies. Photometric redshifts will be calculated for the galaxies in this sample. Therefore all the galaxies must be observed in at least 3 bands. These photometric redshifts will be used to generate luminosity functions, V/V_{max} statistics and the like. Ideally, then, the sample must be complete down to a magnitude limit, with little or no constraints from surface brightness. The magnitude limit that was chosen is I_{ST} <28. I=28 in the ST system is equivalent to I=27.2 in the AB system and I=26.8 in the Vega system.

Figure 2.5 shows I band number counts for a variety of criteria. The heavy solid line shows the total counts. The light lines show the I counts for the set of galaxies detected in all bands (dashed) in at least the B, R and I bands (dotted) and just the R and I bands (solid). All galaxies detected in

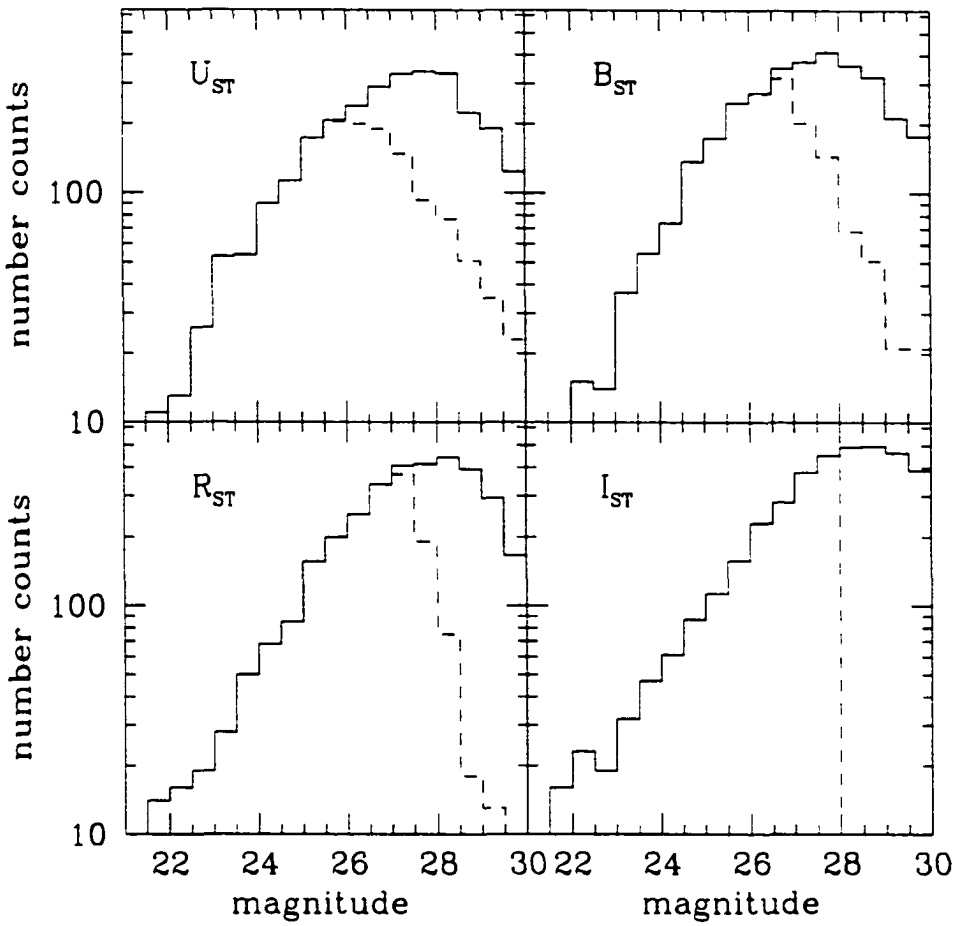

Figure 2.3: Total number counts for the HDFN and HDFS in the $UBRI$ bands. The solid lines show the total number counts. The dashed lines show the number counts for objects with $I < 28$. The magnitude scale is the ST system for all bands.

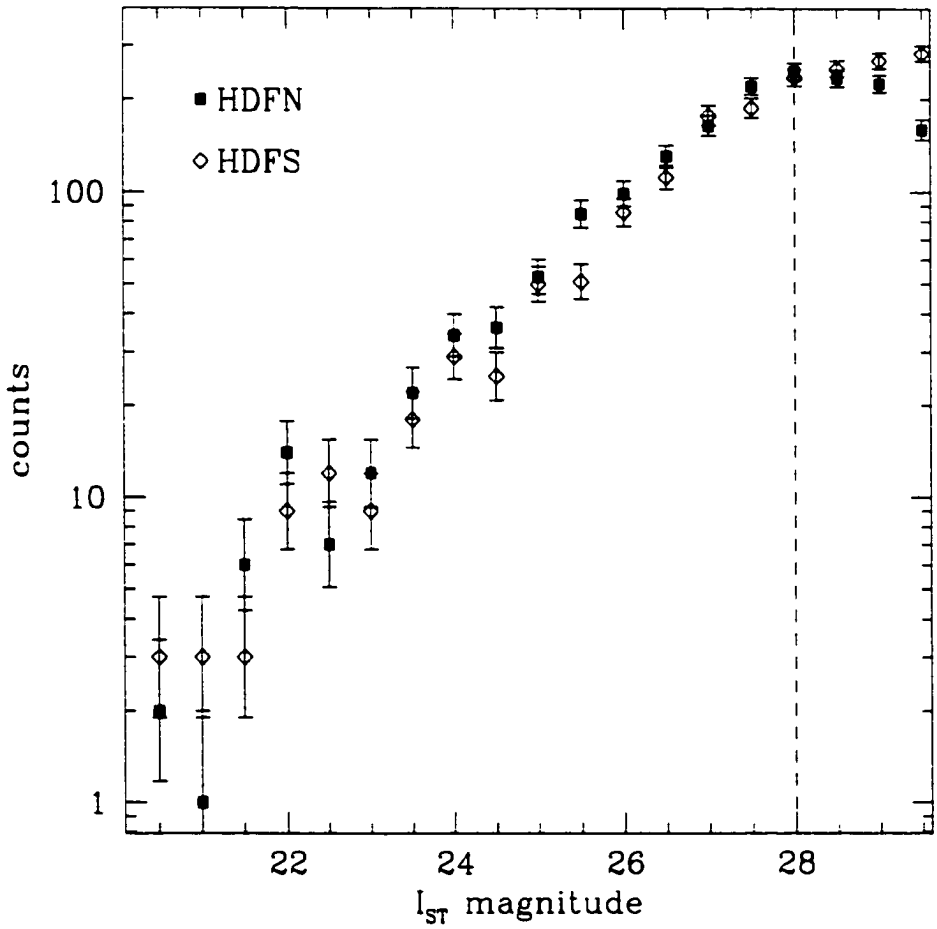

Figure 2.4: *I* band number counts for the HDFN (solid points) and the HDFS (open points). The error bars reflect Poisson statistics in each bin. The dashed vertical line shows the cutoff for the sample.

I are also detected in R down to $I_{ST} = 29$: the light solid line and the heavy solid line are distinguishable only in the two faintest bins. One also sees from the figure that all but 1% of the galaxies brighter than $I_{ST} < 28$ are detected in at least three bands. All (with one exception) of the small fraction that do not have B detections can reliably assigned redshifts of $z > 3.5$ based on the lower limits of their $B - R$ colours: that is to say, they are B-dropouts. A larger fraction of galaxies are not detected in U. This is partially because the U image is not as deep as the BRI images. However, another fraction of the galaxies with no U detections are *bona fide* high redshift U-dropouts. In either case, photometric redshifts can be measured for the entire sample.

The next step is to show that the sample is complete, that is to say, that there is no significant population galaxies down to the limiting magnitude that are missed by the detection algorithm. For this, simulations were used. A sub-section containing no border effects or large bright galaxies was cut out of the I image of the HDFN. Galaxies were then added at random to this image. These simulated galaxies had exponential profiles with various total magnitudes I_{tot} and central surface brightnesses, μ_I. Setting the parameters exactly as in the original extraction as described above, SExtractor was run on the image with extra galaxies. The fraction of artificial galaxies recovered gives the completeness as a function central surface brightness and total magnitude. In each trial, 10 galaxies were added to the image. For each combination of I_{tot} and μ_I, 100 trials were made. The test was done at 0.1 magnitude intervals of I_{tot} and μ_I

The results are shown in Figure 2.6. The dots show the total I magnitude and peak surface brightness of all the galaxies detected in the Hubble Deep

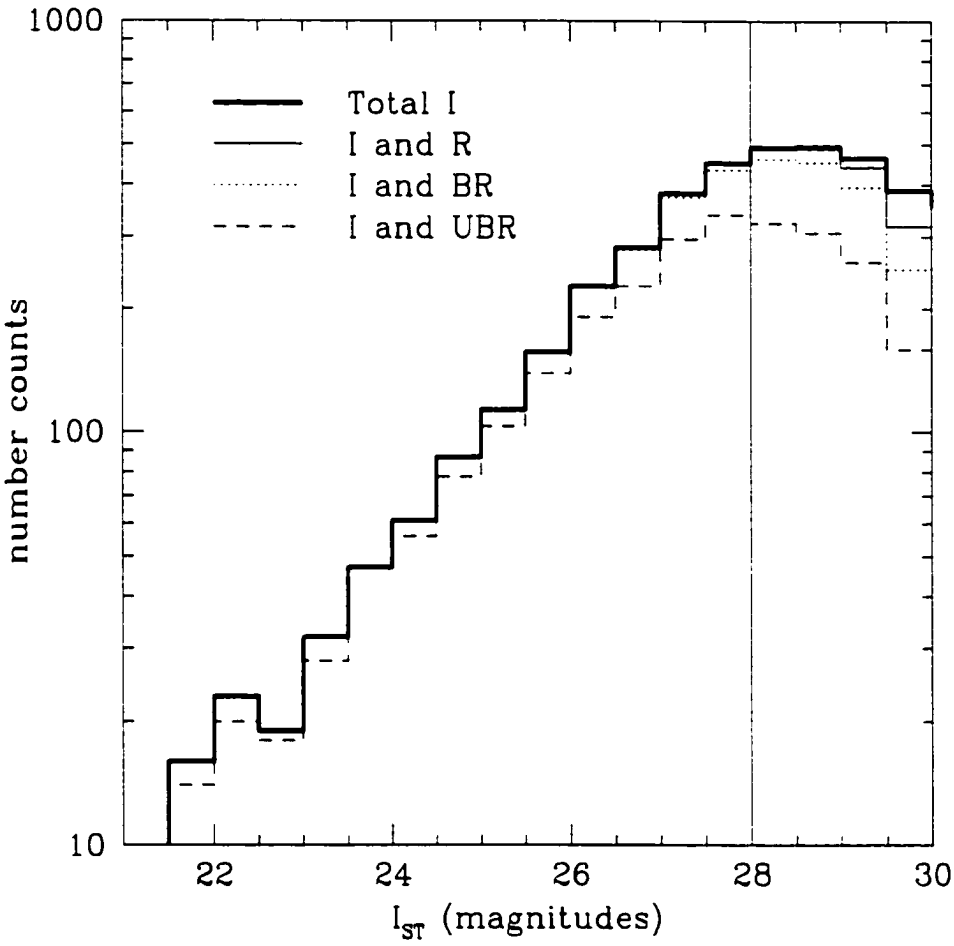

Figure 2.5: Photometric completeness limits. The light lines show the I number counts including only those galaxies which were detected in other bands. The dashed line shows the I counts for galaxies detected in all bands. The dotted line shows the I counts for galaxies detected in at least the BRI bands. The light solid line shows the I counts for galaxies detected in at least the RI bands. The heavy solid line shows the total I band number counts, regardless of whether those galaxies were detected in other bands: it can only be distinguished from the I plus R counts in the two faintest bins. The vertical line shows the I_{ST}=28 cutoff of the sample.

Fields. The labeled lines indicate the 90%, 70%, 50%, 30% and 10% completeness limits of the sample. The completeness reflects two things: First, there is the chance of recovering a faint galaxy from the noise. If a galaxy has either a low surface brightness or a faint total magnitude, it will be missed. In particular, if its peak surface brightness is below the detection threshold of 26.4 mag arcsec^{-2}, it will always be missed. Second, there are the effects of crowding. Even bright galaxies can be missed if they are superimposed on other objects. This occurs roughly 2% of the time. As can be seen from Figure 2.6, the vast majority of the observed objects with $I_{ST} > 28$ lie in an area that is at least 90% complete. Four objects lie near but slightly above the 90% contour line. It can be seen from Figure 2.6 (and will be further shown in Chap. 5) that surface brightness effects play only a minor role.

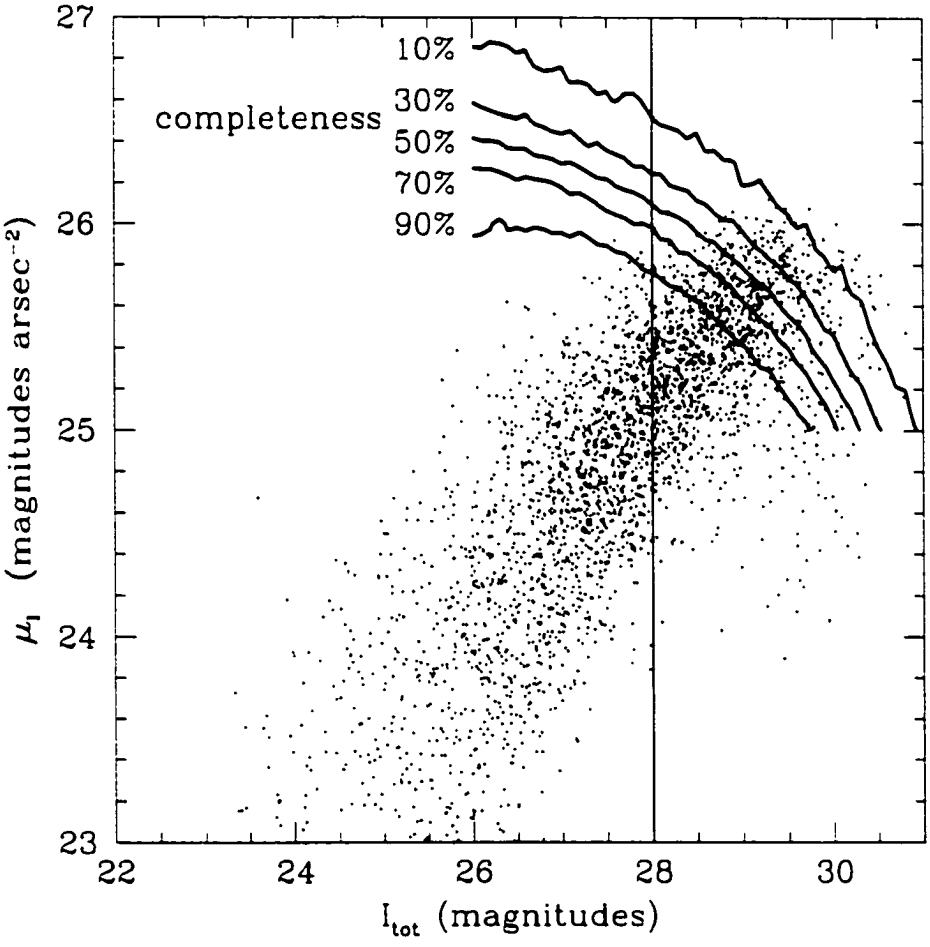

Figure 2.6: Surface brightness completeness limits. The dots show the total I magnitude and peak surface brightness of all the galaxies detected in the Hubble Deep Fields. The labeled lines indicate the various completeness limits of the sample. The vertical line shows the magnitude cut for the sample.

Chapter 3

Photometric Redshifts

This chapter first examines the photometric redshift technique from a historical perspective, with a brief description of every method used so far. For this thesis, the template fitting method of photometric redshifts was used; therefore this technique is described in much greater detail. The Hubble Deep Fields present a challange for photometric redshifts. The redshift range is very large. At high redshift, the templates must be extended further into the UV than observations have been made locally. Further, although the BRI images are of comparable depth, the U image is somewhat shallower. It is important to distinguish between genuine U dropout/Lyman break galaxies and nearer galaxies that are intrinsically faint in the U band. The modifications to the basic technique that are needed to apply it to the Hubble Deep Field data are discussed. Finally, the method is applied to the sample defined in the previous chapter, and the photometric redshift distribution down to $I_{ST} = 28$ is presented.

3.1 A brief history of photometric redshifts

The concept of photometric redshifts is not new: it was first developed by Baum (1957; 1962). But with the advent of the Hubble Deep Field (Williams *et al.*, 1996), there has been a recent revival in interest in photometric redshifts. Indeed, there have been more papers dealing with photometric redshifts since 1996 (Gwyn & Hartwick, 1996; Lanzetta *et al.*, 1996; Mobasher *et al.*, 1996; Sawicki *et al.*, 1997; Cowie *et al.*, 1996; Madau *et al.*, 1996; SubbaRao *et al.*, 1996; Pelló *et al.*, 1996; Steidel *et al.*, 1996a; Steidel *et al.*, 1996b; Belloni & Röser, 1996; Benítez, 1999; Brunner *et al.*, 1997; Connolly *et al.*, 1997; Furusawa *et al.*, 1999; Giallongo *et al.*, 1998; Hudson *et al.*, 1998; Hogg *et al.*, 1998; Liu & Green, 1998; Wang *et al.*, 1998, among others) than in the previous 35 years (Baum, 1962; Koo, 1985; Ellis *et al.*, 1985; Loh & Spillar, 1986b; Loh & Spillar, 1986a; MacLaren *et al.*, 1988; Rixon *et al.*, 1991; Connolly *et al.*, 1995a). Recently an entire conference (Weymann *et al.*, 1999) has been devoted to photometric redshifts, something that would have been unheard of five years ago.

This section will outline a brief history of photometric redshifts. The list of papers reviewed here is not exhaustive; however, it does cover all of the techniques so far developed.

3.1.1 Direct shift measurement

Baum was the first to propose (1957) and then develop (1962) a technique for measuring redshifts photometrically. He used a photoelectric photometer and 9 bandpasses spanning the spectrum from 3730Å to 9875Å. With

this system he observed the spectral energy distribution (SED) of 6 bright elliptical galaxies in the Virgo cluster. He then observed 3 elliptical galaxies in another cluster (Cl0925+2044, also known as Abell 0801). By plotting the average SED of the Virgo galaxies and the average SED of the Cl0925 galaxies on the same graph using a logarithmic wavelength scale, he was able to measure the displacement between the two energy distributions, and hence the redshift of the second cluster. His redshift value of $z = 0.19$ agreed closely with the known spectroscopic value of $z = 0.192$, so he extended his technique to a handful of clusters of then unknown redshifts out to maximum redshift of $z = 0.46$. He then derived a very rough value of Ω_0. Baum's technique was fairly accurate, but because of its dependence on a large 4000Å break spectral feature, it could only work on elliptical galaxies.

3.1.2 Colour-colour diagrams

Koo (1985) followed a different approach. First, he used photographic plates instead of a photometer, making it possible to measure photometric redshifts for a large number of galaxies simultaneously. Second, instead of using 9 filters he used only 4: $UJFN$ ($\equiv UB_JR_FI_N$). Third, instead of using an empirical spectral energy distribution, he used the theoretical Bruzual (1983, among others) no-evolution models for all galaxy types.

The most important difference, however, was the way the colours were used. Instead of converting the photometric colours into a kind of low resolution spectrum, he converted the Bruzual templates into colours, and plotted lines of constant redshift and varying spectral type, known as *iso-z* lines, on a colour-colour diagram. Finding that the most normal colour-colour diagrams

(e.g. $U - J$ versus $J - F$ and $J - F$ versus $F - N$) were degenerate in a range of redshifts, he invented what he called *colour-shape diagrams*. The *shape* measured whether the SED turned up or down at both ends, that is, whether the spectrum was bowl shaped or humped. Another way to put it is that the colour measured the first derivative with respect to wavelength of the spectrum and the shape measured the second derivative. For colour he used either $2U - 2F$ or $U + J - F - N$, both of which span a large wavelength range. For shape, he used either $-U + 2J - F$ or $-U + J + F - N$. Following this method to measure the redshift of a galaxy, Koo calculated the colour and the shape from the $UJFN$ magnitudes and plotted them on the colour-shape diagram. The redshift of the galaxy was then found by finding the *iso-z* line closest to the point representing the galaxy. Koo tested this method on a sample of 100 galaxies with known spectroscopic redshifts ranging from $z = .025$ to $z = .700$.

This method is similar to that used by Pelló *et al.* (1996) and Miralles, Pelló & Le Borgne (1996). They used the *BRIJK* colours of galaxies to determine "permitted redshifts" in the following manner: The colours of galaxies are plotted as a function of redshift from the Bruzual & Charlot (1993) models. Each available colour (with its associated uncertainty) of a galaxy defines a "permitted" redshift range on the corresponding colour-redshift diagram. The intersection of the permitted redshift ranges for all the colours determines the redshift. This amounts to a colour-colour-colour-colour diagram (4 dimensions instead of 2). This method was used by Pelló *et al.* (1996) to discover a cluster of galaxies at $z \simeq .75$ by looking for an excess in the redshift distribution in the field of a gravitationally lensed quasar.

Miralles *et al.* (1996) used the method to determine the redshift distribution of the Hubble Deep Field.

The "ultra-violet dropout" techniques of Steidel *et al.* (1996b; 1996a) and Madau *et al.* (1996) are similar if simpler. All galaxy spectra have a large Lyman break; shortward of 912Å, the continuum drops dramatically. When this break is redshifted into and past the U filter, the U flux is greatly reduced or non-existent, resulting in very red ultra-violet colours.

In the ultra-violet dropout techniques, an exact redshift of a galaxy is not determined. Rather, the redshift is determined to be in the redshift range where the Lyman break is in or just past the U filter. Since U filters typically have a central wavelength of 3500Å, this works out to a redshift of $z \sim 2.5$. In practical terms, redshifted template galaxy spectra are used to determine a locus on a colour-colour plot where most galaxies lie in a particular redshift range. Those galaxies whose measured colours lie within the locus are deemed to be in that redshift range. Clearly, this method is a lot simpler than that of Pelló *et al.* (1996) as only two colours are considered. It is also a lot less precise since the redshift is not strongly constrained. For both these reasons it is best suited for pre-selecting galaxies at high redshift for spectroscopic study. Steidel *et al.* (1996b) did exactly this using the U_N, G, and $\mathcal{R}$ filters to preselect objects for spectroscopy. Madau *et al.* (1996) applied this technique to the Hubble Deep Field using the F300W, F450W, F606W and F814W filters. The technique was extended to higher redshifts by using F450W dropouts to find galaxies of redshifts $z \sim 4$. By detecting these dropouts, it was possible to place constraints on the star formation rate and metal production at high redshifts.

3.1.3 Linear regression

Perhaps the simplest and certainly the most empirical photometric redshift technique yet is that of Connolly *et al.* (1995a). This method requires a "training set" of a large number of galaxies with multi-colour photometry and spectroscopic redshifts. Redshift, z, is assumed to be a linear or quadratic function of the magnitudes (M_i) of the galaxies, that is, if N is the number of filters:

$$z = a_0 + \sum_{i=1,\ldots,N} a_i M_i \tag{3.1}$$

or

$$z = a_0 + \sum_{i=1,\ldots,N} a_i M_i + \sum_{\substack{i=1,\ldots,N \\ j=i,\ldots,N}} a_{ij} M_i M_j \tag{3.2}$$

The constants, a_i and a_{ij}, are found by linear regression. Connolly *et al.* (1995a) used a $UJFN$ plus redshift data set extending to $z \sim .5$ of 370 galaxies. They showed that this method could determine redshifts with uncertainties of $\sigma_z = 0.057$ with a linear fit and $\sigma_z = 0.047$ with a quadratic fit. There is little or no loss of accuracy if colours ($C_i = M_i - M_{i-1}$) are used instead of magnitudes. Using this technique they were able to measure the luminosity function out to $J \sim 24$ (SubbaRao *et al.*, 1996).

The linear regression technique has two advantages and two disadvantages. The advantages: (1) It is extremely simple. (2) It is completely empirical: one does not have to assume that the galaxies in question have the same spectral energy distribution as local galaxies. The disadvantages: (1) A substantial collection of spectroscopic redshifts must have been measured before the technique can used. (2) Extension to fainter magnitudes or

deeper redshifts is not possible.

3.1.4 Template fitting

The template fitting technique developed by Loh & Spillar (1986b) more closely resembles that of Baum (1962) than that of Koo (1985). The technique is described in detail in Section 3.2, but can be summarized as follows: First, the photometric data for each galaxy in the fields are converted into spectral energy distributions (SED's). Second, a collection of template spectra of all Hubble types and redshifts in the range of interest is compiled. Third, the spectral energy distribution derived from the observed magnitudes of each object is compared to each template spectrum in turn. The best matching spectrum and hence the redshift is determined by minimizing χ^2.

Loh & Spillar (1986b) observed 34 galaxies of known redshift in the galaxy cluster 0023+1654 through 6 non-standard filters to test their method. The standard deviation of the redshift differences ($z_{spec} - z_{phot}$) was 0.12. They went on to use their technique to measure photometric redshifts for 1000 field galaxies in order to determine a value for the density parameter, Ω_0 (Loh & Spillar, 1986a). Ellis *et al.* (1985) and MacLaren, Ellis & Couch (1988) used template fitting with a 7 filter set to confirm the membership of galaxies in clusters. Gwyn (1995) tested this method using $BVRI$ photometry obtained at CFHT of the Colless *et al.* (Colless *et al.*, 1990; Colless *et al.*, 1993) galaxies. Numerous authors (Gwyn & Hartwick, 1996; Lanzetta *et al.*, 1996; Mobasher *et al.*, 1996; Sawicki *et al.*, 1997; Cowie *et al.*, 1996) have used this technique to determine redshifts in the Hubble Deep Field.

3.1.5 Variations

Benítez (1998; 1999) added a twist to the template fitting technique. In the normal technique, only the differences between the template and the observed SED are considered when calculating the likelihood of fit. In the Bayesian photometric redshifts method, one's expectation of the redshift distribution is also taken into account. Care is necessary when choosing the redshift distribution function; it is possible to bias the results. As an extreme example, if one expects the redshift distribution to be a delta function at z=1 and uses that as an expectation function, then no photometric redshifts other than z=1 would be measured. However, with more reasonable and conservative choices, Benítez showed that it is possible to reduce the residuals in the photometric redshifts from $\Delta z/(1+z) = 0.10$ to 0.08. A similar method has been used by Kodama, Bell & Bower (1999) to discriminate between cluster members and background/foreground galaxies in the field of Abell 370. They propose using it for high redshift clusters.

In the standard template fitting technique, the redshift and the type of the galaxy are the free parameters. To these two parameters, Furusawa *et al.* (1999) add 2 extinction parameters. The first is internal absorption in the galaxy; the second is the amount of intergalactic absorption. The prescription for intergalactic absorption by Madau (1995) is actually an expression for the median absorption. From Figure 1 of Madau (1995), one can see that there is quite a distribution of absorptions along different lines of sight. Indeed the mode of the distribution is considerably less than the median. Furusawa *et al.* (1999) claim that the accuracy of photometric redshifts is improved if

these two extinctions are left as free parameters.

3.2 The template fitting technique in general

Although the template fitting technique has been described cursorily on numerous occasions (*q.v.* the references in the previous section), it has not been given complete exegesis in the same way the colour diagram and linear regression techniques have. This section provides that description.

The template fitting technique can be divided into three steps:

1. The photometric data for each galaxy (through various filters) are converted into spectral energy distributions (SED's). The magnitude in each bandpass is converted to a flux (power per unit bandwidth per unit aperture area) at the central or effective wavelength, λ_{cen}, of the bandpass. When the flux is plotted against wavelength for each of the bandpasses, a low resolution spectral energy distribution is created.

2. A set of template spectra for different Hubble types is compiled from various sources. These spectra are then redshifted. The redshifted spectra are reduced to the passband averaged fluxes at the central wavelengths of the passbands in order to compare the template spectra with the SED's of the observed galaxies.

3. The spectral energy distribution derived from the observed magnitudes of each object is compared to each template spectrum in turn. The best matching spectrum, and hence the redshift, is determined by minimizing χ^2.

In the following subsections, each of these steps is examined in turn.

3.2.1 Photometry to spectral energy distributions

It is said that anyone who makes a significant contribution to any field of endeavour becomes an obstruction to its progress in direct proportion to the importance of his or her original contribution. If this is true of anybody, it is true of Pogson (1856) who formalized the magnitude system which has been alternately a boon and a plague to astronomers since it was introduced more than 2000 years ago (Hipparchus, 130 BC; Ptolemy 140). Although the magnitude system is convenient in many instances, it has one major deficiency. It is not directly obvious what the shape of the spectral energy distribution of a source is by looking at its magnitudes and colours. The magnitude in each bandpass must be converted to a flux (power per unit bandwidth per unit aperture area) at the central or effective wavelength, λ_{cen}, of the bandpass. When the flux is plotted against wavelength for each of the bandpasses, a low resolution spectral energy distribution is created.

To convert magnitudes in some filter, m, to fluxes, F, one uses the following equation:

$$F = F_0 10^{-m/2.5}. \tag{3.3}$$

where F is the flux in units of $\mathrm{W\,\AA^{-1}m^{-2}}$ and F_0 is the flux zero-point of that filter system in the same units. This equation is straightforward to use as long as the flux zero-point is known. Magnitude systems are ostensibly calibrated to the type A0 star, Vega, which has $m = 0$ for all filters by definition. In practice, there is usually some small but significant zero-point shift between

the Vega calibration and reality. By using information from Johnson (1966), Koo (1985), Glass (1973), Steidel & Hamilton (1993), Fukugita, Shimasaku & Ichikawa (1995), and Fukugita *et al.* (1996) it is possible to derive the flux zero-points for the usual Johnson-Cousins *UBVRI* system, the photographic *UJFN* system, the Space Telescope F300W, F450W, F606W and F814W system used in the HDF, the *ugriz* system used in the Sloan Digital Sky Survey, the *UnGR* system of Steidel *et al.* , and the infrared *JHK* system. This information is summarized in Table 3.1.

When magnitudes are specified on the *AB* system, the flux zero-points are defined to be $3.631 \times 10^{-23} W\, Hz^{-1} m^{-2}$ for all filters. Since spectra are usually described in $W\,\text{Å}^{-1} m^{-2}$, it is convenient to convert the flux zero-points to these units:

$$F_{0\lambda} = \frac{c}{\lambda_{cen}^2} 10^{10} F_{0\nu} \tag{3.4}$$

Where $F_{0\lambda}$ is the flux zero-point (in units of $W\,\text{Å}^{-1} m^{-2}$), $F_{0\nu}$ is the flux zero-point (in units of $W\, Hz^{-1} m^{-2}$), c is the speed of light (in $m s^{-1}$), λ_{cen} is the central wavelength (in Å) of the filter in question, and 10^{10} is the number of angstroms in a metre. Using the values for the *AB* system, we have:

$$F_{0\lambda AB} = \frac{1.095 \times 10^{-4}}{\lambda_{cen}^2(\text{Å})} \tag{3.5}$$

The *ST* system used by the Hubble Space Telescope is the most convenient of all. The flux zero-points is defined to be $F_{0\lambda ST} = 3.63 \times 10^{-12} W\,\text{Å}^{-1} m^{-2}$ for all filters (Code *et al.*, 1980).

For small values, absolute uncertainties in the magnitudes are roughly equivalent to relative uncertainties in the fluxes:

Table 3.1: Filter properties

Filter	λ_{cen}	F_0 ($\times 10^{-12}$WÅ$^{-1}m^{-2}$) "Vega"	AB	ST
$U_{\rm Johnson}$	3650Å	4.36	8.22	3.63
$B_{\rm Johnson}$	4400Å	6.37	5.66	3.63
$V_{\rm Johnson}$	5500Å	3.71	3.63	3.63
$R_{\rm Cousins}$	6500Å	2.21	2.59	3.63
$I_{\rm Cousins}$	8000Å	1.13	1.71	3.63
$U_{\rm Kron}$	3660Å	4.18	8.17	3.63
$J_{\rm Kron}$	4630Å	5.56	5.11	3.63
$F_{\rm Kron}$	6170Å	2.69	2.88	3.63
$N_{\rm Kron}$	7940Å	1.21	1.74	3.63
F300W	3000Å	3.54	12.09	3.63
F450W	4575Å	5.61	5.23	3.63
F606W	6030Å	2.71	3.01	3.63
F814W	8000Å	1.14	1.70	3.63
u'_{SDSS}	3550Å	3.67	8.74	3.63
g'_{SDSS}	4750Å	5.11	4.81	3.63
r'_{SDSS}	6200Å	2.40	2.83	3.63
i'_{SDSS}	7650Å	1.28	1.88	3.63
z'_{SDSS}	9050Å	0.783	1.34	3.63
$U_{\rm NSteidel}$	3570Å	3.68	8.59	3.63
$G_{\rm Steidel}$	4830Å	5.05	4.69	3.63
$\mathcal{R}_{\rm Steidel}$	6930Å	1.73	2.28	3.63
J	1.2μm	0.318	0.760	3.63
H	1.6μm	0.117	0.428	3.63
K	2.2μm	0.039	0.226	3.63

$$\begin{aligned}
\Delta M &= M_1 - M_2 \\
&= 2.5\log(F_2/F_1), \text{ if } \Delta F = F_2 - F_1 \\
&= 2.5\log(1 + \frac{\Delta F}{F_1}) \\
&\simeq \frac{2.5}{\ln 10}\frac{\Delta F}{F_1} \\
\Delta M &\simeq \frac{\Delta F}{F}
\end{aligned} \tag{3.6}$$

Once the magnitudes are converted into fluxes, the equivalent of a very low resolution spectrum can be made by plotting the fluxed against the central wavelength of the filters.

3.2.2 The template spectra

In this step, the goal is to produce a set of template spectral energy distributions spanning the redshift range of interest. One wishes to have templates at fairly small redshift intervals ($\Delta z \lesssim .05$), smaller than the expected redshift uncertainty. The templates should also cover all Hubble types, from ellipticals to irregulars, again at fine intervals.

There are many sources from which to compile template SED's:

- Pence (1976) lists spectra for four galaxy types(E/S0,Sab,Sbc,Sdm-Im) spanning a wavelength range from either 1900Å (for ellipticals) or 1400Å (for other types) to 8000Å. The data is derived from ground-based and Orbiting Astronomical Observatory (OAO) observations.

- Coleman, Wu & Weedman (1980, frequently referred to as CWW) give data for four types as well: an old stellar population (ellipticals and

bulges), Sbc, Scd and Im. The wavelength range is 1400Å to 10000Å. Their data is derived from Astronomical Netherlands Satellite (ANS), the OAO and the International Ultraviolet Explorer (IUE) as well as ground-based data.

- Bruzual (1985) published a pair of spectra: E/S0 and Irr The wavelength coverage extends from 1400Å to 33000Å. The extensions to the infra-red were done using broad band (*JHKL*) photometry.

- More recently, Kinney *et al.* (1996) published 12 template spectra (ellipticals, bulges, S0, Sa, Sb, Sc and six starburst types). The spectra extend from 1200Å to 10000Å. The data come from IUE and ground based telescopes.

- In a different vein, Bruzual & Charlot (1993) have generated galaxy spectra based on theoretical models. The advantage of these model spectra is that they extend bluewards all the way to 150Å as well as red-wards to 25500Å. This provides full spectral coverage for the U filter for even the highest redshifts. Another advantage is that they include the effects of evolution.

- The models of Worthey (1994) span the spectrum from 91Å to 160μm. They are available for metallicities from [Fe/H]=-2.0 to [Fe/H]=0.5, ages from 1 to 18 Gyr and a wide variety of initial mass functions.[1]

- The PEGASE models of Fioc and Rocca-Volmerange (1997) have much

[1] They are also available from
`http://www.astro.lsa.umich.edu/users/worthey/getmodels/dial_a_model.html`

to recommend them. They match the observed portion of the UV spectra of galaxies much better than those of Bruzual & Charlot and Worthey. They incorporate the effects of nebular emission and dust (and its evolution). At the risk of showing a local prejudice, some might argue that the fact they use the Victoria isochrones (Vanden-Bergh *et al.*, 1983) is an asset. The models span the wavelength range from 220Å to 96980Å. The PEGASE models are available from `http://www.iap.fr/users/fioc/PEGASE.html`.

To summarize, there are empirical SED's with spectral coverage down to 1200Å in the UV and model templates with much greater coverage. Since, if one wishes to produce templates for redshifts greater than $z = 1$ with the U as one of the filters, it is necessary to have coverage shortwards of 1200Å, and since it is desirable to use empirical data, some workers (*e.g.* Sawicki *et al.*, 1996; Ferguson & McGaugh, 1994) have extended the SED's of CWW either by fitting a power law to the bluest section of the spectra and extrapolating or by adding sections of theoretical model spectra. In a similar vein, it is sometimes desirable to apply empirical modifications to theoretical templates. Gwyn (1995) found that small changes (as a function of redshift and type) to the colours of the Bruzual & Charlot (1993) templates significantly improved the photometric redshifts. Cowie *et al.* (1996) made similar modifications to the infra-red portions of his templates.

Since the SED's come at discrete Hubble types (E/S0, Sab, Scd, Imm) whereas they really form a continuum, it is desirable to interpolate between the available spectra to fill in the gaps. If the gaps between templates are

large, subtle uncertainties and biases may be introduced. Interpolating between types is not an unreasonable thing to do as the galaxy SED's can be represented (to first order) by a one-parameter family of types from ellipticals to irregular. All types of galaxies can be thought of as containing a passively evolving (bulge) component and a starforming (disk) component. The bulge contains old, red stars with little or no star formation. The disk contains younger, bluer stars which are constantly renewed. Ellipticals are pure passively evolving bulge and irregulars are pure starforming disk; spiral galaxies contain both components in varying ratios. Thus, to construct spectra for all types of galaxies, one need only mix the spectra of an elliptical and an irregular galaxy. Connolly *et al.* (1995b), using principal component analysis, found that the spectra of all types of galaxies could be produced to within 1% using only two eigenspectra: an "average spectrum" and a "deviation spectrum". It is justifiable, then, to define a morphological type parameter, t. For irregulars, $t = 0$; for ellipticals, $t = 1$. For intermediate types, t can be equated to the bulge to total light ratio in a spectral energy distribution.

It is relatively straightforward to redshift a spectrum. If the spectrum is stored in two columns, wavelength and flux at that wavelength, one has but to multiply each wavelength by $(1 + z)$, where z is the desired redshift.

At high redshifts, the effects of absorption by the intergalactic medium (IGM) become important. The higher the redshift of the galaxy, the more the wavelengths of the Lyman system in the rest frame of the galaxy are shifted into the observer frame passbands. As each Lyman transition wavelength moves into the observed bands, a sharp increase in the opacity of the intergalactic neutral hydrogen occurs. When the Lyman break moves in to the

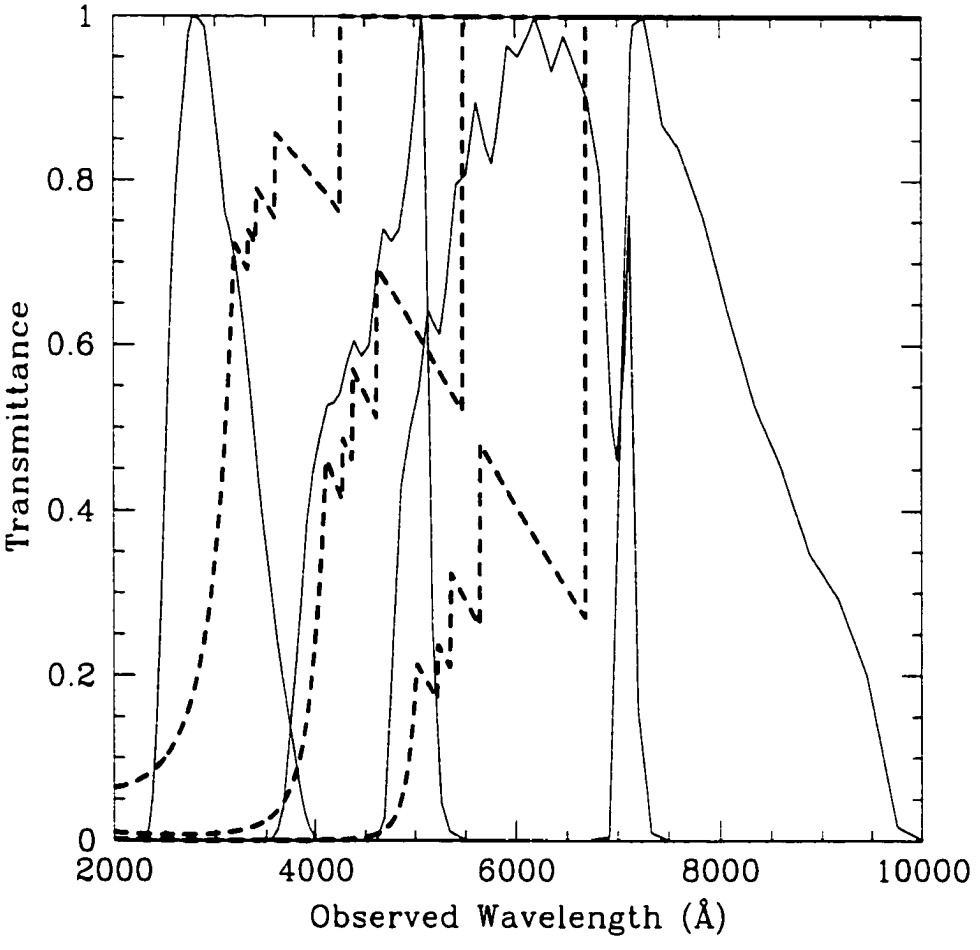

Figure 3.1: Intergalactic absorption. The dashed lines show the transmittance of the intergalactic medium for sources at high redshift as a function of observed wavelength. From right to left, the three curves correspond to sources at z=2.5, z=3.5 and z=4.5. The solid lines show the bandpasses of the filters used for the Hubble Deep Fields.

band, the transmittance drops to almost zero. This is illustrated in Figure 3.1. It shows the observational passbands of the Hubble Deep Fields (solid lines) and the transmittance ($e^{-\tau_{eff}}$) of the IGM as calculated by Madau (1995). The amount of intergalactic extinction is a straightforward function of the observed wavelength (λ_{obs}) and the redshift of the emitter (z_{em}). Madau gives a fairly simple expression for the effective optical depth, τ_{eff}, along a typical line of sight. This correction can be applied to the template spectra.

In order to compare the template spectra with the SED's of the observed galaxies, the redshifted spectra are reduced to the passband averaged fluxes at the central wavelengths of the passbands:

$$F_{pb} = \frac{\int_{\lambda_1}^{\lambda_2} T(\lambda)P(\lambda)d\lambda}{\int_{\lambda_1}^{\lambda_2} P(\lambda)d\lambda}. \tag{3.7}$$

where $T(\lambda)$ is the template spectral energy distribution, $P(\lambda)$ is the response function of the passband and λ_1 and λ_2 represent the wavelengths where the passband response function falls to zero. [2]

3.2.3 Comparing the templates to the SED's

Given a spectral energy distribution of a galaxy of unknown redshift and a set of templates, the next step is to compare the SED to each of the templates in turn in order to find the template which most closely matches the SED.

[2] In principle, this convolution should be performed in units of *photons* $\text{Å}^{-1}m^{-2}$ rather than $\text{W}\text{Å}^{-1}m^{-2}$. In practise, the difference is completely neglible.

The degree to which each template matches the observed SED is quantified by χ^2 in the following manner:

$$\chi^2(t, z) = \sum_{i=1}^{N_f} \frac{(F_i - \alpha T_i(t, z))^2}{\sigma_{F_i}^2}. \tag{3.8}$$

where t is the spectral type, z is the redshift, N_f is the number of filters in the set, F_i and σ_{F_i} are respectively the flux and the uncertainty in the flux in each bandpass of the observed galaxy, T_i is the flux in each bandpass of the template being considered, and α is a normalization factor. A normalization factor is necessary to compare the galaxies and the templates properly: α must remain a free parameter in order to determine the very least χ^2. For fixed values of t and z, χ^2 can be minimized with respect to α. By setting the derivative of equation 3.8 with respect to α equal to zero, a closed formula for α can be found:

$$\alpha = \frac{\sum_{i=1}^{N_f} \frac{F_i T_i}{\sigma_{F_i}^2}}{\sum_{i=1}^{N_f} \frac{T_i^2}{\sigma_{F_i}^2}}. \tag{3.9}$$

Each template is compared in turn to the target galaxy SED and the smallest value of χ^2 is found. The best matching template gives z_{phot}, the sought-after photometric redshift of the galaxy, and t, the spectral type, as a bonus.

It is also possible to do the comparison in magnitudes. Equation 3.8 becomes:

$$\chi^2(t, z) = \sum_{i=1}^{N_f} \frac{(M_{Fi} - M_{Ti}(t, z) - \alpha)^2}{\sigma_{M_{F_i}}^2}. \tag{3.10}$$

Where M_{Fi} and $\sigma_{M_{F_i}}$ are respectively the magnitudes and the uncertainty in the magnitudes in each bandpass of the observed galaxy, M_{Ti} is the flux

in each bandpass of the template expressed as a magnitude, and α is a normalization factor given now by

$$\alpha = \frac{\sum_{i=1}^{N_f} \frac{M_{Fi} - M_{Ti}(t,z)}{\sigma^2_{M_{Fi}}}}{\sum_{i=1}^{N_f} \frac{1}{\sigma^2_{M_{Fi}}}}. \tag{3.11}$$

3.3 The template fitting technique as used in this thesis

In the initial stages of this thesis only the template spectra of Coleman, Wu & Weedman (1980, CWW) were used. There exist (even locally) bluer galaxies than CWW's bluest spectrum, Imm. This leads to some noticeable errors when the resulting photometric redshifts were compared to the corresponding spectroscopic redshifts. Therefore, the starburst spectra of type SB3 and SB2 from Kinney *et al.* (1996) were added. All these spectra were extended into the infrared with JHKL photometry from the compilation of Yoshii & Takahara (1988). They were extended into the ultraviolet by linear extrapolation as far as 912Å in the same manner as Ferguson & McGaugh(1994). Shortwards of the Lyman break at 912Å the exact shape of the spectra does not matter because the effects of intergalactic absorption dominate, causing the galaxy to be largely invisible at these wavelengths. Shortwards of the break, the spectra have values equal to their value at 912Å: that is, they become flat in F_λ. This is a somewhat arbitrary decision, but tests have shown that other options (e.g. linear extrapolation out to the far UV) have no effect on the photometric redshifts. Spectra intermediate to the six original spectra

were produced by interpolation for a total of 51 template spectra.

Figure 3.2 shows the template spectra that were used. The heavy lines show the original SED's. They are (from the bottom) E/S0, Sbc, Scd, Imm, SB3 and SB2. The first four are from Coleman, Wu & Weedman (1980); the last two are from Kinney *et al.* (1996). The light lines are interpolations between the original SED's. The template spectra were redshifted. The redshifts are spaced at intervals of 0.022 in $\log z$. There are 100 intervals running from $z = 0.079$ to $z = 12.589$ (although in practice, no galaxy in the sample has a redshift higher than $z = 6$). Spacing the redshifts of the templates logarithmically puts more templates at low redshifts (where most of the galaxies lie) and fewer at high redshift (where there are relatively fewer galaxies). Having 100 linearly spaced redshift intervals running from $z = 0$ to $z = 6$ would a mean a spacing of $\Delta z = 0.06$. This is overkill at high redshift, where the typical redshift error (at $z = 3$, say) is $\sigma_z = 0.33$. The spectra were corrected for intergalactic extinction and then multiplied by the passbands as described in 3.2.2.

As noted in Section 2.4, there are a substantial number of galaxies in the sample with no U photometry. There are two possible reasons for this. The first possibility is that the galaxy lies at high redshift ($z > 2$) and the Lyman break has been redshifted into the U. The other possibility is that the galaxy lies at low redshift but is intrinsically faint in the U band. Red galaxies, such as ellipticals, often fall into this later category. Obviously, just because a galaxy is undetected in the U, one cannot assign it a high redshift. On the other hand, one cannot ignore the non-detection and determine a photometric redshift based solely on the other three bands.

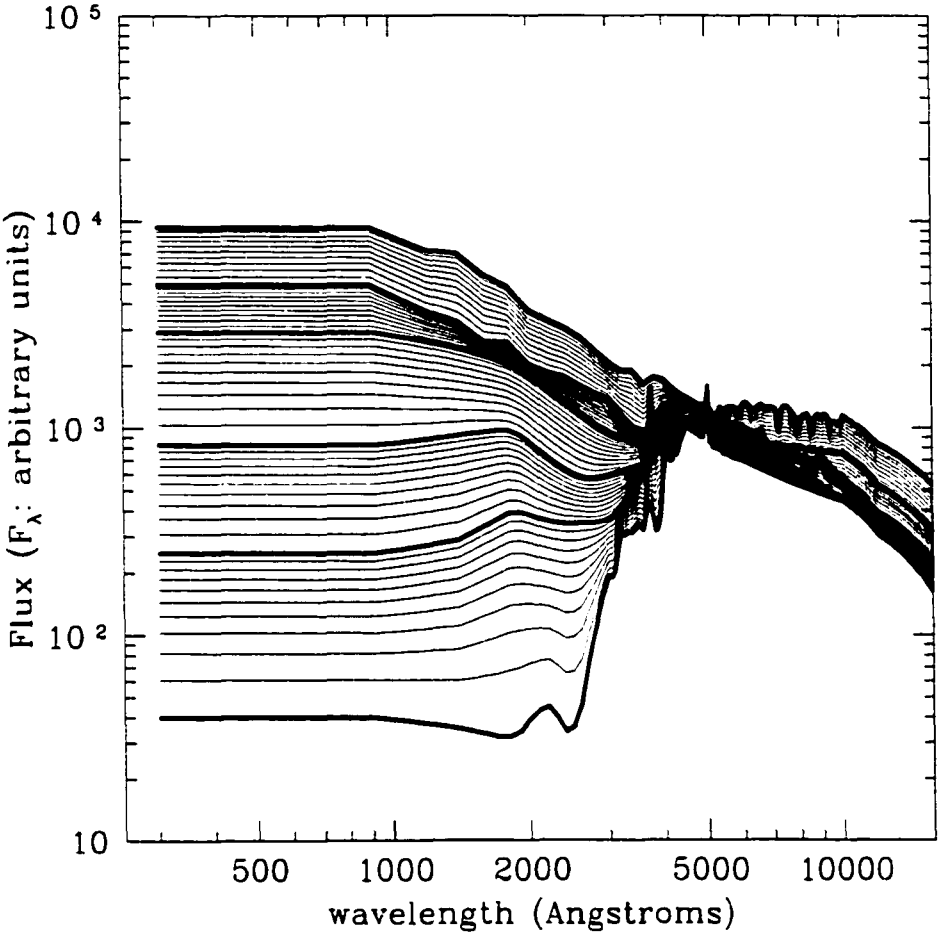

Figure 3.2: Spectral templates. The heavy lines show the original SED's. They are (from the bottom at 1000Å) E/S0, Sbc, Scd, Imm, SB3 and SB2. The light lines are interpolations between the original SED's.

The situation is handled by replacing the term corresponding to the U band in the sum in equation 3.8, where χ^2 is calculated. If the flux predicted by the template is less than the limiting flux in the U band, the term is replaced with zero. If this is not case, on the other hand, the term is replaced with

$$\frac{(F_{U_{lim}} - \alpha T_U(t,z))^2}{\sigma^2_{F_{U_{lim}}}} \tag{3.12}$$

where $F_{U_{lim}}$ is the limiting flux in the U band and $\sigma^2_{F_{U_{lim}}}$ is the uncertainty in the flux that a galaxy would have at $F_{U_{lim}}$. The rest of the symbols have the same meaning as in Equation 3.8. Similarly, if one does the comparison in magnitudes, the U term in 3.10 becomes either zero, if the predicted magnitude is less than the limiting magnitude, or

$$\frac{(M_{U_{lim}} - M_{T_U}(t,z) - \alpha)^2}{\sigma^2_{M_{U_{lim}}}}, \tag{3.13}$$

otherwise. Here $M_{U_{lim}}$ is the limiting magnitude in the U band and $\sigma^2_{M_{U_{lim}}}$ is the uncertainty in the magnitude that a galaxy would have at $M_{U_{lim}}$. The rest of the symbols have the same meaning as in Equation 3.10.

Figure 3.3 illustrates the problem and the solution. It shows two objects in the HDFN for which there was no U detection. The heavy solid lines and points show the photometry for each object. The dashed lines show the limiting magnitude for each band. The U band is shown as an upper limit with a downwards pointing arrow. The left panel shows a low redshift galaxy. If one assumes that since there is no U detection, it must be a high redshift U-dropout, one obtains a photometric redshift of $z \sim 3.5$ as shown by the dotted SED. Using the prescription described above, on the other hand, the

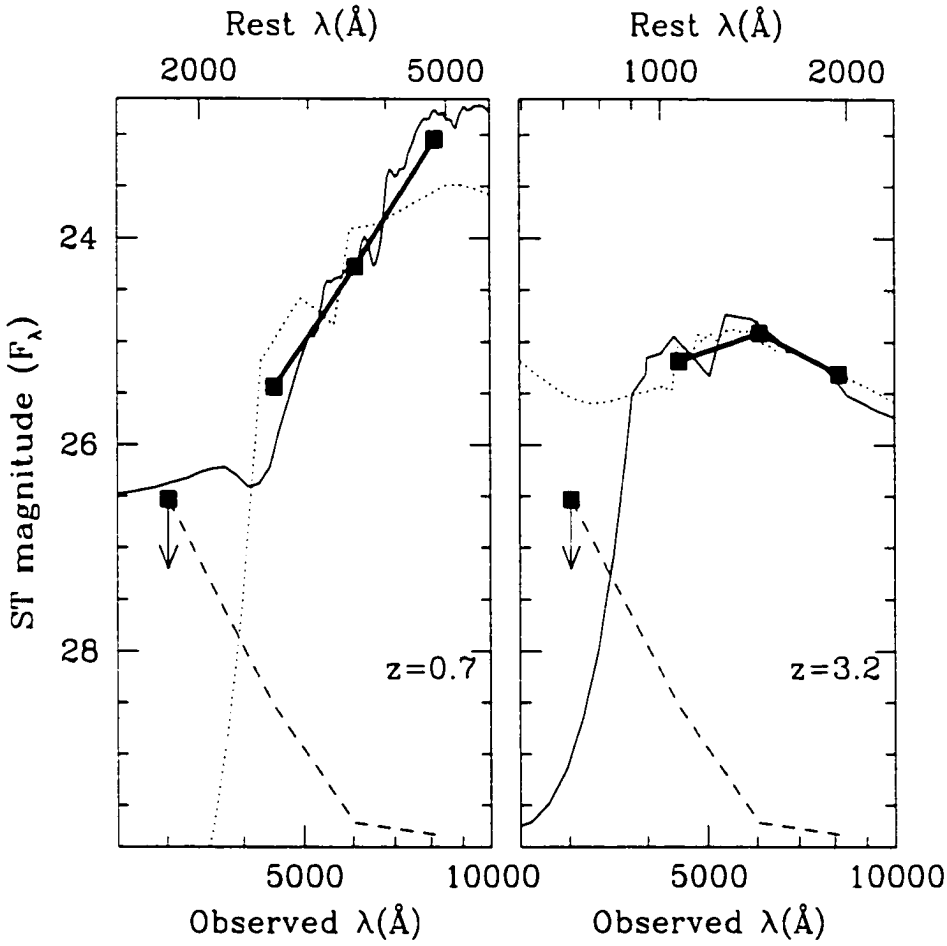

Figure 3.3: U^{*} dropouts. The heavy solid lines and points show the photometry for each object: upper limits are indicated with an arrow. The light solid lines show the best-fitting template and the dotted line shows an alternate (incorrect) template. The dashed lines show the limiting magnitude for each band. The bottom axis gives the observed frame wavelengths: the upper axis does the same in the rest frame of the galaxies, calculated using its photometric redshift.

best fitting template is found to be an elliptical at $z = 0.7$; this template is shown by the light solid line. This template corresponds better to what one can determine from other evidence: its appearance (it looks like an elliptical galaxy) and its spectroscopic redshift (z_{spec}=0.372). The other panel shows the opposite case. The best fitting template, as determined by treating the U band as an upper limit, gives a redshift of $z_{phot} = 3.2$, quite close to the spectroscopic value of z_{spec}=2.991. Ignoring the U entirely and determining a photometric redshift based solely on the BRI photometry, gives a redshift $z_{phot} = 0.2$; this template is shown by a dotted line.

There is an equivalent procedure when working with fluxes. Even when there is no significant detection, one retains the minute (and occasionally negative) fluxes when doing the photometry. The errors in the flux of a non-detection are determined entirely by the sky background. Template matching then occurs as before, using Equation 3.8. Although the value of α may be altered slightly by the presence of negative fluxes in 3.9, these data will have large uncertainties and will not receive much weight.

For this thesis, the χ^2 minimization was done in magnitudes rather than fluxes, using Equations 3.10 and 3.13. If the galaxy photometry is in ST magnitudes, it is much easier to do the comparison between the photometry and the templates. As a test, photometric redshifts were also determined using fluxes. The redshifts thus derived were found to be virtually identical to those derived using magnitudes.

3.4 Results

The technique described above was applied to the photometric sample of Chapter 2. Figure 3.4 shows a comparison of the photometric redshifts with the 120 spectroscopic redshifts currently available. The spectroscopic redshifts for the Hubble Deep Field North come from Cohen *et al.* (1996), Lowenthal *et al.* (1997), Steidel *et al.* (1996a), Zepf *et al.* (1997), Hogg *et al.* (1998), Fernández-Soto *et al.* (1999), Spinrad *et al.* (1998) and Weymann *et al.* (1998). Those from the Hubble Deep Field South come from: Glazebrook *et al.* (in preparation) and Sawicki & Mallen-Ornelas (in preparation)

.

The agreement is generally quite good. Since the redshift uncertainties scale with z, Figure 3.4 has been plotted with logarithmic axes. The error in photometric redshift scales with redshift; that is to say, $\sigma_z \propto z$. The typical relative error in the photometric redshifts is $\sigma_z/z = 11\%$ over the whole range of redshifts.

The error in galaxy type was also measured. For those galaxies with spectroscopic redshifts, the template fitting procedure was performed again. In this fitting, only the type was allowed to vary; the redshift of the templates was set to the spectroscopic redshift of the galaxy in question. The best-fitting template gives the correct type for that galaxy. Comparing this type to the type determined by the original template fitting (when both redshift and type are allowed to vary) gives the error in galaxy type. The error in galaxy type was found to be $\sigma_{\rm type} = 7$ templates, or $\sigma)t = 0.14$ on a scale of $t = 0$ to $t = 1$, roughly equivalent to a shift of one Hubble type (from Sa to

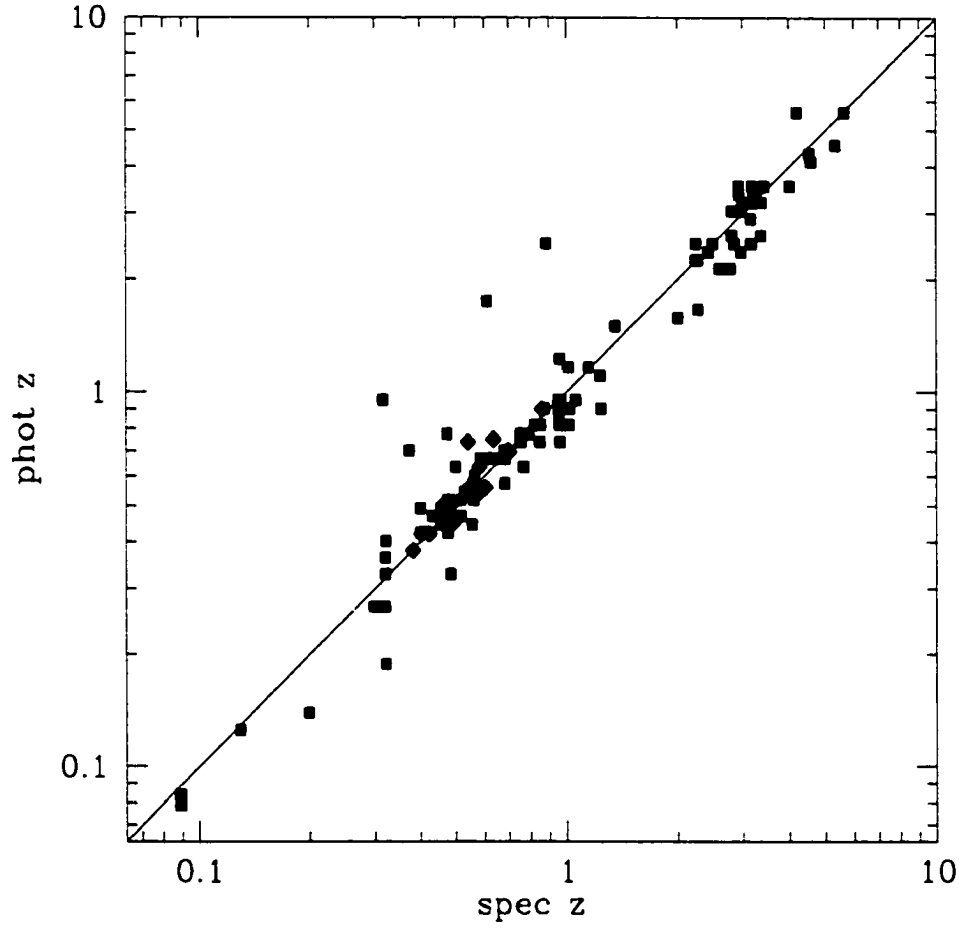

Figure 3.4: A comparison of photometric and spectroscopic redshifts. The filled squares represent galaxies in the HDF North: those in the HDF South are shown by open diamonds.

Sb, say). This is comparable in scale to the redshift error.

Figure 3.5 shows the photometric redshift distribution for galaxies brighter than $I_{ST} = 28$ in the HDFN and HDFS. The bulk of the galaxies lie at lower redshifts ($z < 2$) with a poorly populated tail extending out $z = 6$ There is second peak just above $z = 2$.

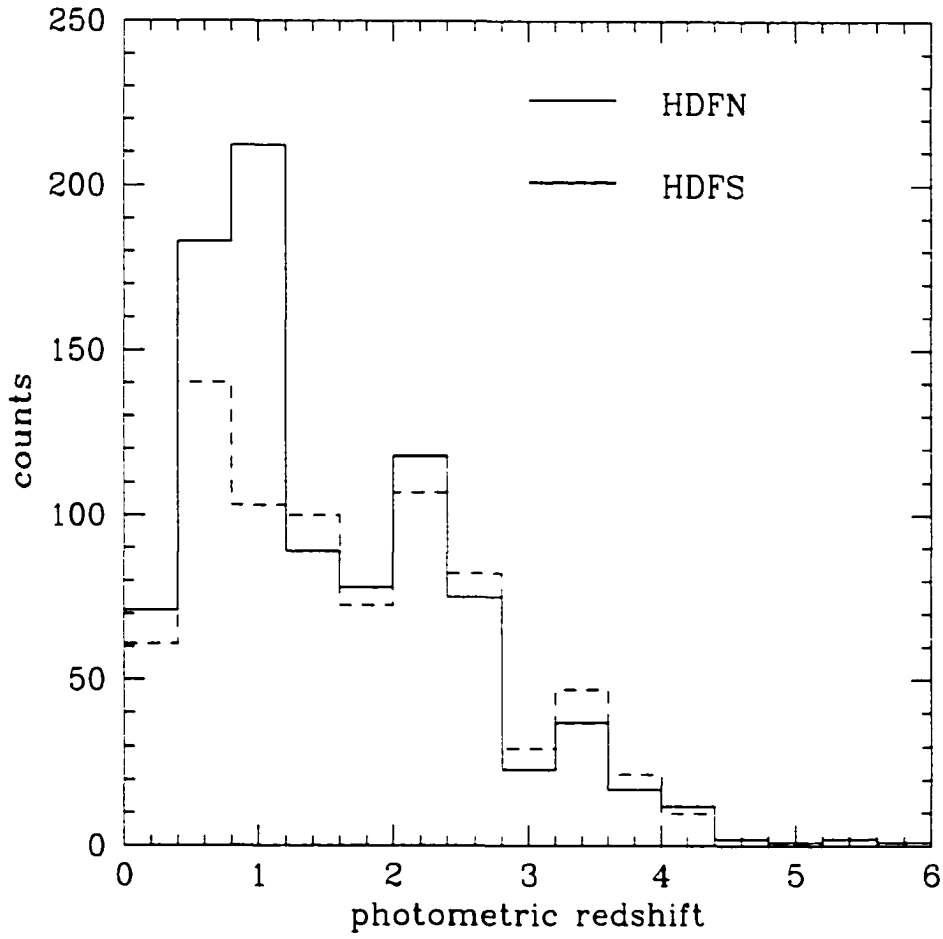

Figure 3.5: Photometric redshift distributions for the HDF North (solid line) and the HDF South (dashed line).

Chapter 4

Clustering

This chapter examines the evolution of the clustering properties of galaxies using correlation functions. The angular correlation function, $\omega(\theta)$, measures the excess probability of finding a galaxy at angular separation on the sky, θ, away from another galaxy. If galaxies are uniformly distributed on the sky, $\omega(\theta) = 0$. If they are clustered, $\omega(\theta)$ will have some non-zero value. Correlation functions are measured by comparing the observed number of pairs of galaxies at a given angular separation to the number of pairs at the same angular separation of a randomly generated uniform set of galaxies.

The angular correlation function is a projection of the spatial correlation function, $\xi(r)$, where r is distance, onto the plane of the sky. Even if galaxies are strongly clustered in space, when the third dimension of depth is lost to projection, a part of the clustering signal is lost too. Galaxies which are quite distant from each other in space, and hence uncorrelated, may end up quite close together in projection. The deeper the sample is, the greater the loss in clustering signal will be and the closer $\omega(\theta)$ will be to zero.

Correlation functions have been measured before in Hubble Deep Field

North by Villumsen, Freudlong & da Costa (1997). Not being able to split their sample by redshift, they split it by apparent magnitude. (This is, in essence, splitting by one filter photometric redshifts.) Consequently, the amplitudes of their correlation functions are not large. For the most part, they are consistent with zero within the errors at all angular separations.

It is actually quite difficult to measure correlation functions in the Hubble Deep Fields. The fields are quite small in surface area; this means that the number of galaxies in each sample will be small. The fields are also very deep. Even if the field is sliced in redshift, each slice still has a much smaller spatial extent in the lateral directions than in depth. For example, a slice from $0.4< z <0.8$ in one of the HDF's is about 1 Mpc by 1 Mpc across by about 500 Mpc deep. As mentioned earlier, this will tend to dilute the clustering signal.

4.1 Motivation

The Hubble Deep Field North resulted in dozens of papers on galaxy evolution. All these papers treat the HDFN as a typical field; the conclusions that are drawn are assumed to hold for all fields. With the advent of the HDF South (Williams *et al.* 1999) it is possible to test this hypothesis.

The two fields do show some differences. The number counts presented in Figure 2.4 show that the HDFN holds 15% more galaxies. This excess is more visible when the differential counts are plotted as shown in Figure 4.1. Only a fraction of the galaxies in the HDFN and virtually none of the galaxies in the HDFS have spectroscopic redshifts. Thus, the question

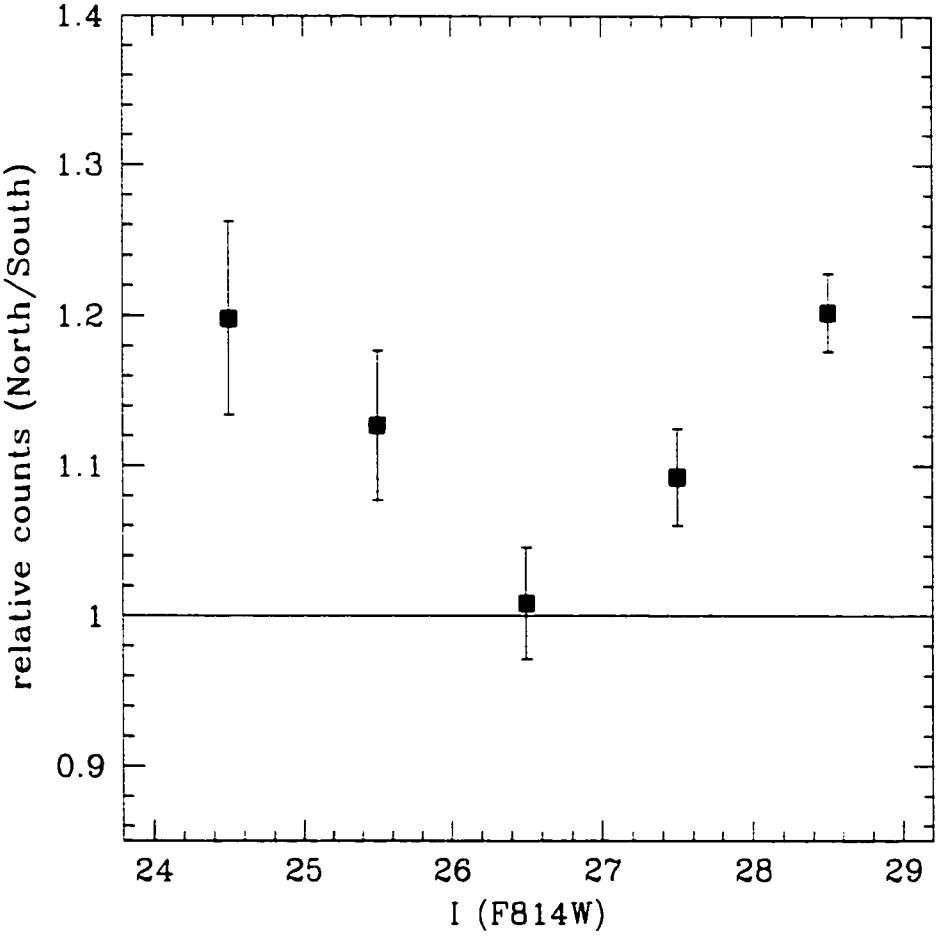

Figure 4.1: Relative number counts for the Hubble Deep Fields. The ratio (North divided by South) of the F814W number counts in each magnitude bin is shown. There are roughly 15% more galaxies in the HDFN compared to the HDFS

"where do these excess galaxies in the HDFN lie?" must be addressed with photometric redshifts.

The redshift distributions for the HDF North and South are shown in Figure 3.5. The two redshift distributions are not the same. The Kolmogorov-Smirnov test gives the probability of the two distributions being the same as 1.2×10^{-6}. The redshift distributions are most different in the redshift range $0.4 < z < 1.2$.

It is tempting to ascribe the differences in the Hubble Deep Fields to a structure present in the North but not in the South. Indeed, there is a pronounced spike in the spectroscopic redshift distribution of the HDFN at $z = 0.475$ (Cohen *et al.* 1996). Figure 4.2 shows the I band images of the Hubble Deep Fields. Only light from galaxies with photometric redshifts in the range $0.4 < z < 0.8$ is shown: the other galaxies have been masked out.[1] The images have been convolved with a Gaussian profile ($\sigma = 6$ arcseconds). The left image shows a large concentration of light in the HDFN that is not present in the South. To measure this effect quantitatively, one must use correlation functions.

Another reason to measure correlation functions is to see if there is any change in the clustering of galaxies with redshift. In the hierarchal clustering picture, the Universe starts out uniform and unclustered: structure grows as the Universe ages. Therefore, one might expect to see the correlation amplitudes decreasing with increasing redshift.

[1] this can be done for any redshift slice: see
`http://astrowww.phys.uvic.ca/grads/gwyn/pz/dice.html`

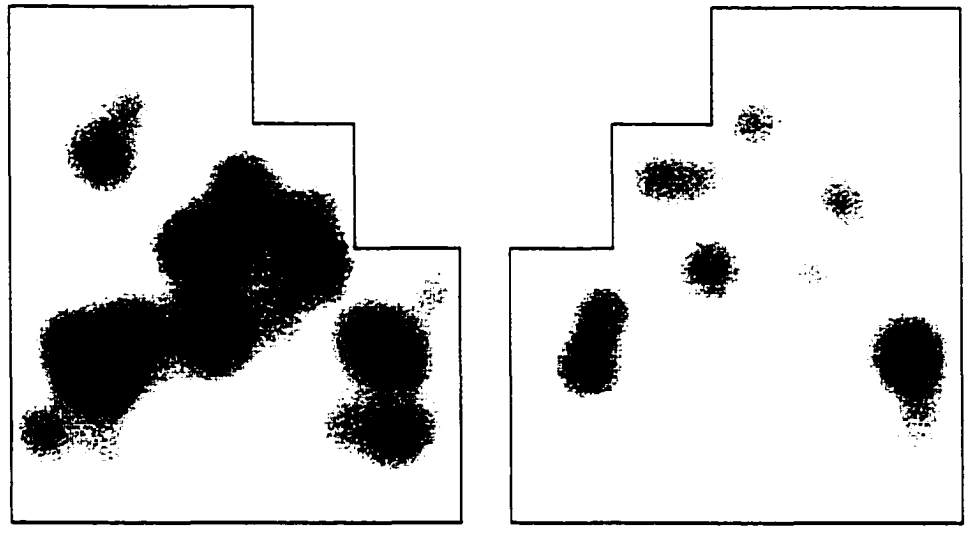

Figure 4.2: I band light in the HDFN (left) and HDFS (right) coming from galaxies with photometric redshifts in the range $0.4 < z < 0.8$. The image has been convolved with a 6 arcsecond radius Gaussian. Note the concentration of light near the centre of the North image which is not present in the South

4.2 Method

The most common methods of measuring correlation functions are described in detail elsewhere (Infante & Pritchet, 1995; Landy & Szalay, 1993) and are only briefly summarized here. The basic idea is to generate a set of random points in an area identical to the area of sky that was surveyed. The correlation function is measured by comparing the number of pairs of data galaxies with a given angular separation to the corresponding number for the random points. Let N_d be the number of data galaxies, N_r be the number of random points, and $N_{dd}(\theta)$, $N_{rr}(\theta)$, and $N_{dr}(\theta)$ be respectively the numbers of data-data, random-random, and data-random pairs in a bin. The appropriately normalized versions of these values are DD, RR and DR respectively:

$$\begin{aligned} DD &= \frac{2.N_{dd}(\theta)}{N_d(N_d-1)} \\ RR &= \frac{2.N_{rr}(\theta)}{N_r(N_r-1)} \\ DR &= \frac{N_{dr}(\theta)}{N_r.N_d} \end{aligned} \tag{4.1}$$

Then one has for estimators of ω:

$$\omega(\theta) = \frac{DD}{DR} - 1 \tag{4.2}$$

which is the most basic estimator, or alternatively

$$\omega(\theta) = \frac{DD - 2DR + RR}{RR} \tag{4.3}$$

which is the "minimum variance" estimator of Land and Szalay (1993). Plugging the definitions of Equation 4.1 into 4.2 one has:

$$1 + \omega(\theta) = \frac{2.N_{dd}(\theta).N_r}{N_{dr}(\theta)(N_d - 1)} \tag{4.4}$$

To this, it may be required make two small further corrections to equation 4.4:

$$1 + \omega(\theta) = \frac{2.N_{dd}(\theta).N_r}{B.N_{dr}(\theta)(N_d - 1)} - \omega_{rd} \tag{4.5}$$

The first term corrects the effects caused by the fact that the data galaxies are not necessarily evenly distributed within boundaries of the sample, whereas the random galaxies always are. This correction, $\omega_{rd}(\theta)$, is usually small. It is given by

$$1 + \omega_{rd}(\theta) = \frac{DR}{RR} = \frac{N_{dr}(\theta)(N_r - 1)}{2.N_{rr}(\theta).N_d}. \tag{4.6}$$

The second correction is the "integral constraint", B. It is in essence a correction to the mean surface density of a galaxies which is over-estimated due to clustering. The integral constraint is given by:

$$B = \frac{\sum_i N_r r(\theta_i)}{\sum_i (1 + \omega(\theta_i).N_r r(\theta_i))} \tag{4.7}$$

where the $\sum_i$ are sums over all the bins in angle. Since B depends on $\omega(\theta)$ in Equation 4.7 and $\omega(\theta)$ depends on B in Equation 4.5, it may be necessary to iterate. Similar corrections must be made to Equation 4.3.

4.3 Results

The two-point angular correlation functions were computed for various redshift slices using Equation 4.4. The integral constraint, B, was found to be

very close to unity (within 1 part in 10^3) for all redshift slices. Therefore, no integral constraint corrections were made to correlation functions. Similarly, the random-data cross correlation effects (as measured by $\omega_{rd}(\theta)$) were found to be negligible and were ignored. The angular correlation functions were converted into projected spatial correlation functions $\omega(r_p)$, where r_p is the projected distance. This is the distance between two galaxies projected onto the plane of the sky at the angular diameter distance, d_A, corresponding to the central redshift of each redshift slice. A H_0=65 km s^{-1}Mpc^{-1}, Ω_0=1 cosmology was used to calculate the angular diameter distance.

The correlation function was measured for a wide variety of redshift slices. Figure 4.3 shows four representative slices. The correlation functions for the HDFN are shown as squares; those for the HDFS as triangles. Note that it is impracticable to calculate the angular correlation function for slices much narrower than the ones shown without running into problems with small number statistics. Further, because of the uncertainties on the redshifts, it would be difficult to compute a reliable spatial (as opposed to projected spatial) correlation function.

The first thing one should note from Figure 4.3 is that, for most redshift slices, the correlation functions show no difference within the errors. This is also true for other redshift slices not shown on the figure. The only exception was in the $0.4 < z < 0.8$ redshift slice, where galaxies in the HDFN were significantly more clustered than in the HDFS. This suggests the presence of a structure in this redshift bin in the HDFN. As noted earlier, there is a sharp peak centred at $z = 0.475$ in the *spectroscopic* redshift distribution of the HDFN. The spatial scale of the structure (the HDF is $\sim$ 1 Mpc across

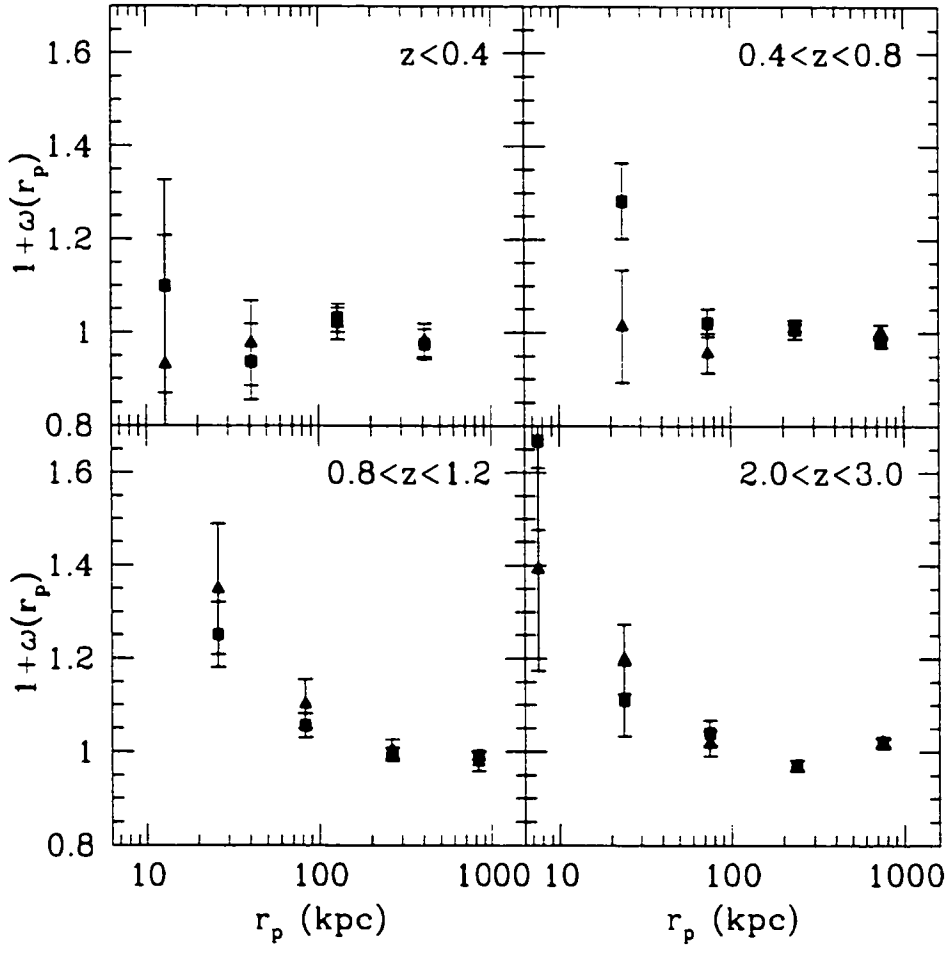

Figure 4.3: The project spatial correlation function for various redshift slices. The correlation functions for the HDFN are shown by squares: the HDFS is shown by triangles. The error bars show Poisson uncertainties.

at that redshift) and the number of galaxies involved ($\sim$ 50 more galaxies in the North than in the South) suggest a very poor galaxy cluster or a very rich group.

More generally, the differences in the redshift distributions could be due to cosmic variance in the large scale galaxy distribution. This hypothesis was tested empirically in the following manner: The William Herschel Deep Field (McCracken *et al.*, 2000, WHDF) extends to $B = 28$ and has good coverage in the $UBRIHK$ bands. It covers roughly 40 square arcminutes. The WHDF was divided into 9 separate areas, each the same size as the Hubble Deep Fields. The field-to-field variance was found to be 10% (rms), smaller than, but not inconsistent with, the difference between the HDFN and HDFS.

N-body simulations computed by Stadel (private communication) indicate the variance in the mass distribution along lines of sight comparable the HDF are about 20% out to $z = 1$. Assuming that galaxies trace the mass, at least in a statistical sense, this variance in mass should translate into a similar variance in the redshift distributions of the galaxies in the Hubble Deep Fields. Again, this is consistent with the difference between the two redshift distributions below $z = 1$ as seen in Figure 3.5.

The second thing one should note from Figure 4.3 is that the galaxies become more clustered with increasing redshift. The hierarchal clustering scenario, on the other hand, predicts the opposite trend. However, the clustering observed is only on the scales of $\sim$10 kpc, roughly the size of individual galaxies. This suggests that we are looking at the initial assembly of galaxies as galaxy fragments merge. Alternatively, it is possible that fragments of

larger galaxies are being counted as separate galaxies, rather than as parts of a whole. However, it should be emphasized that the galaxy catalog described in Chapter 2 was constructed with great care with respect to deblending, both automatically (with SExtractor) and manually (by scrutinizing each galaxy individually).

The problem is typified by the objects shown in Figure 4.4. It is clear that the four objects are separate, although there are hints of faint filaments connecting them. The morphology is the same in the three bands in which the objects are detected. All four objects have photometric redshifts of $z = 3.3$: the spectroscopic redshift of the brightest object is $z = 3.210$ (Steidel *et al.*, 1996b; Zepf *et al.*, 1997). The question is: are these bright starforming regions in one larger object or are they instead smaller galaxies in the process of merging? At some level, it is a question of degree. If the fragments have not already merged, they will soon. The same holds for the clustered objects bringing up the correlation function at small separations at high redshift: it is slightly irrelevant whether or not the objects are fragments of a merged whole or fragments about to merge.

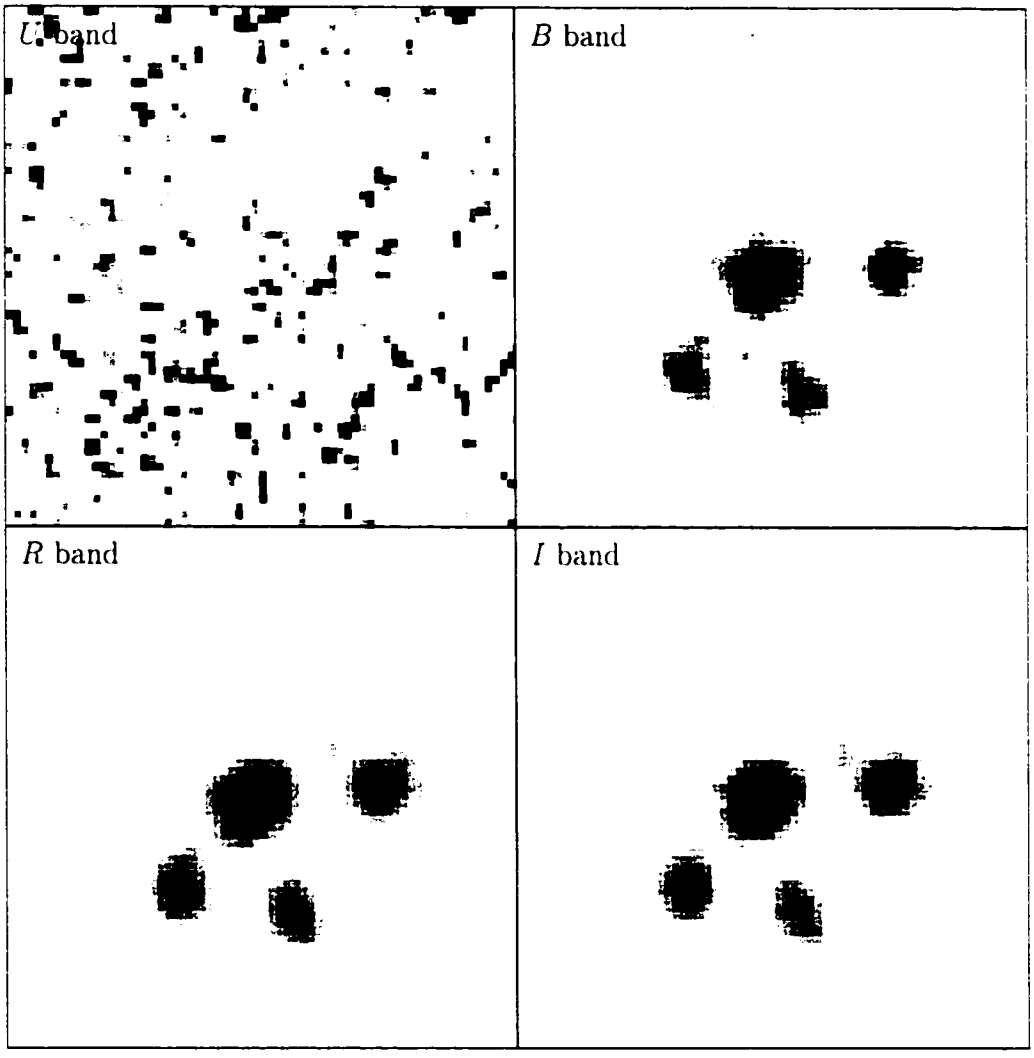

Figure 4.4: Four galaxy fragments. The four objects have photometric redshifts of $z = 3.3$; the spectroscopic redshift of the brightest object is $z = 3.210$. Note the complete lack of detection in the U band due to intergalactic absorption. The boxes are 2.6 arcseconds on a side, corresponding to 20 kpc at the redshift of the objects.

Chapter 5

Star Formation Rates

This chapter examines the evolution of the star formation rate density (SFRD) as measured by the UV luminosity density. The first step is to measure the UV luminosity function of galaxies for a series of redshift slices. The luminosity function describes the relative abundance of galaxies per unit volume, as a function of magnitude. The luminosity function can be measured using the either the $1/V_a$ method or the stepwise maximum likelihood (SWML) method. This entails measuring absolute magnitudes for galaxies, which in turn entails getting k-corrections. Further consideration must be given to account for surface brightness effects and the effects of the redshift uncertainties inherent in the photometric redshift method. With the luminosity functions in hand, one can generate a luminosity density function which measures the amount of energy density of light from galaxies per unit volume as a function of magnitude. Integrating over magnitude for the luminosity function in each redshift slice, one obtains the luminosity density. Since star formation rate density is directly proportional to the UV luminosity density (with some corrections for dust extinction), one can then measure how SFRD

evolves as a function of redshift.

5.1 The $1/V_a$ method

The $1/V_a$ method is well known (Schmidt, 1968) and has been described in detail elsewhere so the following description will be brief. V_a is defined as the volume accessible to a galaxy given its absolute magnitude and the limits defining the sample in which it is found. Formally,

$$V_a = \int_{z_{min}}^{z_{max}} \frac{dV}{dz} dz. \tag{5.1}$$

where dV/dz is the co-moving differential volume element:

$$\frac{dV}{dz} = \frac{4\pi c d_L^2}{H_0(1+z)^3(1+2q_0z)^{1/2}}. \tag{5.2}$$

The luminosity distance d_L is given by equation 5.3:

$$d_L = \frac{c}{H_0 q_0^2}\{q_0 z + (q_0 - 1)[(1+2q_0z)^{1/2} - 1]\}. \tag{5.3}$$

where H_0 is the Hubble constant (assumed to be $65\,\mathrm{km\,s^{-1}Mpc^{-1}}$) and q_0 is the deacceleration parameter (assumed to be $\frac{1}{2}$). Note that Equations 5.2 and 5.3 are considerably more complicated if $\lambda \neq 0$. The limits, z_{min} and z_{max} are defined as the smallest and largest redshift that a given galaxy could be at and still make it into the sample. These limits can be fixed, as in a volume-limited sample. For a magnitude-limited sample, they must be determined for every galaxy. The lower bound, z_{min}, is usually the lower redshift limit of the sample or the redshift at which the galaxy becomes too bright to make it into the sample (if the sample is defined with a bright magnitude limit). The

upper bound, z_{max}, is either the upper redshift bound of the sample or the redshift at which the galaxy becomes fainter than the faint magnitude limit. Given the absolute magnitude, M, of each galaxy and m_{lim}, the limiting apparent magnitude of the sample, z_{max} can be determined by solving the following equation:

$$m_{lim} = M + \mu(z_{max}) + k(z_{max}). \tag{5.4}$$

where $\mu(z_{max})$ is the distance modulus corresponding to z_{max} and $k(z_{max})$ is the k-correction term.

Finally, to determine the luminosity function, Φ, one uses the equation:

$$\Phi(M) = \frac{4\pi}{A} \sum_{M-\frac{\Delta M}{2}}^{M+\frac{\Delta M}{2}} \frac{1}{V_a}. \tag{5.5}$$

where A is the area surveyed (in steradians) and ΔM is the bin size used.

5.2 The SWML method

The Step-Wise Maximum Likelihood (SWML) method was developed by Efstathiou, Ellis & Peterson (1988, frequently referred to as EEP). Again, this method is described in detail elsewhere, and the following description will be brief. The probability, p_i, that a galaxy, i, with absolute magnitude M_i at redshift z_i will be in a magnitude-limited sample is the value of the luminosity function $\Phi(M_i)$ normalized by the integral over the part of the luminosity function bright enough to be seen at z_i. That is to say,

$$p_i \propto \frac{\Phi(M_i)}{\int_{M_{min}(z_i)}^{\infty} \Phi(M) dM} \tag{5.6}$$

where $M_{min}(z_i)$ is the faintest absolute magnitude that a galaxy could have at z_i and still make it into the sample. The likelihood, $\mathcal{L}$, that all of the N galaxies in the sample were bright enough to be included is the product of the probabilities that *each* galaxy was bright enough to be included: $\mathcal{L} = \prod_i^N p_i$. Or, logarithmically:

$$\ln \mathcal{L} = \sum_i^N \ln \left(\frac{\Phi(M_i)}{\int_{M_{min}(z_i)}^{\infty} \Phi(M) dM} \right) \tag{5.7}$$

$$= \sum_i^N \ln \Phi(M_i) - \sum_i^N \ln \int_{M_{min}(z_i)}^{\infty} \Phi(M) dM \tag{5.8}$$

One can then parameterize the luminosity function and maximize $\ln \mathcal{L}$ with respect to those parameters. In the SWML method, the luminosity function is parameterized as a series of N_p steps at magnitudes M_k of width ΔM. At each step, M_k, the luminosity function has the value Φ_k. It is convenient to define $W(x)$, a boxcar function with the same width as one of the luminosity function bins, and $H(x) = \frac{1}{\Delta M} \int W(x) dx$, its integral (which is a ramp function). Formally:

$$W(x) = \begin{cases} 1. & -\Delta M/2 < x < \Delta M/2 \\ 0. & \text{otherwise} \end{cases} \tag{5.9}$$

$$H(x) = \begin{cases} 0. & -\Delta M/2 > x \\ x/\Delta M + 1/2. & -\Delta M/2 < x < \Delta M/2 \\ 1. & x > \Delta M/2 \end{cases} \tag{5.10}$$

Then Equation 5.8 becomes

$$\ln \mathcal{L} = \sum_i^N W(M_i - M_k) \ln \Phi_k - \sum_i^N \ln \left[\sum_j^{N_p} \Phi_j \Delta M \; H\left(M_j - M_{min}(z_i)\right) \right] \tag{5.11}$$

Maximizing 5.11 with respect to the Φ_k's, one obtains:

$$\Phi_k \Delta M = \frac{\sum_i^N W^*(M_i - M_k)}{\sum_i^N \left[H\left(M_j - M_{min}(z_i)\right) \Big/ \sum_j^{N_p} \Phi_j \Delta M H\left(M_j - M_{min}(z_i)\right) \right]} \tag{5.12}$$

Unfortunately, Equation 5.12 defines the Φ_k's in terms of themselves. In practice, however, one can assume an arbitrary shape for the luminosity function, *e.g.* a flat line ($\Phi_1 \ldots \Phi_{N_p} = 1$), and iterate.

The luminosity function produced by solving Equation 5.12 must be normalized. The Φ_k's must be multiplied by

$$\frac{1}{V^*} \sum_i^N \left[\sum_k^{N_p} \Phi_k \Delta M H\left(M_k - M_{min}(z_i)\right) \right]^{-1} \tag{5.13}$$

where V^* is the effective volume of the sample. In general, the effective volume is the V_a^* corresponding to the largest redshift in the sample. If there are redshift limits z_1 and z_2 on the sample, then the effective volume is given by

$$V^* = \int_{z_1}^{z_2} \frac{dV^*}{dz} dz \tag{5.14}$$

where dV^*/dz is the co-moving differential volume element as before.

5.3 The k-corrections

In the previous two sections, the question of k-corrections was glossed over: this section describes them in excessive detail. When we observe a redshifted galaxy through some filter, we are not looking at the same part of its spectrum that we would be if the galaxy was in the same restframe as we are.

Furthermore, we are looking at smaller section of the spectrum. The k-correction accounts for these two effects. There are few things in astronomy that cause as much confusion as k-corrections. Some authors define the k-correction as the shift in the centre of the bandpass and deal with change in width separately. Here, they are treated together. Further, the equations are different if the SED's of the objects in question are measured in units of power per unit *frequency* instead of power per unit *wavelength*. Here, F_λ is used exclusively. Given the apparent magnitude of a galaxy, m, and a redshift, z, the absolute magnitude, M of a galaxy is given by

$$M = m - \mu(z) - k(z) \tag{5.15}$$

The flux measured through a passband whose response function is given by $P(\lambda)$ of a galaxy whose SED is given by $T(\lambda)$ at redshift z is:

$$F(z) = \frac{\int \frac{T\left(\lambda/(1+z)\right)}{(1+z)} P(\lambda) d\lambda}{\int P(\lambda) d\lambda} \tag{5.16}$$

The k-correction is defined as the ratio (expressed in magnitudes) of the flux of the galaxy through the filter when the object is at redshift z and the flux when the galaxy is in the rest frame of the observer, $z = 0$.

$$\begin{aligned} k(z) &= -2.5 \log_{10} \frac{F(z)}{F(0)} \\ &= 2.5 \log_{10} F(0) - 2.5 \log_{10} F(z) \\ &= 2.5 \log_{10} \frac{\int T(\lambda) P(\lambda) d\lambda}{\int P(\lambda) d\lambda} - 2.5 \log_{10} \frac{\int \frac{T\left(\lambda/(1+z)\right)}{(1+z)} P(\lambda) d\lambda}{\int P(\lambda) d\lambda} \end{aligned}$$

$$= 2.5\log_{10}\frac{\int T(\lambda)P(\lambda)d\lambda}{\int T\big(\lambda/(1+z)\big)P(\lambda)d\lambda} + 2.5\log_{10}(1+z) \qquad (5.17)$$

In equation 5.17, the first term represents the shift in the bandpass and the second term, the change in the width of the bandpass.

The responses of the HDF filters, $P(\lambda)$, are shown in Figure 2.1. When the photometric redshifts were determined, a galaxy type was determined as well. The SED of this best-fitting template is used for $T(\lambda)$ in Equation 5.17. The template is normalized to the photometry in the same way it was during the photometric redshift procedure as described by Equations 3.10 and 3.11. Once this is done, the flux for any bandpass at any wavelength can be determined using this normalized bandpass.

Alternatively, one could convert the *UBRI* photometry into fluxes, plot those fluxes against the central wavelength of each filter (shifted to the rest frame) and linearly interpolate or extrapolate to get the flux at the desired rest wavelength. The fitting described above is close to being such an interpolation or an extrapolation. In particular, when the absolute magnitude at 2500Å is sought, this is essentially an interpolation for galaxies between z=0.2 and z=2.25. However, the intermediate step of template fitting makes the procedure superior to simple linear interpolation. The SED's of galaxies — particularly early-type galaxies — are not particularly well described by linear segments. Figure 5.1 illustrates this. It shows the difference between k-corrections determined by strict interpolation/extrapolation and the true k-corrections. Linear interpolation can lead to magnitude errors of up 0.4 magnitudes. Extrapolation at higher redshifts can lead to even larger errors.

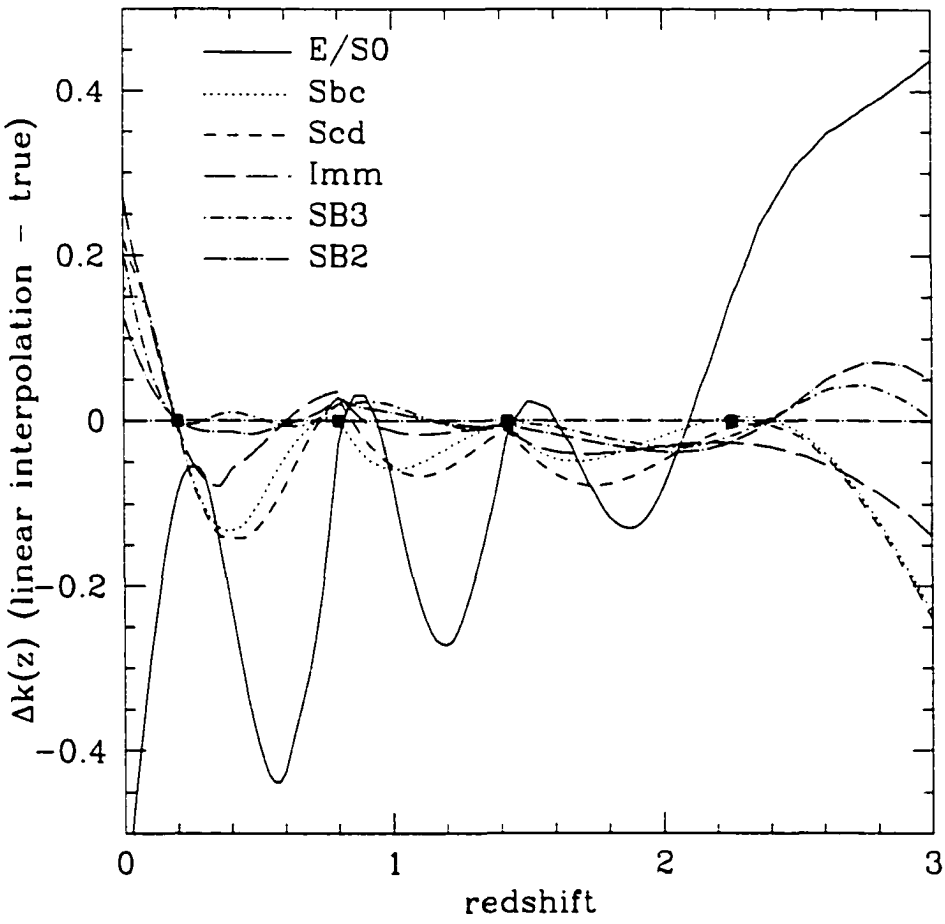

Figure 5.1: The difference between an estimation of the flux at a rest wavelength of 2500Å by linear interpolation of $UBRI$ photometry and the true flux determined directly from the template. The differences are small for late types of galaxies but substantial for earlier types.

5.4 Comparing methods and fields

As noted in Chapter 4, The HDFN and HDFS have different redshift distributions and (at least in one redshift slice) slightly different angular correlation functions. It has been noted by several authors that the $1/V_a$ can potentially give biased results for spatially inhomogeneous samples. This section examines the possibility by comparing the results of the $1/V_a$ method to those of the SWML method (which is generally agreed to be unbiased) in the HDFN and HDFS. If the spatial inhomogeneity is large enough to cause biases in the $1/V_a$ method, they should show up when the two methods are compared in the two fields.

Figure 5.2 shows the luminosity functions at 2500Å for both the fields measured by both methods. Several redshift slices are shown. The luminosity functions for the HDFN are similar to those for the HDFS, for the most part, with the exception of the $0.5 < z < 1.0$ slice. This is the slice that contains an over-density of objects in the HDFN. Even in this slice, it would appear that a small vertical shift would suffice to match up the two luminosity functions. That is to say, there are density differences between the fields, rather than luminosity differences. While it is possible to distinguish the luminosity functions for the different fields, it is considerably more difficult to separate the lines corresponding to the luminosity functions measured by the $1/V_a$ method and those for the SWML method.

Figure 5.3 also shows the luminosity functions as measured by the two methods. This time, the results for the HDFN and the HDFS have been averaged. The differences between the two methods are now even less significant.

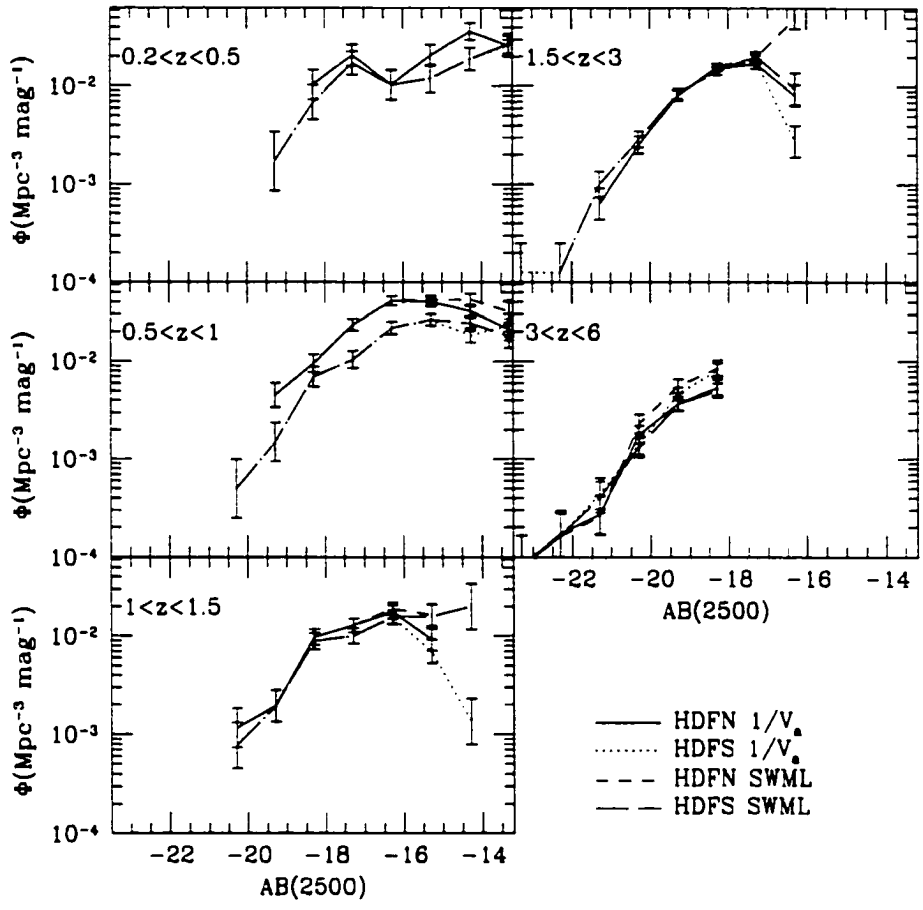

Figure 5.2: Comparing the luminosity functions of the HDFN and HDFS measured by the $1/V_a$ and the SWML methods. The error bars reflect Poisson noise only. The redshift slices are noted in the upper right-hand corner of each panel.

The error bars in Figure 5.3 reflect the Poisson errors ($1/\sqrt{N}$, where N is the number of points in a bin). They also reflect the real, cosmic variance from field to field, as measured by the absolute difference between the values for North and South, divided by $\sqrt{2}$. These two errors are added in quadrature to give the final uncertainty.

5.5 Surface brightness

As noted in Chapter 2, the galaxy sample is defined in terms of a limiting surface brightness as well as a limiting magnitude. The surface brightness limit for the Hubble Deep Fields is 25.8 magnitudes per square arcseconds, as shown in Figure 2.6. Galaxies fainter than this limit are detected less than 90% of the time. Until now in this analysis, the effects of surface brightness on the luminosity functions have been ignored. In a Euclidean geometry, distance has no effect on surface brightness; in the real Universe, the surface brightness of distant objects falls off as $(1+z)^4$. Clearly, there is a possibility that surface brightness effects may alter the luminosity function. This section explores this possibility.

It would be difficult to include the effects surface brightness considerations into the SWML method. One would have to include a surface brightness distribution function into the maximum likelihood calculations. This distribution function would have to be parameterized in some way and incorporated into Equation 5.11. While probably not impossible, it would be extremely messy. Since the SWML and the $1/V_a$ methods give very similar results when only the limiting magnitude needs to be considered, it may

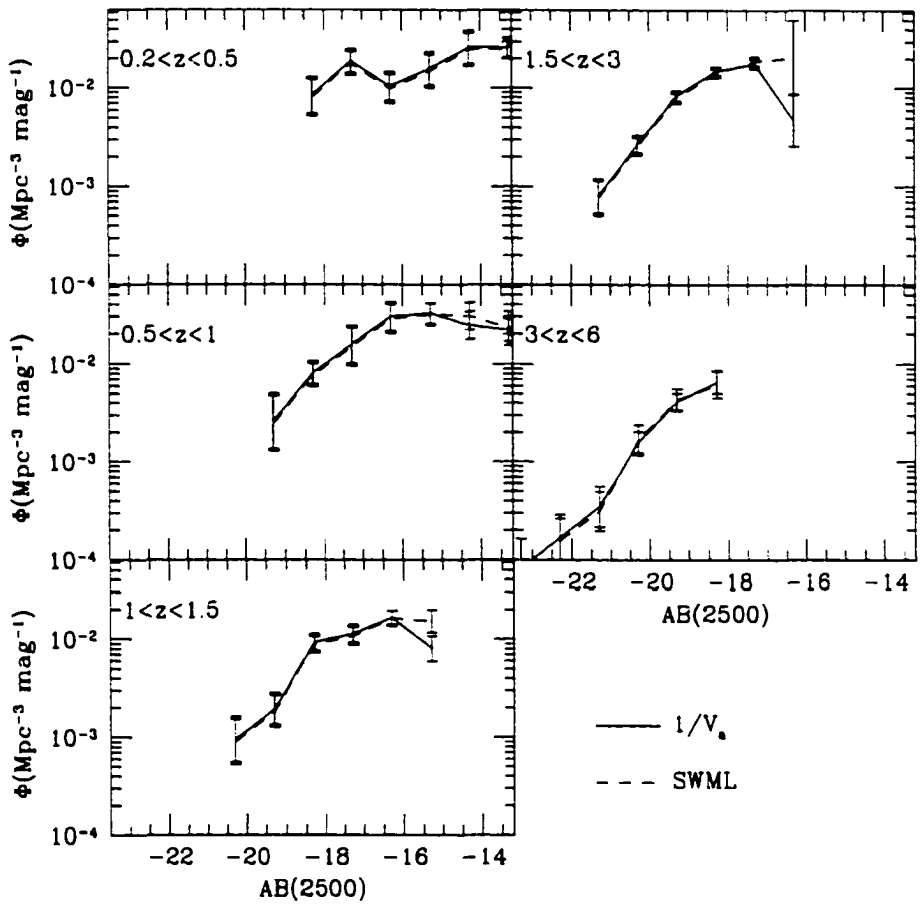

Figure 5.3: Comparing the $1/V_a$ vs. SWML methods of measuring luminosity functions averaging the HDFN and the HDFS. The two methods give very similar results. The error bars reflect Poisson noise and cosmic variance

be assumed the two methods will give similar results when limiting surface brightness is also considered.

To introduce the effects of surface brightness into the $1/V_a$ method, the definition of z_{max} in Equation 5.1 was changed. For a given galaxy, z_{max} is now the lowest of:

- the upper limit of the redshift bin in question ($z_{\rm bin}$).
- the redshift at which the galaxy's magnitude becomes fainter than I=28 ($z_{\rm mag}$).
- the redshift at which the galaxy's peak surface brightness drops below μ_I=25.8 magnitudes per square arcsecond ($z_{\rm surf}$).

The first two limits are easy to find: $z_{\rm bin}$ is defined by the bin in question and $z_{\rm mag}$ is given by Equation 5.4. To calculate $z_{\rm surf}$, one must solve the following equation:

$$\mu_{\rm limit} = \mu_{peak} - 2.5\log_{10}(1+z)^4 + 2.5\log_{10}(1+z_{\rm surf})^4 - k(z) + k(z_{\rm surf}) \quad (5.18)$$

where μ_{peak} and z are the peak surface brightness and the redshift of the galaxy in question respectively. The presence of k-corrections in Equation 5.18 means that it must be solved by iteration.

Figure 5.4 shows the effects of surface brightness on z_{max}. Panel (a) shows z_{max}(mag)=$z_{\rm mag}$ plotted against photometric redshift. Panel (b) is similar but here the vertical axis is z_{max}(mag, surf), the minimum of $z_{\rm mag}$ and $z_{\rm surf}$. The points in panel (b) are typically lower than that of panel (a): the surface brightness cutoff can remove a galaxy from the sample at a lower

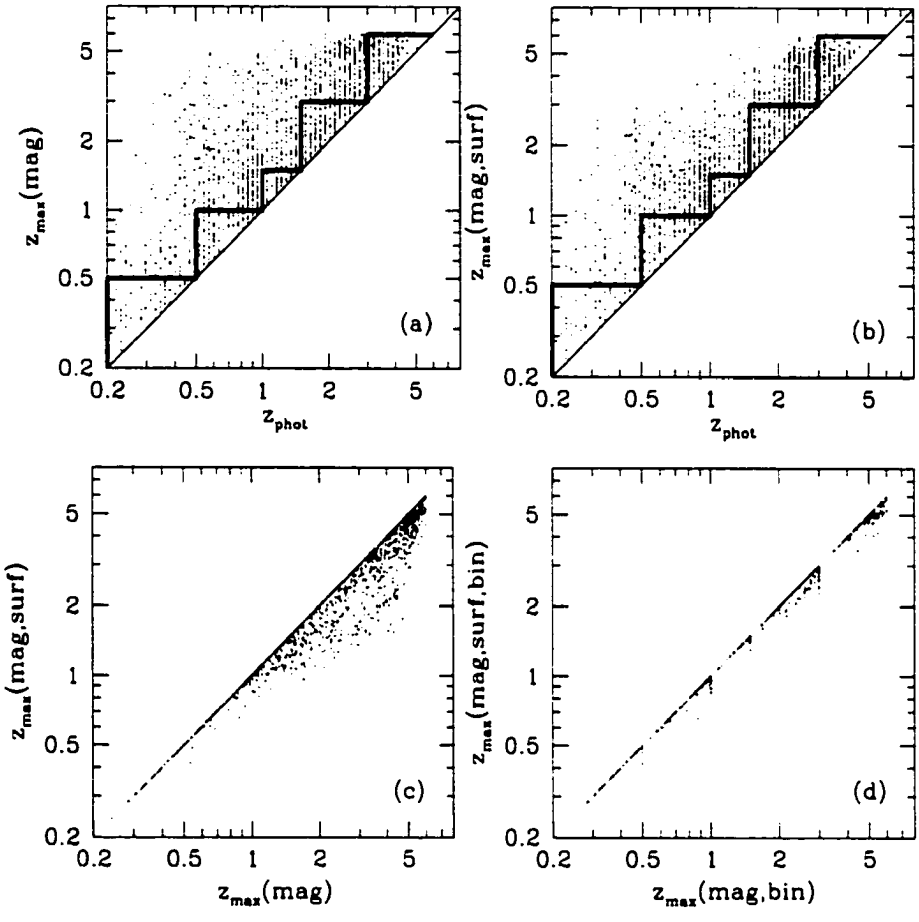

Figure 5.4: The effects of surface brightness on z_{max}. On the axis labels, z_{phot} denotes photometric redshift and z_{max} denotes the maximum redshift the same galaxy could have and still remain in the sample, as limited by the parameters in brackets: magnitude (mag), surface brightness (surf) or redshift bin limits (bin). The redshift bins are shown as a series of steps in panels (a) and (b). Panel (d) shows that, if the limits of the redshift bins are taken into account, adding a surface brightness constraint affects z_{max} only slightly.

redshift than the magnitude cutoff would. This is shown more clearly in panel (c), which plots z_{max}(mag, surf) against $z_{\rm max}$(mag): $z_{\rm max}$(mag) can be up to 3 times greater than z_{max}(mag, surf). These large changes in maximum redshift would have comparable effects on the accessible volume, V_a, for each galaxy and consequently a non-trivial effect on the luminosity function. However, the whole redshift sample has been sliced into redshift bins. The upper limits of these bins, shown as a series of steps in panels (a) and (b) confine the z_{max}'s and consequently the V_a's. When the upper limits are taken into account, panel (c) becomes panel (d) which plots the minimum of z_{mag}, z_{surf}, and z_{bin} against the minimum z_{mag} and z_{bin}. In panel (d), the effects of surface brightness dimming are much less dramatic.

This is borne out by Figure 5.5. The solid line shows the luminosity function calculated assuming only a magnitude limit. The dashed line shows the effects of taking into account the surface brightness limit. The two are extremely similar. Indeed, they can only be clearly distinguished at the faint end of the luminosity functions of the higher redshift bins.

Surface brightness dimming might have more subtle effects. As discussed in Section 2.3, the photometry in the HDF's are total magnitudes measured either by the Kron method or the corrected isophotal method. In principle, these total magnitudes are not subject to surface brightness dimming effects. Un-corrected isophotal magnitudes, on the other hand, are subject to these effects. At higher redshifts, only the central portions of the galaxy are bright enough to make it past the isophotal threshold. This means that the total area over which the light is summed is diminished: the light from the edges of the galaxy is missed. This effect is of course always present when doing

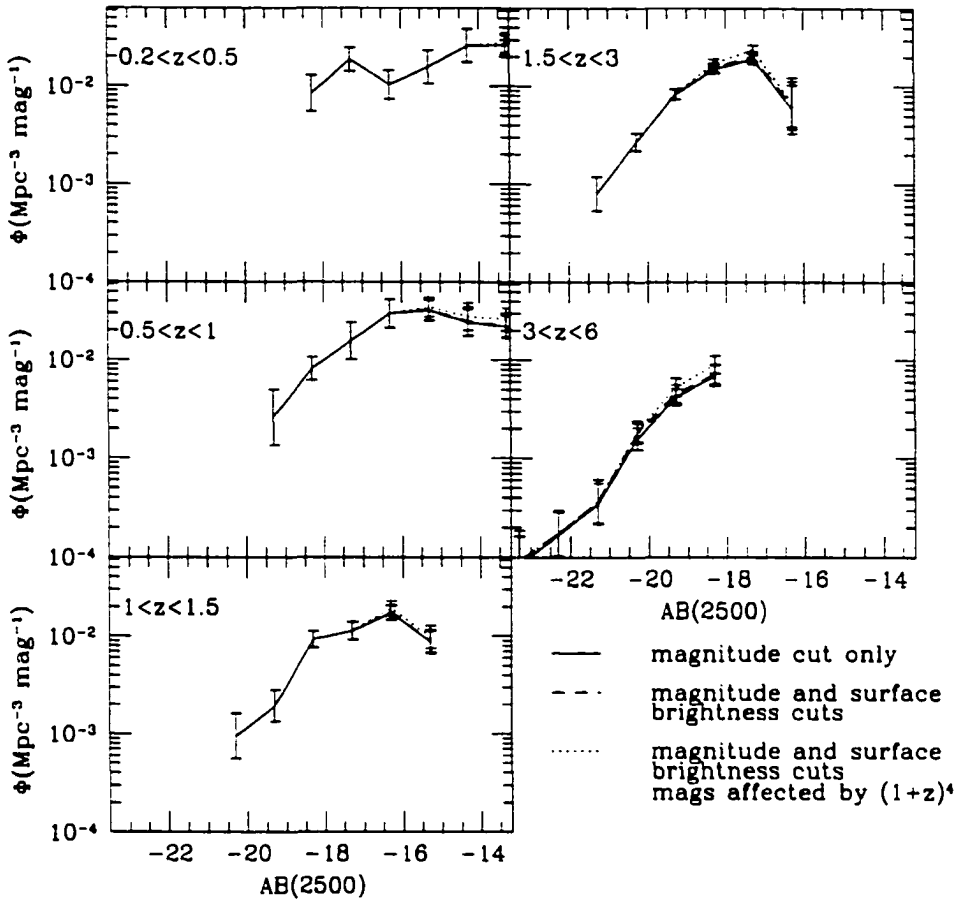

Figure 5.5: The effects of surface brightness on the luminosity functions. The solid line shows the luminosity function calculated assuming only a magnitude limit. The dashed line shows the effects of taking into account the surface brightness limit. The dotted shows the effect of assuming that the magnitudes themselves are affected by surface brightness dimming.

isophotal photometry. It causes fewer difficulties when all the galaxies in the sample are at small redshifts and $(1+z)^4$ surface brightness dimming factor is small. When the galaxies are at higher redshifts or, as in this analysis, the galaxies are being artificially moved to higher redshift to see when they might drop out of the sample, the missed light is more of a problem. With the dimming, galaxies will drop out of the sample at a lower redshift; if the z_{max}'s are smaller, each galaxy will be weighted more heavily in the $1/V_a$. The isophotal method represents a worst-case scenario, an upper limit to the effects surface brightness dimming has on photometry. Neither the Kron method nor the corrected isophotal method (nor, for that matter, the fixed aperture method) will be affected by surface brightness dimming to nearly the same degree, if indeed at all.

The effects of surface brightness dimming on isophotal magnitudes and hence on luminosity functions were measured in the following way. The redshift at which the galaxy would drop out of the sample, z_{iso} was determined by solving Equation 5.4 by iteration as before, but using isophotal magnitudes instead of total magnitudes. Small sub-rasters ("postage stamps") of the original HDF images were made, centred on each galaxy in the sample. For each iteration, the photometry measured for the galaxy in question was measured anew using the relevant sub-raster. To simulate the effects of surface brightness dimming at z_i, the redshift of the iteration, the limiting isophote was raised by a factor of $(1+z_i)^4/(1+z)^4$, where z is the original redshift of the galaxy. The flux from the pixels within this isophote were summed to determine a new magnitude. This magnitude was corrected for distance and k-corrections as before. The limiting redshift determined

using isophotal magnitudes is always less than that determined using total magnitudes. Therefore each galaxy will have greater weight in the $1/V_a$ and therefore the luminosity function will be shifted upwards. The dotted lines in Figure 5.5 show the luminosity functions calculated by this method. As expected, the luminosity functions are slightly elevated, particularly at the faint ends. However, the shifts are not large. As discussed above, this represents a worst case scenario; total magnitudes should not be affected in this manner and certainly not to this degree. Thus, although one does need to be cautious about surface brightness, ultimately it has very little effect on the luminosity functions.

It has been argued (Pascarelle *et al.*, 1998) that in order to compare the UV luminosity densities at both high and low redshift properly, one must apply the same intrinisc surface brightness cut to the sample at both high and low redshifts. However Driver & Cross (2000) have shown that there is a universal luminosity-surface brightness relation. Figure 5.6 shows that high luminosity galaxies also have high surface brightnesses. This implies that an absolute magnitude cut is also effectively a surface brightness cut.

5.6 Eddington corrections

In the previous two sections, it is shown that it is not important which method ($1/V_a$ *vs.* SWML) one uses to calculate luminosity function and that surface brightness effects can be safely ignored. This section discusses factors that *do* affect the shape of the luminosity functions: the errors in the photometric redshifts, the photometry and the galaxy types. These errors

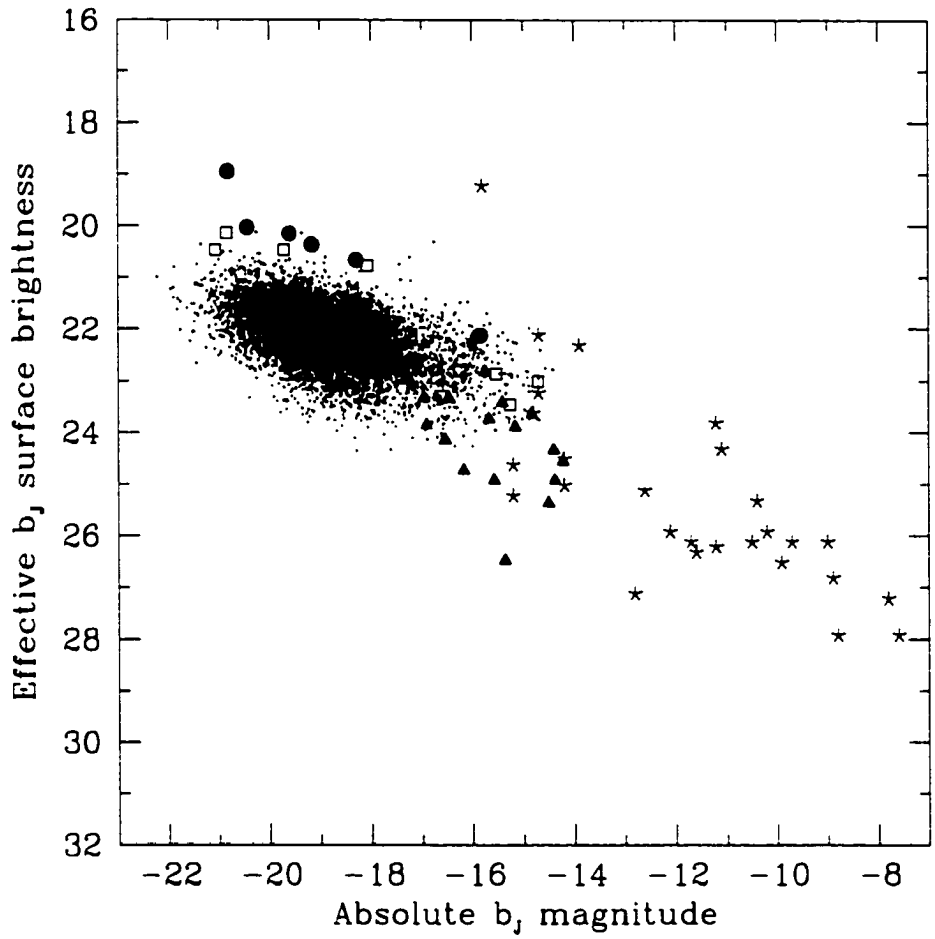

Figure 5.6: The bivariate brightness distribution from Driver & Cross (2000). Data from the 2dF survey are shown as small dots, galaxies from the local group are shown as stars and the other symbols show data from HDF's.

propagate to errors in the luminosity functions in two ways: First, they cause errors in the absolute magnitude of each galaxy. Since $M = m - \mu(z) - k(z,t)$, if both m, μ (which depends on redshift, z) and k (which depends on galaxy type, t) have errors, so will M. Second, the weighting each galaxy receives in the $1/V_a$ method is dependent on each galaxy's z_{max} which in turn is affected by errors in redshift and apparent magnitude.

The errors in the absolute magnitude will tend to flatten the luminosity functions. Take, for example, the simplest case of two absolute magnitude bins, one heavily populated and the other sparsely populated. Because of the errors in the absolute magnitude, some fraction of galaxies will be scattered from one bin to the other. If the fraction is the same for both bins, more galaxies will scatter from the heavily populated bin into the sparsely populated bin than will scatter the other way. The result will be to equalize the two bins. This effect, the Eddington bias, was first noted in connection with stellar parallaxes (Eddington, 1913) and was later generalized (Eddington, 1940). Note that errors in the absolute magnitudes occur even if there are no errors in the redshifts; errors in apparent magnitude cause similar difficulties. Thus, the problem arises in spectroscopic surveys; Efstathiou, Ellis & Peterson (1988) discuss it in the context of the local luminosity function. The errors in weighting are less serious; although they add to the uncertainty, they do not systematically affect the luminosity function.

Figure 5.7 illustrates the effects of observational errors on the luminosity function. In all the panels, the solid line is the B luminosity function of Loveday *et al.* (1992). The other lines show the effects of increasing errors in the redshift, the magnitudes and the types. The bottom right panel shows

the effects of the combination of all three errors. Note that one does not expect the local luminosity function to be valid for the redshift slice shown ($1.5 < z < 3.0$). Figure 5.7 is merely an illustration of the effects of errors. In fact, this particular redshift slice exaggerates the effect of type error on the k-corrections.

The Eddington bias can only be corrected statistically; individual galaxies cannot be corrected, just the final distribution. The procedure to correct the bias is as follows:

- Measure the luminosity function as before. Call this luminosity function $\Phi_0(M)$.
- Add the effects of all the errors in redshift, magnitude and type to Φ_0 (using a Monte Carlo routine) to produce a new (flatter) luminosity function. Call this luminosity function $\Phi'_0(M)$.
- For each bin, correct $\Phi_0(M)$ by an amount equal to $\Phi'_0(M) - \Phi_0(M)$. Call this luminosity function $\Phi_1(M)$.
- Again, add the effects of the errors to $\Phi_1(M)$ to produce $\Phi'_1(M)$.
- Correct $\Phi_1(M)$ by an amount equal to $\Phi'_1(M) - \Phi_0(M)$ to produce $\Phi_2(M)$
- Repeat n times until one obtains a luminosity function $\Phi_n(M)$, which, when the effects of the errors are added, reproduces $\Phi_0(M)$ closely enough that further iterations would be pointless.

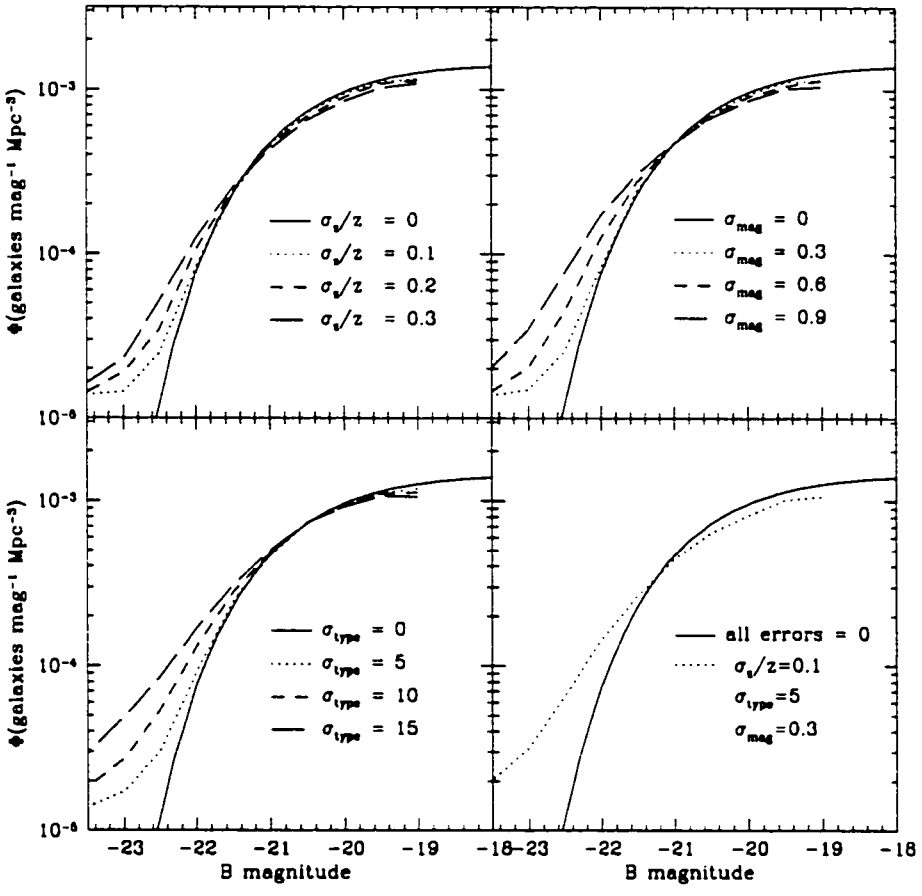

Figure 5.7: The effects of observational errors on the luminosity functions. In all the panels, the solid line is the B luminosity function of Loveday *et al.* (1992). The other lines show the effects of increasing errors in the redshift, the magnitudes and the types. The bottom right panel shows the effects of the combination of all three errors.

In practice only a few iterations ($n < 5$) are ever necessary. Each iteration adds some degree of noise, so excessive iterations are not advisable. Figure 5.8 illustrates the effects of this procedure. The solid line shows the real luminosity function (Loveday *et al.*, 1992). The dotted line shows this luminosity function with the effects of the errors added. The other lines show the effects of successive iterations of the procedure outlined above. By the second and third iterations, the match is quite good.

5.7 Luminosity functions

The procedure described above was applied to the luminosity functions generated in the previous sections. As discussed in Section 3.4 the redshift error is $\sigma_z/z = 0.11$ and the type error is $\sigma_{\rm type} = 7$ templates (that is, about plus or minus one Hubble type). For simplicity, an average magnitude error of $\sigma_{\rm mag} = 0.1$ magnitudes was adopted. As may be seen from the upper right hand panel of Figure 5.7, the effects of a magnitude error of only $\sigma_{\rm mag}$=0.1 will be quite small. Consequently, a more detailed treatment of the magnitude errors is not called for.

Figure 5.9 shows the results. A by-product of the Monte Carlo procedure described in Section 5.6 is that one can accurately assess the uncertainties. The error bars in Figure 5.9 reflect the effects of errors in redshift, type and magnitude as well as $1/\sqrt{N}$ Poisson statistics. These errors are added in quadrature with the cosmic variance measured by comparing the results from the HDFN and HDFS. The luminosity functions for the three lowest redshift slices show relatively little evolution, consistent with the results of Cowie,

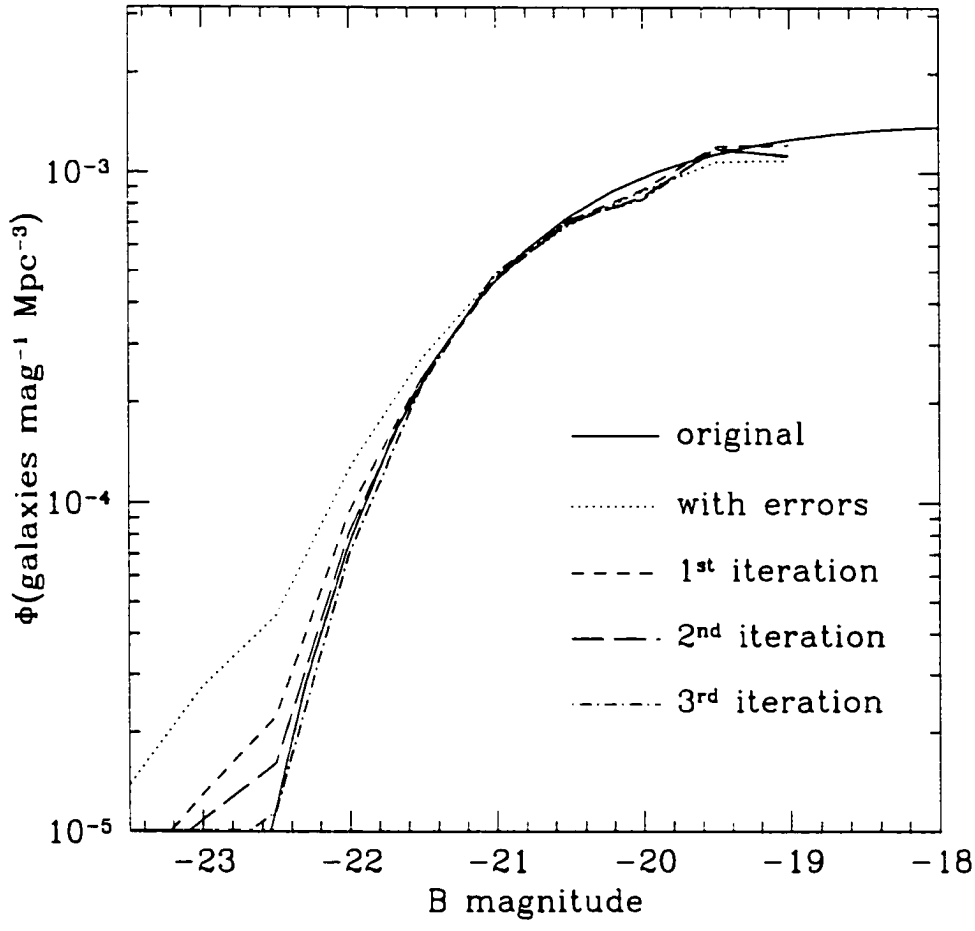

Figure 5.8: Removing the Eddington bias. The solid line is the B luminosity function of Loveday *et al.* (1992). The dotted line shows the effects of observational errors in redshift, magnitude and type (as per the lower right panel of figure 5.7). The following lines show the results of the iterative procedure used to correct these errors.

Songaila & Barger (1999). The luminosity function for the highest redshift slice ($3 < z < 6$) lies about a magnitude brighter than those for the lower redshift slices; that for the second highest ($1.5 < z < 3$) another half magnitude brighter still. This relatively small amount of evolution is at odds with the 3 magnitudes of luminosity evolution reported in Gwyn & Hartwick (1996). As was helpfully pointed out by Bershady *et al.* (1997), the k-corrections used in that article were based on SED's that were somewhat too red. Bershady *et al.*'s ground-based work (which is wide in sky-coverage but shallow in depth) is much more in line with the present luminosity functions.

Up until now, a H_0=65 $\mathrm{km\,s^{-1}Mpc^{-1}}$, $\Omega = 1$, $\Lambda = 0$ cosmology has been assumed. However, opinions diverge widely on the exact values of the parameters (Sandage, 1999; Mould *et al.*, 2000; Perlmutter *et al.*, 1999, for example). The details of the cosmology affect the determination of luminosity functions with the $1/V_a$ through Equations 5.2, 5.3 and 5.4. Therefore, some discussion of the effects of cosmology on the luminosity functions is warranted.

The luminosity functions were recomputed using four variant cosmologies, tweaking the various parameters to values that have been suggested by various authors.

- H_0=65 $\mathrm{km\,s^{-1}Mpc^{-1}}$, $\Omega = 1$
- H_0=65 $\mathrm{km\,s^{-1}Mpc^{-1}}$, $\Omega = 0.3$
- H_0=65 $\mathrm{km\,s^{-1}Mpc^{-1}}$, $\Omega = 0.3$, $\Lambda = 0.7$
- H_0=50 $\mathrm{km\,s^{-1}Mpc^{-1}}$, $\Omega = 1$

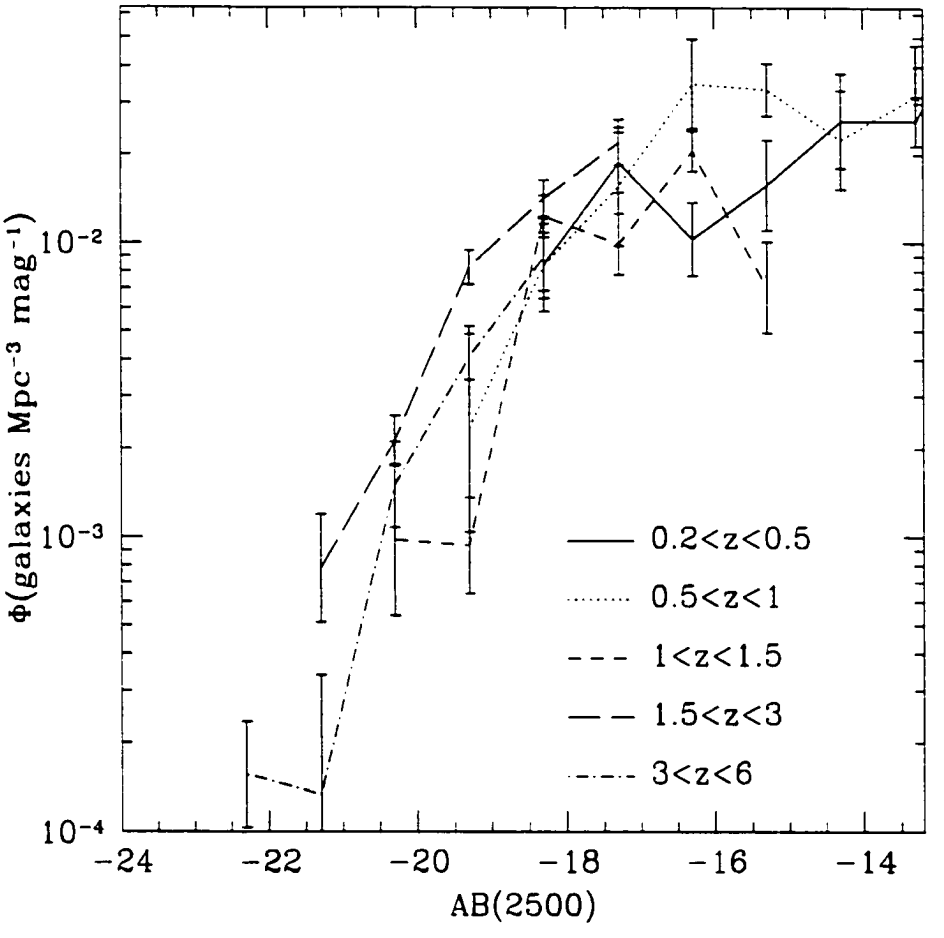

Figure 5.9: Luminosity functions for the Hubble Deep Fields. The different redshift slices are indicated by different line types. The error bars reflect measurement errors as well as cosmic variance.

The $1/V_a$ method was used, corrected for Eddington effects as described in the previous section. Figure 5.10 shows the results of these tests. Each panel shows a different redshift slice. Luminosity functions computed with different cosmologies are shown as different line types. Clearly, cosmology does systematically change the positions of the luminosity functions.

The real question, however, is whether changing the cosmology significantly changes the final results. Figure 5.11 shows that it does not. Each panel shows the luminosity functions for different cosmologies. Although the panels do show differences, overall the relative positions of the luminosity functions for different redshift slices remain similar.

5.8 Luminosity density

Having computed the luminosity functions for a series of redshift slices, computing the luminosity density of the Universe is quite easy. The luminosity function gives the number of galaxies per cubic megaparsec at a given absolute magnitude. Multiplying the luminosity function by the flux corresponding to this absolute magnitude, $F(M)$, one obtains the luminosity density function. Summing over the luminosity density function gives the luminosity density, L:

$$L = \int_{-\infty}^{+\infty} F(M)\Phi(M)dM. \tag{5.19}$$

Figure 5.12 shows the luminosity density function, $F(M)\Phi(M)$. Unlike the luminosity functions, which are flat or rising at the faint ends, the luminosity density function fall off at the faint ends. Faint galaxies, though numerous, do not contribute much light. Thus, integrating over the section of

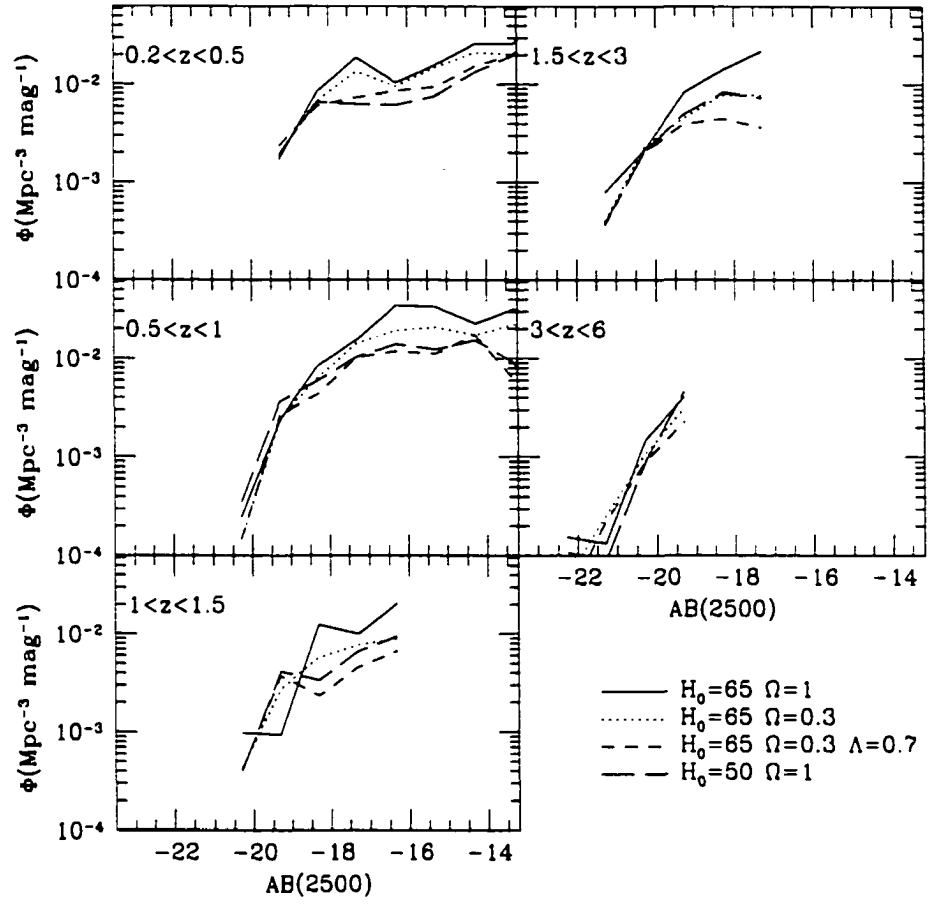

Figure 5.10: The effects of different cosmologies on the luminosity functions. Each panel shows a different redshift slice. Luminosity functions computed with different cosmologies are shown as different line types. Clearly, cosmology does change the positions of the luminosity functions. The error bars have been omitted for clarity.

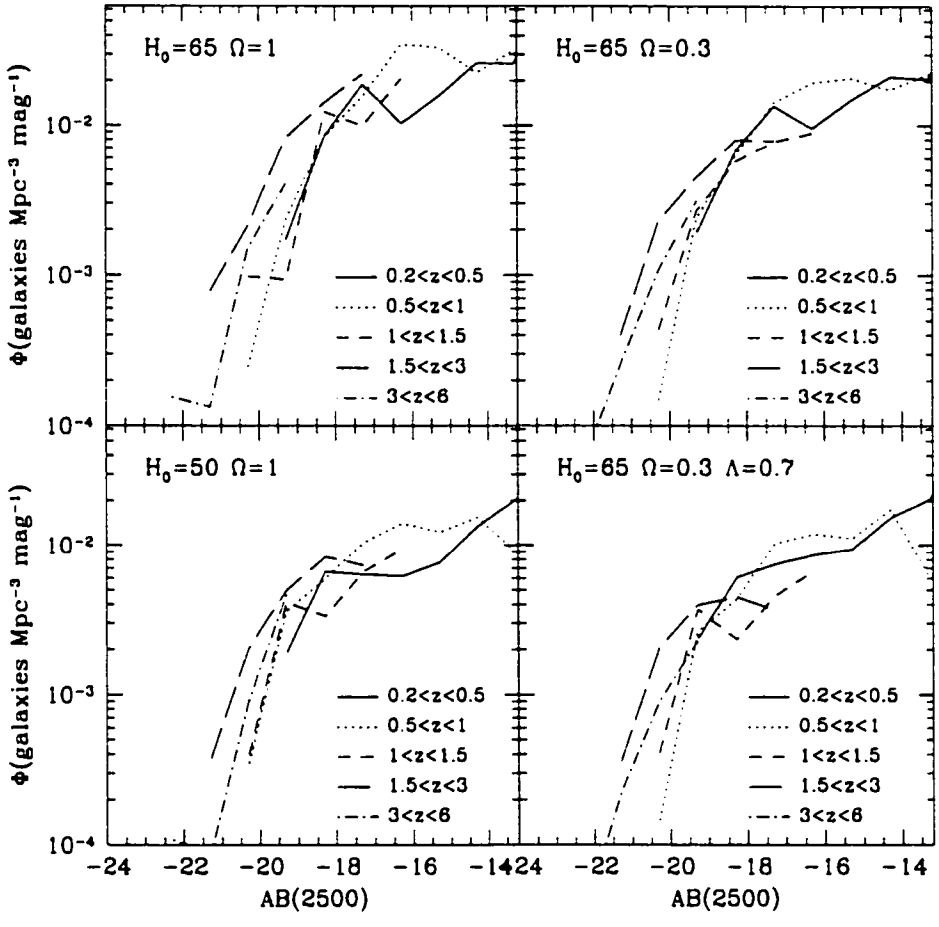

Figure 5.11: The effects of different cosmologies on the luminosity functions. Each panel shows the luminosity functions for different cosmologies. Although the panels do show differences, overall the relative positions of the luminosity functions for different redshift slices remain similar. The error bars have been omitted for clarity.

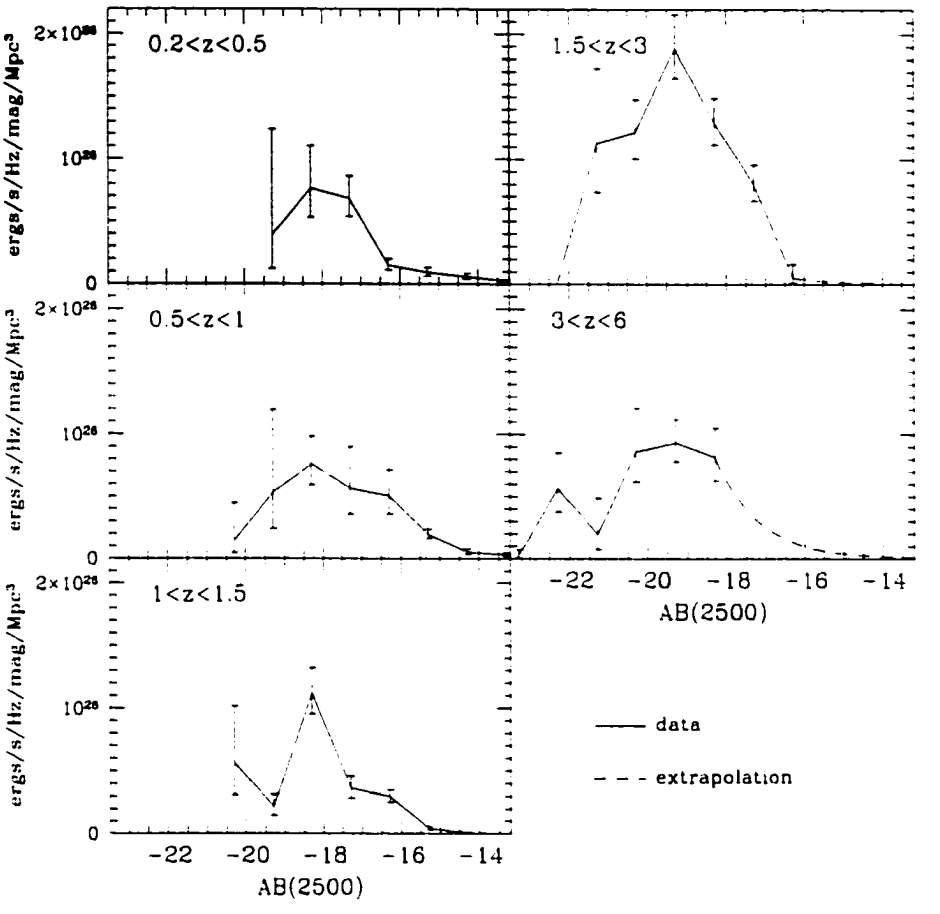

Figure 5.12: The luminosity density functions. The vertical axes represent the 2500Å flux density in the units shown. The dashed sections of each line show extrapolations from the data.

$F(M)\Phi(M)$ that is measured by the present sample should be a fairly complete measure of total luminosity density. The luminosity density functions of the highest redshift bin, however, is slightly incomplete at the faint end. To extend the luminosity function, it was assumed that it is well described by a Schecter function with $\alpha = -1$ (that is to say, flat at faint absolute magnitudes), normalized to the faintest observed point of the luminosity function. This correction amounts to 20% of the total luminosity density for the highest redshift bin. It amounts to less than 1% in the lower bins. In contrast, most spectroscopic samples require quite large extrapolations. The details of these extrapolations can cause sizable differences. For example in the spectroscopic sample of Cowie *et al.* (1999) changing the faint end slope of the luminosity function from $\alpha = -1.0$ to $\alpha = -1.5$ can cause a difference of a factor of 1.4 in the resulting luminosity densities, which is larger than the effect of ignoring the correction entirely in this photometric redshift sample. The dashed sections in Figure 5.12 show extrapolations from the data.

The luminosity density was calculated at different wavelengths to make it easier to compare the results with the luminosity densities given by different authors. Figures 5.13, 5.14, 5.15, and 5.16 show the integrated luminosity density at 1625Å, 2000Å, 2500Å, and 2800Å respectively. In all four figures, solid symbols indicate luminosity densities which have been corrected for dust obscuration (as discussed below in Sec. 5.9), while open symbols indicate the uncorrected luminosity densities.

At 1625Å (Fig. 5.13), the luminosity density at high redshift is slightly higher than the measurement of Madau *et al.* (1996). The difference may be due to the more detailed consideration of accessible volumes in the present

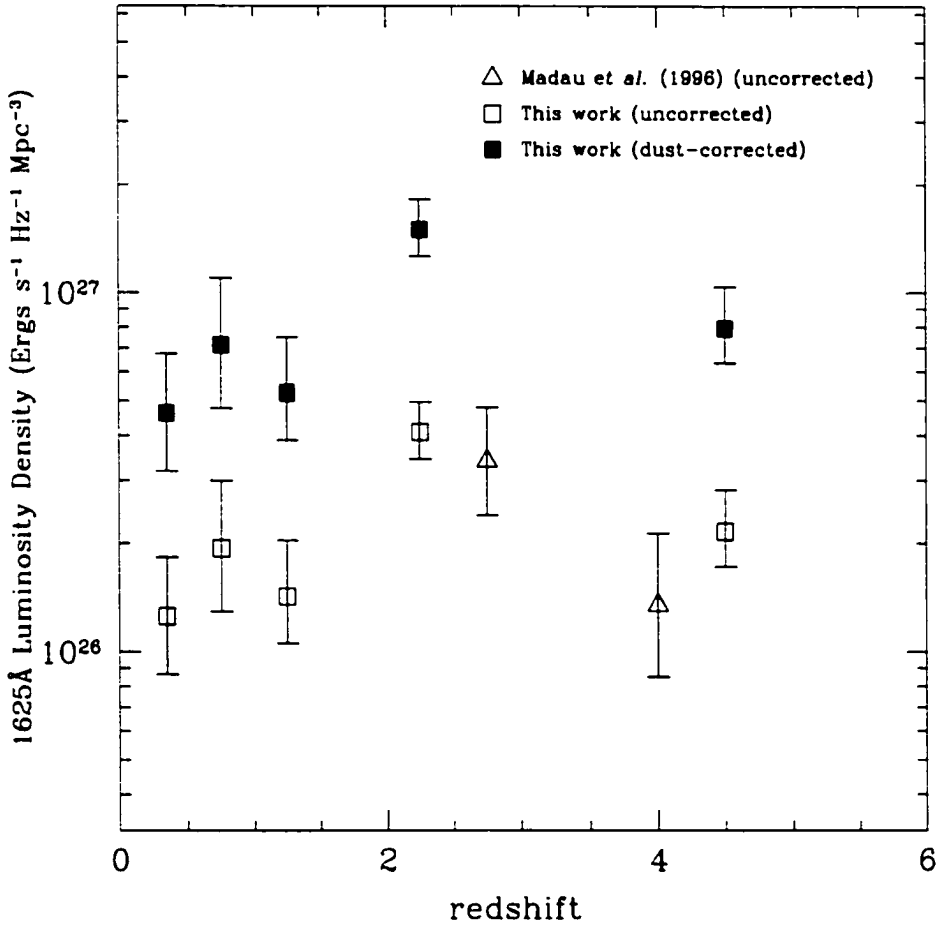

Figure 5.13: The luminosity density at 1625Å as a function of redshift

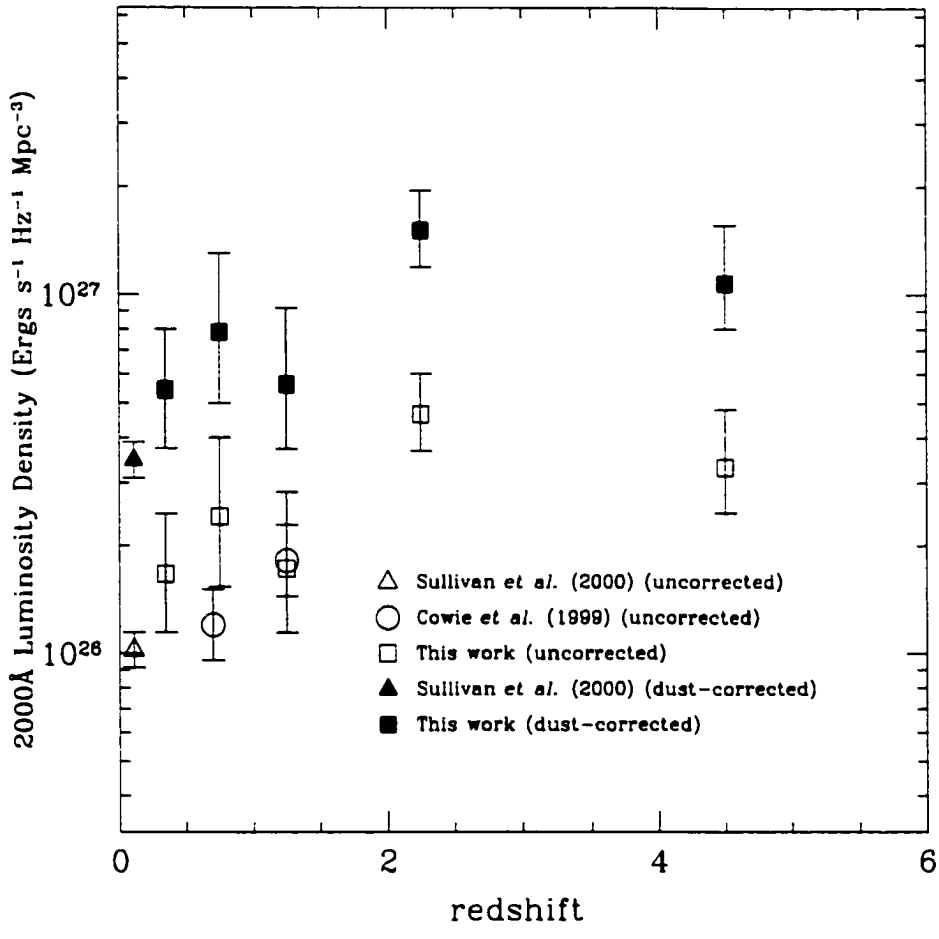

Figure 5.14: The luminosity density at 2000Å as a function of redshift

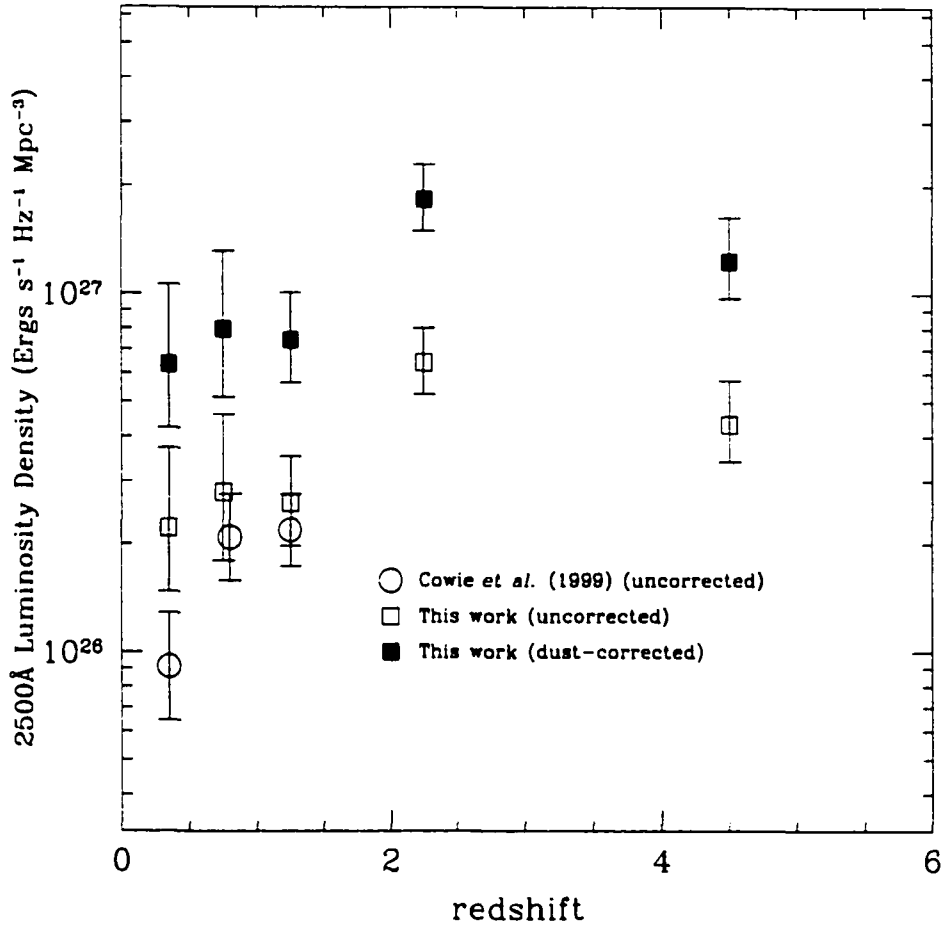

Figure 5.15: The luminosity density at 2500Å as a function of redshift

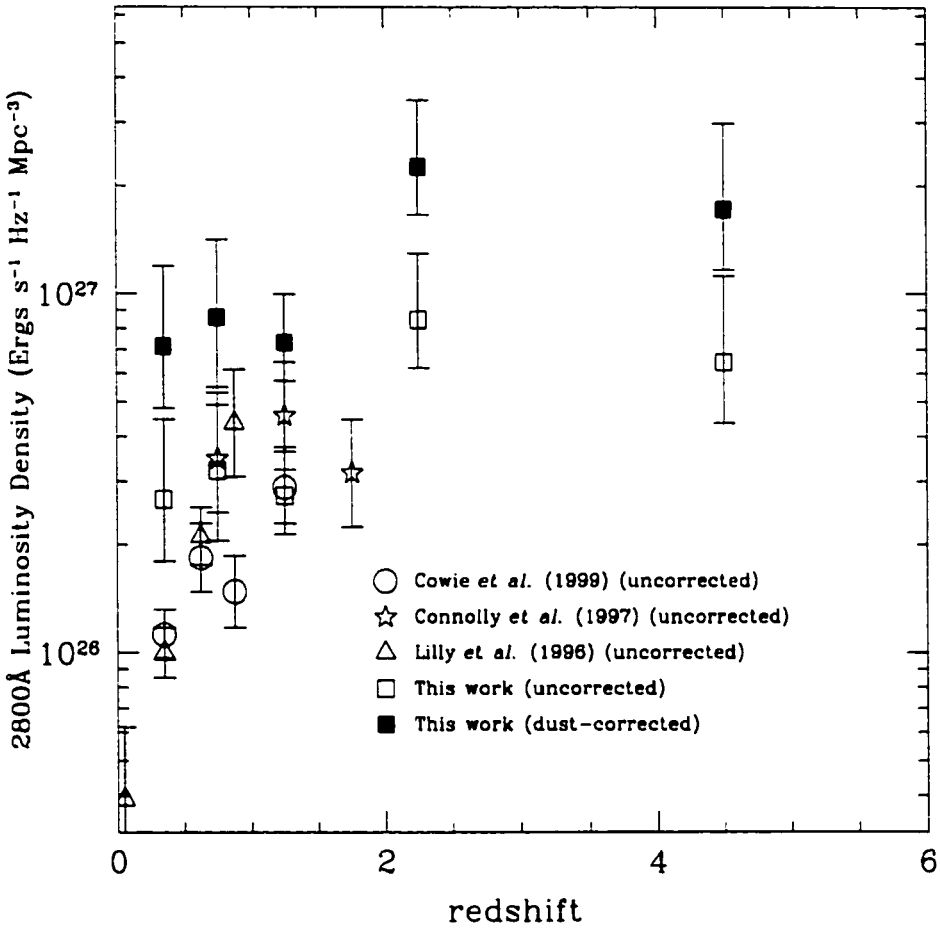

Figure 5.16: The luminosity density at 2800Å as a function of redshift

work. In the above discussion, each galaxy was given a weight according to its accessible volume. This volume is no larger than that of the redshift slice in question and is generally smaller. Madau *et al.* (1996) assume that "...this redshift interval has been uniformly probed...", effectively equating the accessible volume with the volume of the redshift slice. Since each galaxy has a weight equal to $1/V_a$, Madau *et al.*'s weights — and hence their luminosity densities — will be generally smaller than those determined when magnitude and surface brightness effects are taken into account.

At 2000Å and 2500Å(Figs. 5.14 and 5.15), the present determination of luminosity density are generally consistent with that of Cowie *et al.* (1999) and the local measurement of Sullivan *et al.* (2000).

At 2800 Å (Fig. 5.16) the luminosity density measurements are not unlike those of Lilly *et al.* (Lilly *et al.*, 1996) and Connolly *et al.* (1997). However the slope of the redshift-luminosity density relation is somewhat shallower than that found by Lilly *et al.* (Lilly *et al.*, 1996). A similar result is noted by Cowie *et al.* (1999) and Sullivan *et al.* (2000).

5.9 The effects of dust

The luminosity densities discussed above have not been corrected for effects of internal dust absorption. These effects are sizable at the UV wavelengths being considered here. Ideally, one would like to apply a dust correction to the UV luminosity of each galaxy individually. However, for the most part, it is not possible to measure the extinction in a galaxy using only broad band

colours.[1] Therefore, only an average correction can be applied.

Naively, one would expect that different types of galaxies would have differing amounts of dust absorption. One would expect later types to be more dusty, earlier galaxies, less so. To investigate the amount of dust absorption as a function of galaxy type, three samples were examined: the UV-selected sample of Sullivan *et al.* (2000), the sub-sample of the Canada-France Redshift Survey (CFRS) survey discussed by Tresse *et al.* (1996) and the survey of local galaxies of Kennicutt (1992). These three samples have all have photometry or visual morphologies, which can be used to determine type, and Hα and Hβ equivalent widths which can be used to measure extinction.

Extinction, parameterized by the colour excess, $E(B-V)$ can be determined by comparing the measured values of the Balmer line fluxes, $F(\mathrm{H}\alpha)$ and $F(\mathrm{H}\beta)$, to their expected values:

$$\begin{aligned}
\left.\frac{F(\mathrm{H}\alpha)}{F(\mathrm{H}\beta)}\right|_{\text{observed}} &= \frac{10^{-0.4A_\alpha}}{10^{-0.4A_\beta}} \times \left.\frac{F(\mathrm{H}\alpha)}{F(\mathrm{H}\beta)}\right|_{\text{emitted}} \\
&= 10^{-0.4(A_\alpha - A_\beta)} \times \left.\frac{F(\mathrm{H}\alpha)}{F(\mathrm{H}\beta)}\right|_{\text{emitted}} \\
&= 10^{-0.4E(B-V)(X_\alpha - X_\beta)} \times \left.\frac{F(\mathrm{H}\alpha)}{F(\mathrm{H}\beta)}\right|_{\text{emitted}} \qquad (5.20)
\end{aligned}$$

where A_λ is the extinction in magnitudes and $X(\lambda) \equiv A_\lambda / E(B-V)$ is the extinction law. Equation 5.20 can be rearranged to give

$$E(B-V) = \frac{-2.5 \log\left(\left.\frac{F(\mathrm{H}\alpha)}{F(\mathrm{H}\beta)}\right|_{\text{observed}} \Big/ \left.\frac{F(\mathrm{H}\alpha)}{F(\mathrm{H}\beta)}\right|_{\text{emitted}} \right)}{(X_\alpha - X_\beta)} \qquad (5.21)$$

[1] The exception is the special case of starburst galaxies, which have very similar intrinsic SED's. It is possible to relate the UV spectral slope of starburst galaxies to their extinction (Meurer *et al.*, 1999).

The ratio of the emitted Balmer line strengths is known theoretically to be $F(\mathrm{H}\alpha)/F(\mathrm{H}\beta) = 2.86$, for case B recombination and a nebular temperature of 10 000 K and a density of 100 cm^{-3} (Osterbrock, 1989). The extinction law is well known at optical wavelength: Seaton (1979) gives $A_\alpha - A_\beta = 1.19$; Calzetti (1997) gives a similar value. Thus if $F(\mathrm{H}\alpha)/F(\mathrm{H}\beta)$ can be measured for a galaxy, its extinction can be known.

The Hα and Hβ equivalent widths must be corrected for stellar absorption. More properly, this is the drop in the galactic continuum underneath the nebular emission lines due to Balmer absorption in the stellar atmospheres.

The sample of Sullivan *et al.* (2000) and Treyer *et al.* (1999) is selected in the UV with a filter centred at 2000Å. The median redshift of the sample is about $z = 0.1$. From the information in these papers, it is possible to derive $E(B-V)$ for each galaxy in the sample. They also list galaxy type, determined by comparing the rest-frame UV-B colour to the spectral templates of Poggianti (1997). These types were adopted, rather than re-determining the type based on the templates described in Section 3.3.

The sample of Tresse *et al.* (1996) consists of those galaxies in the CFRS sample with redshifts less than $z = 0.3$. Their Table 2 lists A_V (= $3.2 \times E(B-V)$), as calculated from Hα and Hβ (corrected for stellar absorption), so no further calculations are needed to determine the dust content. The type of each galaxy was determined by comparing its given $V-I$ colour to spectral templates. Again, the templates used were those adopted by the authors (in this case the GISSEL models (Bruzual & Charlot, 1993) were used) rather than the templates used in this thesis.

Kennicutt's (1992) sample is a set of local, $z < 0.02$, galaxies. The

tabulated values of Hα and Hβ equivalent widths were corrected for stellar absorption. Regrettably, there was insufficient information to make individual corrections for each galaxy: an average correction of 5Å was applied. On the other hand, corrections were made for the contamination of the Hα line for the nearby [NII] line. The corrected Hα and Hβ were used to determine $E(B-V)$ using Equation 5.21. Kennicutt gives visually classified morphologies for all the galaxies in his sample.

Figure 5.17 shows $E(B-V)$ plotted against galaxy type for the three samples. There is a considerable amount of scatter: $E(B-V)$ ranges from 0 to 0.8; this corresponds to a range in A_V from 0 to 2.56, in agreement with other authors. The surprising thing about Figure 5.17 is that there does not appear to be any correlation of extinction with galaxy type. This is true if type is determined by colour (as in the Sullivan *et al.* (2000) and the Tresse *et al.* (1996) samples) or by visual morphology (as in the Kennicutt (1992) sample). Although the scatter for each type is large, the median is remarkably constant. As shown in Table 5.1, the median values of $E(B-V)$ for each of the three samples are quite similar.

Table 5.1: Median $E(B-V)$ for various samples

Sample	$E(B-V)$	$\sigma_{E(B-V)}$
Sullivan *et al.* (2000)	0.30	0.13
Tresse *et al.* (1996)	0.30	0.22
Kennicutt (1992)	0.33	0.12

A dust correction of $E(B-V)$=0.3 was adopted for all galaxies. Adopting the Calzetti (1997) reddening law, this translates to an extinction at 2500Å of

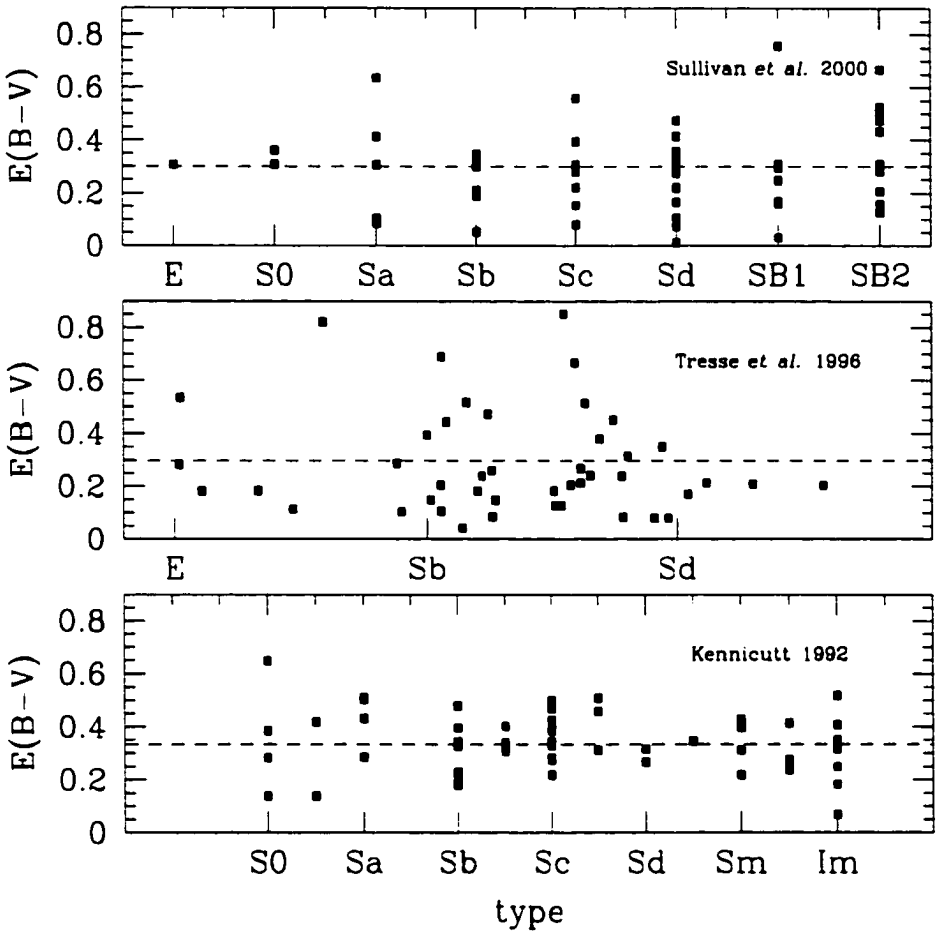

Figure 5.17: $E(B-V)$ as a function of galaxy type for different samples. In the Sullivan *et al.* sample, (2000) galaxy type is determined by rest UV(2000)-B colour. In the Tresse *et al.* (1996) sample, galaxy type is determined by rest $V-I$ colour. In the Kennicutt (1992) sample, galaxy type is based on visual morphology (not colour). There does not appear to be a correlation of $E(B-V)$ with galaxy type. The horizontal lines show the median values of $E(B-V)$.

$A_{2500} = 1.14$ magnitudes. This amounts to a correction to the UV luminosity density of about a factor of three. Although it would be preferable to apply an individual correction for each galaxy, this is not feasible unless Hα and Hβ are measured for each galaxy. This is obviously not feasible for a photometric redshift survey. The dust-corrected luminosity densities are shown as filled squares in Figures 5.13, 5.14, 5.15, and 5.16.

5.10 Star formation rates

The far UV light of a galaxy is dominated by the brightest, bluest stars of the main sequence. Because these stars have a short life-time, and therefore must have been recently formed, the UV luminosity of a galaxy is a good measure of the star formation rate (SFR) of a galaxy. UV luminosity, L_{UV}, is directly proportional to SFR:

$$\text{SFR } (M_\odot \text{yr}^{-1}) = \text{constant} \times L_{UV}(\text{ergs s}^{-1}\text{Hz}^{-1}) \qquad (5.22)$$

The value of the constant in Equation 5.22 must be determined from theoretical models of galaxy spectral evolution. Fortunately, the constant is not sensitive to the details of the construction of these models, nor is it sensitive to the prior star formation history of a galaxy. Unfortunately, it is sensitive to one's choice of initial mass function (IMF). The choice of IMF is the largest single source of uncertainty in the measurement of star formation rates. The constant depends somewhat on exactly which part of the UV continuum is being measured. Values of the constant are summarized in Table 5.2 for the Scalo (1986) and Salpeter (1955) IMF's as given by Madau, Pozzetti & Dickinson (1998).

Table 5.2: Conversion of UV density to SFR

IMF	Wavelength	constant
Scalo	1500Å	2.86×10^{-28}
Scalo	2800Å	1.96×10^{-28}
Salpeter	1500Å	1.25×10^{-28}
Salpeter	2800Å	1.27×10^{-28}

The UV luminosity densities at 2500Å from Figure 5.15 were converted into star formation rate densities by adopting a Salpeter IMF. The results are shown in Figure 5.18 as solid squares. Since the conversion is a simple multiplication, the relative evolution of the SFR density is exactly the same as the that of UV luminosity density. That is to say, it is fairly constant at high redshift, and drops slowly below $z = 1.5$

Star formation rates have been measured from dust-corrected UV luminosities by other authors. The high redshift results of Madau *et al.* (1998) and Steidel *et al.* (1999), as well as the local results of Sullivan *et al.* (2000) are also shown in Figure 5.18 as various four-sided points. Except for the highest redshift point of Madau *et al.*, they are consistent with the results of the present photometric sample.

There are several ways to measure the SFRD at other wavelengths. Star formation rates have been measured using observations at sub-millimetre wavelengths. When dust in galaxies absorbs light at UV wavelengths it is heated. The dust then radiates thermally at a broad range of wavelengths from the far-infrared to the sub-millimetre (8-1000μm) with a peak at $\sim$ 60μm. The integrated luminosity over these wavelengths is related to star

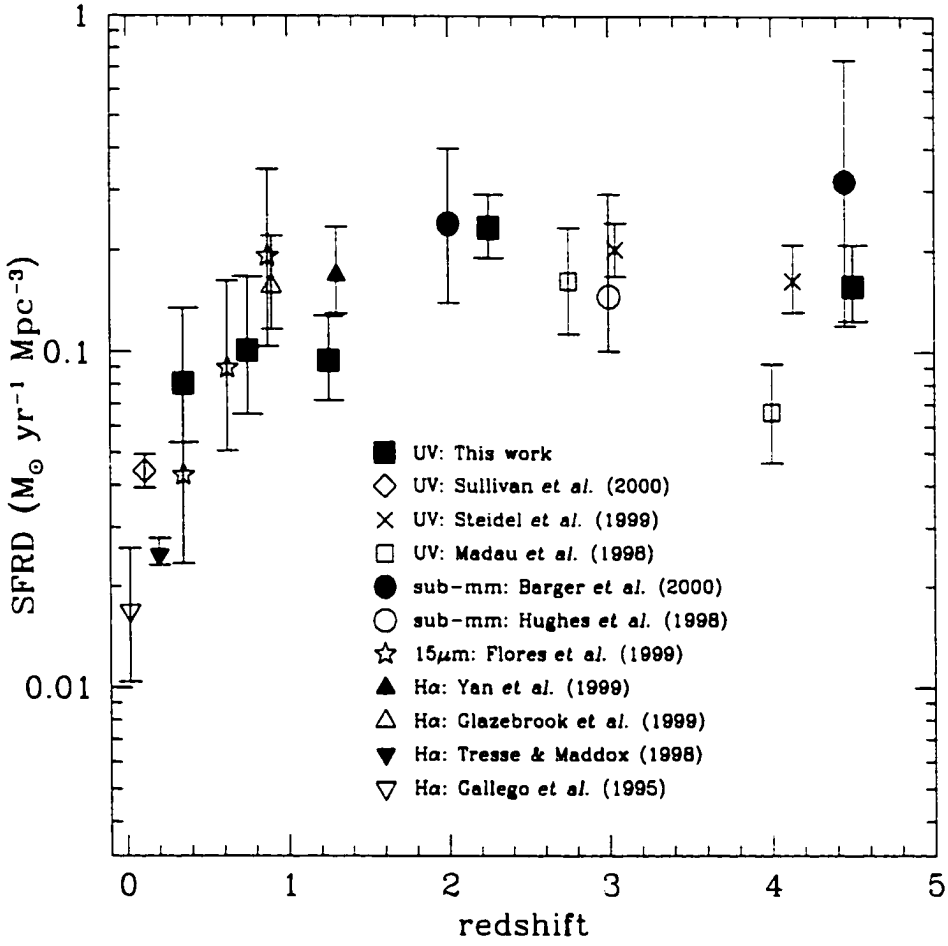

Figure 5.18: Evolution of the star formation rate density of the Universe as measured by different methods. The SCUBA sub-mm measurements are shown as circles. Hα measurements are shown as triangles. The 15μm measurements are shown as stars. UV measurements are shown as various four-sided symbols.

formation rate by

$$\text{SFR } (M_\odot \text{yr}^{-1}) = 4.5 \times 10^{-44} \times L(\text{IR})(\text{ergs s}^{-1}) \quad (5.23)$$

(Kennicutt, 1998). The advent of the Sub-millimetre Common User Bolometric Array (SCUBA) has made it possible to measure the flux at 850μm. Measurements at this wavelength can be extrapolated to measure the full integrated IR flux and hence the star formation rate. As an interesting[2] aside, because the sub-mm images are of such low resolution, it is often hard to make reliable optical identifications. This means that it is sometimes hard to assign a redshift to the objects. However, radio identifications have been made at 21cm, so it is possible to determine "millimetric redshifts". A redshift is determined by comparing the flux ratio F(850μm)/F(21cm) to the flux ratio that one obtains by redshifting a template galaxy (Arp 220). The sub-mm measurements of the SFR from Hughes *et al.* (1998) and Barger, Cowie & Richards (2000) are shown on Figure 5.18 as circles.

Similarly, one can extrapolate from the flux at 15μm to measure the total luminosity from dust and hence measure star formation rates. This was done by Flores *et al.* (1999) who used the Infrared Space Observatory (ISO) to obtain images of a CFRS field. The resulting star formation rates at $z < 1$ are shown as stars in Figure 5.18.

Finally, star formation rates have been measured using Hα fluxes. Almost all the UV light shortwards of the Lyman limit emitted by young hot stars in a galaxy is absorbed by interstellar hydrogen and re-emitted in recombination lines. Thus, measuring the strength of these lines is a measurement

[2]interesting at least to photometric redshift aficionados

of the UV luminosity shortwards of 912Å, which is a measurement of the star formation rate. In principle any recombination line could be used. However, the Paschen lines lie in the infrared and are difficult to measure, and the Lyman series are strongly affected by dust. Thus most such measurements are done using the strongest Balmer line, Hα, which is only weakly affected by dust. Hα luminosity $L(\mathrm{H}\alpha)$ is converted into a star formation rate thus:

$$\mathrm{SFR}\ (M_\odot \mathrm{yr}^{-1}) = 7.9 \times 10^{-42} \times L(\mathrm{H}\alpha)(\mathrm{ergs\ s}^{-1}) \qquad (5.24)$$

(Kennicutt, 1998). Gallego *et al.* (1995) made a local determination of the SFR from Hα measurements. At slightly higher redshifts, Tresse & Maddox (1998) did the same for a sample of CFRS galaxies at $z < 0.3$. At higher redshifts, the Hα line moves into the infrared, making observations more difficult. However, two measurements have been at $z \sim 1$: Glazebrook *et al.* (1999) used the CGS4 infrared spectrograph on UKIRT to observe CFRS galaxies and Yan *et al.* (1999) made measurements using slitless spectroscopy with NICMOS on HST. The star formation rate determined by these surveys are shown as triangles on Figure 5.18

All the measurements discussed above assume or have been corrected to a H_0=65 $\mathrm{km\,s^{-1}Mpc^{-1}}$, $\Omega = 1$, $\lambda = 0$ cosmology. The general shape of Figure 5.18 is not changed by altering this cosmology. Star formation is directly proportional to luminosity density. Luminosity density is directly proportional to the square of the luminosity distance d_L and inversely proportional to the comoving volume element dV/dz. That is to say, $\mathrm{L} \propto d_L^2 (dV/dz)^{-1}$. Although dV/dz is very sensitive to cosmology, this sensitivity is partially cancelled out by the d_L^2 term. Thus, changes in H_0 alter the SFRD by a

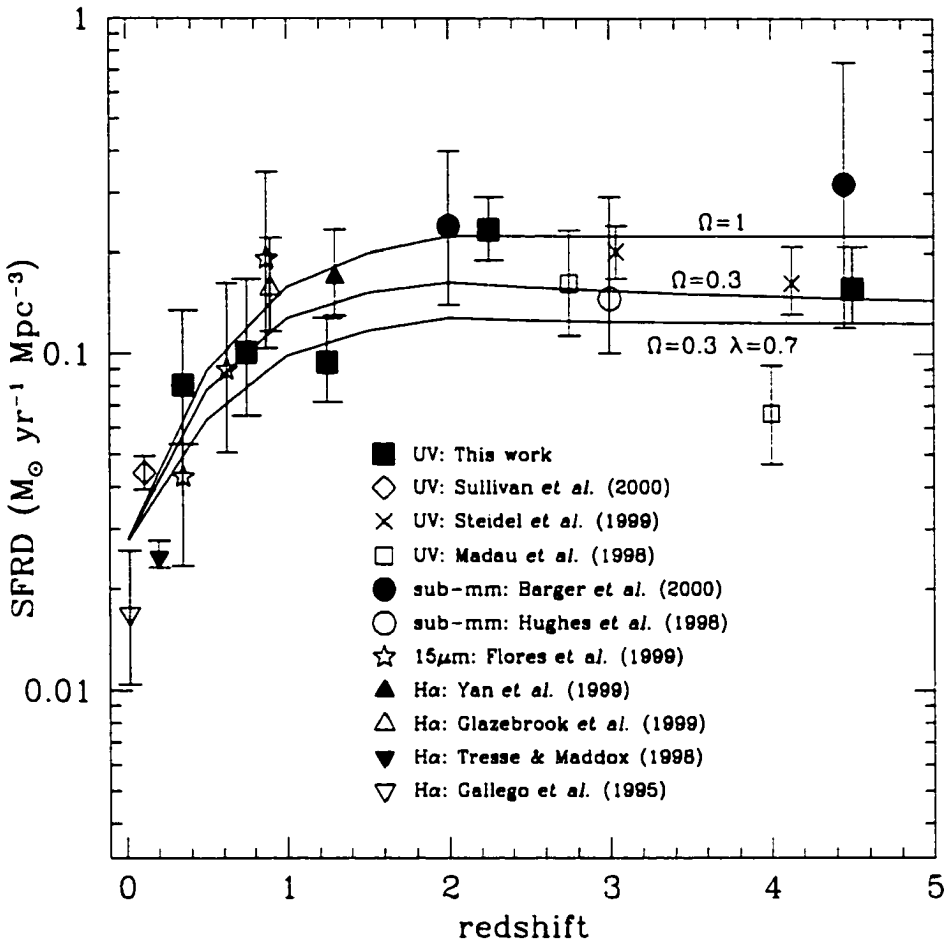

Figure 5.19: The effects of cosmology on estimates of the evolution of the star formation rate density. The same as Figure 5.18 but with the addition of lines showing the effects of differing cosmologies as labeled. Changing the values of Ω and λ has little effect on estimates of the star formation rate.

factor of $H_0/65$, which translates to a simple vertical shift in Figure 5.18. The effects of changing Ω and λ are shown in Figure 5.19. The solid lines show the evolution of the SFRD for various cosmologies, as labeled. Even at high redshift, the difference between the two extremes (Ω=1, λ=0 *vs.* Ω=0.3, λ=0.7, k=0) is smaller than the typical uncertainties of each measurement.

The different measurements of the SFRD shown in Figure 5.18 are quite consistent, with one or two exceptions. The highest redshift point of Madau *et al.* (1998) was discussed earlier. There is also a general disagreement at low redshift between the UV measurements and Hα measurements. However, given that all the methods of measuring the SFRD are subject to systematic uncertainties on the order of a factor of two, Figure 5.18 shows a remarkable consistency. Although several authors have claimed that the star formation seen in the sub-millimetre occurs in a separate population of unusually bright and dusty objects, visible only in the sub-mm, Adelberger & Steidel (2000) have shown that a single population of normal starburst galaxies can account for all the sub-millimetre observations as well as the UV observations. Indeed, Figure 5.18 shows that the sub-mm and UV observations give consistent answers even though they measure star formation in very different ways.

The general picture shown in Figure 5.18 would appear to be one where the Universe forms stars at a constant rate until a point around $z \sim 1.5$ when star formation begins to decay. But if the same data are plotted against the age of the Universe instead of redshift, as shown in Figure 5.20, a different picture emerges. Plotting in this manner compresses the high redshift points (where the SFRD appeared flat) considerably. Now it appears that the best description of the star formation history of the Universe is an exponential

decay with a time constant of $\tau \simeq 4$ Gyr.

That the SFR should decay exponentially is perhaps not surprising. If the rate at which gas is converted into stars is proportional to the amount of gas available in an individual galaxy, then the amount of gas will decline exponentially. If $M_{\rm gas}$ is the mass of gas in a galaxy and $C = 1/\tau$ is a proportionality constant, then one can write:

$$\frac{dM_{\rm gas}}{dt} \propto -CM_{gas}. \tag{5.25}$$

The solution to this differential equation is $M_{\rm gas} \propto \exp(-Ct) \propto \exp(-t/\tau)$. Since the rate at which stars are formed is the same at which gas is depleted the star formation rate, SFR $= \frac{dM_{\rm stars}}{dt} = -\frac{dM_{\rm gas}}{dt}$ will also decline exponentially in this simplified case.

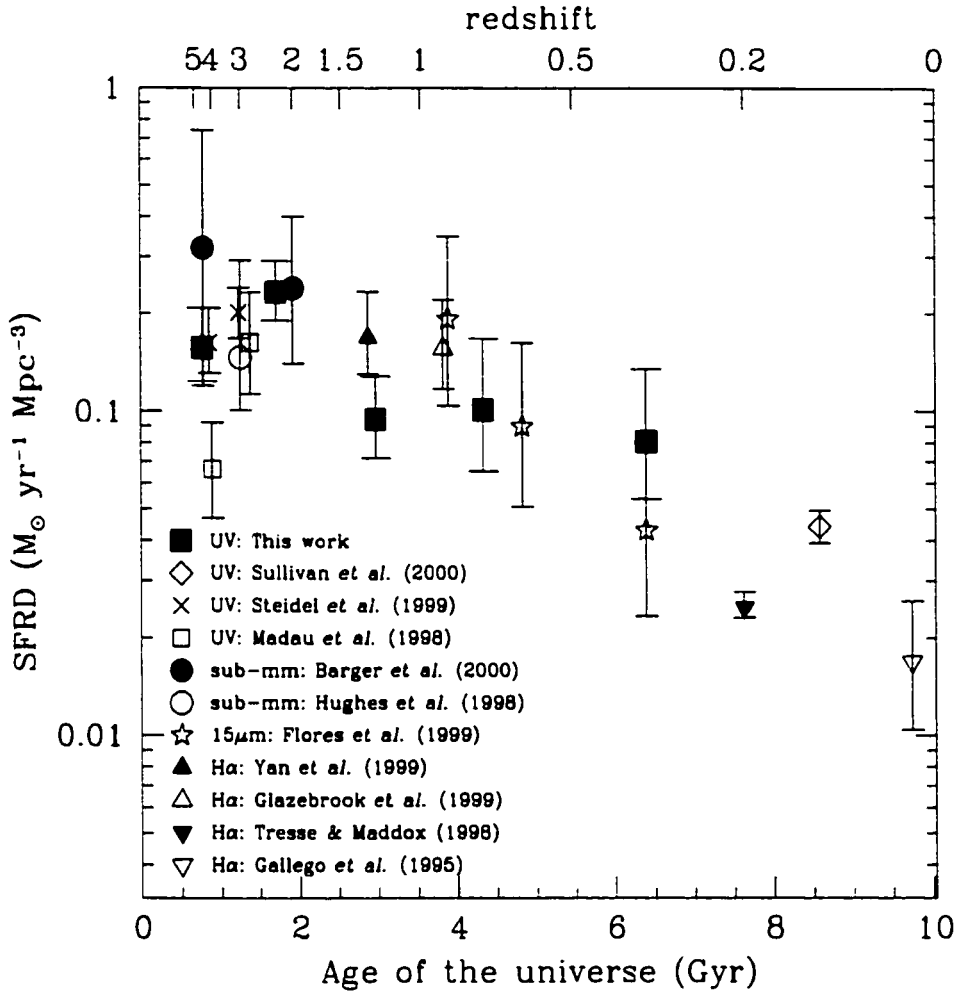

Figure 5.20: Star formation rate density as a function of age of the Universe. The symbols have the same meaning as in Figure 5.18

Chapter 6

Merging

This chapter examines the change in the number density of galaxies using the V/V_{max} statistic and the B band luminosity function.

The V/V_{max} statistic is a robust way of measuring the density and/or luminosity evolution of a population of objects. In this chapter, it is used as a first attempt to get some idea of the nature of the density evolution. While the V/V_{max} statistic is robust, it lacks subtlety. To investigate the merging history of galaxies more carefully, one must instead examine the evolution of the luminosity function.

In the simplest case, all galaxies would have a fixed absolute magnitude. In this case, it would be easy to calculate the merger rate. One would just measure the space density of galaxies at $z = 5$ (as measured by the luminosity function), and again at $z = 0$. The difference would be due to the mergers: if there were twice as many galaxies at $z = 5$ than at $z = 0$, then every galaxy must be the product of the merger of two progenitors. In this case, even though the number density of galaxies would decline with time, the number of stars (as measured by the luminosity density) would remain constant.

In reality, the situation is much more complicated. In addition to fading, galaxies also age with time, becoming redder. As time goes on, the red galaxies will become more numerous at the expense of the blue galaxies. Furthermore, the total number density of galaxies cannot be calculated. The luminosity function does not drop off at the faintest observable magnitudes; any integral over a faint end extrapolation will be infinite. Despite these complicating factors, it is still possible to deduce the merger rate from the evolution of the B band luminosity function by introducing a simple model for the data.

Working in the B band represents a compromise. Ideally, one would like to work in an infrared band, such as K, which is an excellent tracer of total stellar mass, and is not much affected by transitory bursts of star formation. Working in K, however, represents an extrapolation from the HST F814W filter of a factor of 2 in wavelength, even at $z = 0$. Thus, in order to minimize the k-corrections, one would like to work in the ultraviolet. Measuring magnitudes at 1500Å, as in Chapter 5, one does not have to extrapolate the SED of a galaxy beyond the F814W filter until $z = 4.5$. But UV flux closely traces star formation and the number of hot stars, rather than the stellar population in general. The B band is intermediate to these two extremes: it is more quiescent than the 1500Å and requires smaller k-corrections than the K band. Furthermore, generating luminosity functions in B allows one to compare results with the large number of B band luminosity functions in the literature.

For this chapter, the galaxy sample was split by colour into a red sample and a blue sample. The template fitting method described in Section 3.3

determines a galaxy type at the same time it measures a photometric redshift. This assigned type is used to make the colour cut. Those galaxies whose photometry best matches the SED of a Sbc galaxy or earlier are assigned to the red sample. Those with later types are assigned to the blue sample. This cut at Sbc is the same one adopted by the Canada-France Redshift Survey (Lilly *et al.*, 1995a, CFRS), so data from that survey can easily be incorporated to the present analysis. Locally, Sbc is roughly the median colour: splitting at this type divides the sample into two roughly equal groups at low redshift. At high redshift of course, most galaxies are blue: by $z \sim 3$, there are no red galaxies at all. Type can only be determined for the galaxies out to $z = 4.5$: at higher redshifts, the galaxies become R band drop-outs. Without the colour information afforded by $R - I$, the type assigned by the template fitting method is meaningless. Therefore, those galaxies with $z > 4.5$ were excluded from the sample. Since there are only 8 such galaxies in the total sample of 1694, it is unlikely that this will have much of an impact on the results.

6.1 The V/V_{max} statistic

The V/V_{max} statistic is a measure of the radial position of an object within the volume available to it in a sample. It is related to the $1/V_a$ method for determining luminosity functions discussed in Chapter 5. V is the volume enclosed within the radius at which the object lies: V_{max} is the volume within the maximum radius at which the object *could* lie and still be included in the sample. The value of V/V_{max} for a given galaxy can vary anywhere from zero

to one. A value of zero for V/V_{max} means that galaxy lies directly on top of the observer or at the inner limit of the sample. A value of one means that the object was almost too distant to make it into the sample. If the objects in a sample are evenly distributed in space and if the luminosity function of the population does not change over the region being surveyed, then the mean value of V/V_{max} should be $\langle V/V_{max} \rangle = 0.5$; the distribution of V/V_{max} should be a flat, boxcar distribution from 0 to 1. If the distribution of V/V_{max} is not flat, then either some evolution either in luminosity or density is occurring or the volumes have not been calculated correctly.[1] This is most obvious for a purely volume-limited sample in a Euclidean cosmology. Clearly, if the objects are evenly distributed in this space, half the objects will lie in the closest half of the volume and half the objects will lie in the far half.

The V/V_{max} method was devised by Schmidt (1968), who used it to show that quasars are not uniformly distributed in space, but were more common at the high redshift end of his sample. The method was used more recently to show that gamma ray bursters lie outside the galaxy (Meegan *et al.*, 1992; Schmidt *et al.*, 1988) before any GRB redshifts had been measured.

For a given object, the volumes are calculated using Equation 6.1:

$$V = \int_{z_{min}}^{z_{max}} \frac{dV}{dz} dz \tag{6.1}$$

The limits depend on the sample criteria. Although the original V/V_{max} (Schmidt, 1968) statistic was defined in terms of a purely magnitude-limited sample, V/V_{max} can be used for any sample whose limits are defined in any way using any criteria, provided those limits are well-defined. As long as

[1] For example, if the wrong cosmology is assumed.

exactly the same cuts that are applied to the sample are applied to the volumes. V/V_{max} is a valid statistic. In general, z_{min} will be zero for both V and V_{max}. However, if the sample has a lower redshift limit then z_{min} will be that limit. For V, z_{max} is the redshift of the object in question. For V_{max}, z_{max} is the highest redshift that the object could be at and still be included in the sample. If the sample is volume-limited, then z_{max} will be the high redshift limit. If the sample is magnitude-limited, then z_{max} is determined using Equation 5.4. If the sample is surface brightness-limited, then z_{max} is determined using Equation 5.18. More generally, a sample can be defined by a combination of these limits; in which case, z_{max} will be the smallest of the limits.

It was shown in Section 5.5 that surface brightness effects are not important for the $1/V_a$ method because the galaxies were split into multiple redshift bins. Panel (d) of Figure 5.4 shows this clearly. However, in the case of the V/V_{max} method, these redshift bins are not present and surface brightness limits are relevant and cannot be ignored. In panel (c) of Figure 5.4, it can be seen that — in the absence of bins — the maximum redshift determined by the limiting magnitude and the maximum redshift determined by both the limiting magnitude and the limiting surface brightness are significantly different.

Because V/V_{max} is a ratio, one does not have to worry about the angular size of the sample. Further, in the case where the k-corrections are negligible and where the volumes are in Euclidean space, it is not even necessary to know the distances to the objects. In the more general case, the fact that it is a ratio means that V/V_{max} is a more robust statistic when there are

uncertainties in the redshifts of the objects in the sample.

The uncertainty associated with the average value of V/V_{max} , $\sigma_{\langle V/V_{max}\rangle}$, is given by:

$$\sigma_{\langle V/V_{max}\rangle} = \frac{1}{\sqrt{12N}}. \tag{6.2}$$

where N is the number of objects in the sample.

The V/V_{max} statistic was measured for the HDF sample, split by colour as described above. Figure 6.1 shows the results. The left panel shows the range of V/V_{max} for the blue galaxies. The average value of $\langle V/V_{max} \rangle = 0.53 \pm 0.01$ shows that there are more blue galaxies in the further half of the sample. The Kolomogorov-Smirnoff test was applied to the sample. The probability that the V/V_{max} distribution is consistent with a uniform distribution is 4.04×10^{-13}, indicating that evolution is definitely occurring. The right panel shows the V/V_{max} distribution for the red galaxies. The red galaxies are clearly evolving the other way: with more red galaxies in the near half of the sample, the average value is $\langle V/V_{max} \rangle = 0.44 \pm 0.02$. The overall picture is that the blue galaxies are steadily increasing in number with distance, while the red galaxies are decreasing in number. If distance is viewed as the converse of the age of the Universe, then the blue galaxies are decreasing in number with time and the reds are increasing. This result, although robust, is somewhat vague. There is no indication whether the blue galaxies are disappearing because they are becoming red galaxies or whether they are decreasing in number densities due to mergers. For a more detailed picture, it is necessary to turn to an analysis of the B luminosity functions.

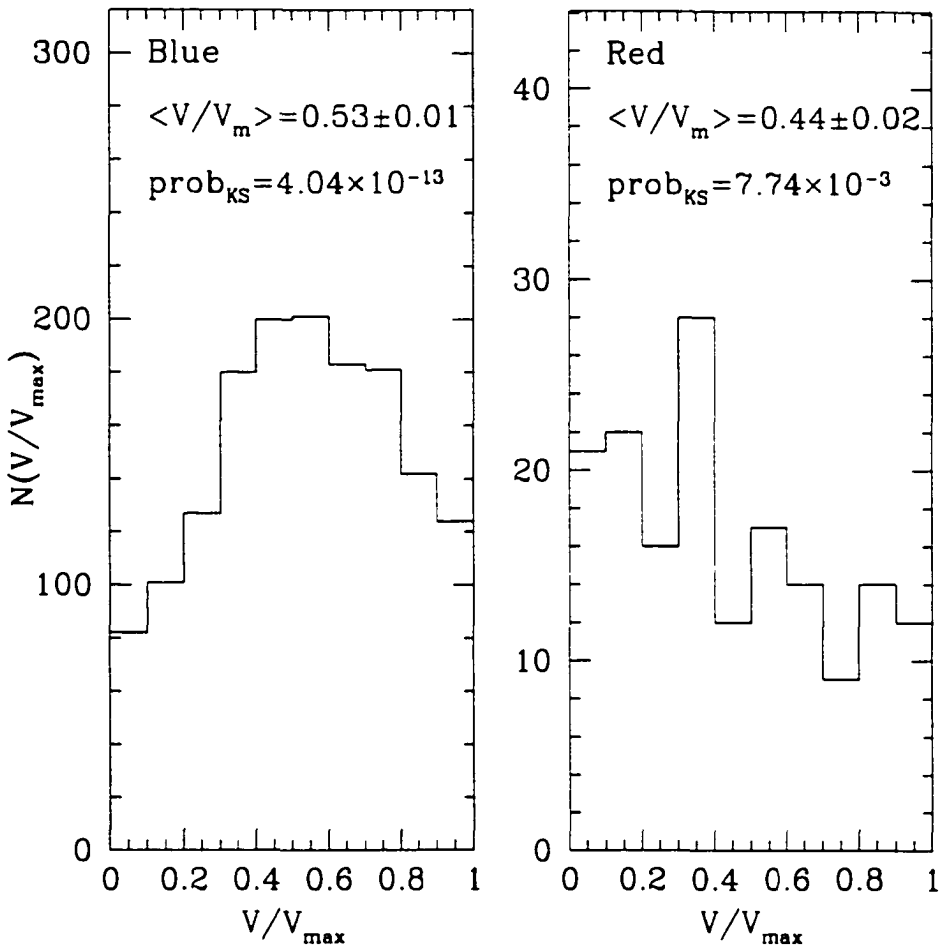

Figure 6.1: V/V_{max} distributions for sub-samples split by colour.

6.2 B band luminosity and luminosity density functions

The B band luminosity functions (LF's) were generated using the $1/V_a$ method described at length in Chapter 5. The accessible volumes were calculated in exactly the same way, using the $I_{ST} = 28$ limit but ignoring the effects of surface brightness. The Eddington corrections described in Section 5.6 were applied as before. Absolute B_{AB} magnitudes were calculated in the same manner as the 2500Å magnitudes were calculated, using the appropriate k-corrections derived from the templates. The main difference is that the sample was split by colour. Figure 6.2 shows these luminosity functions.

The Hubble Deep Fields sample a relatively small volume at low redshift. Further, bright galaxies are relatively rare. Consequently, the bright end of luminosity functions measured in the HDF's at low redshift are not well-defined. To remedy the situation, the LF's were supplemented by luminosity functions measured from the Canada-France Redshift Survey (Lilly *et al.*, 1995b, CFRS-VI). The "best" Schecter functions listed in Table 1 of CFRS-VI were shifted from H_0=50 km s^{-1}Mpc^{-1}to H_0=65 km s^{-1}Mpc^{-1}. The Schecter functions were only used in the absolute magnitude range in which they are valid. These CFRS luminosity functions were used independently of the HDF luminosity functions to measure the evolution of the number density, where one follows each absolute magnitude interval separately. On the other hand, to measure the evolution of the luminosity density, it is necessary to integrate over the function as a whole. For this purpose, the two luminosity functions were merged. In the case of overlap between the

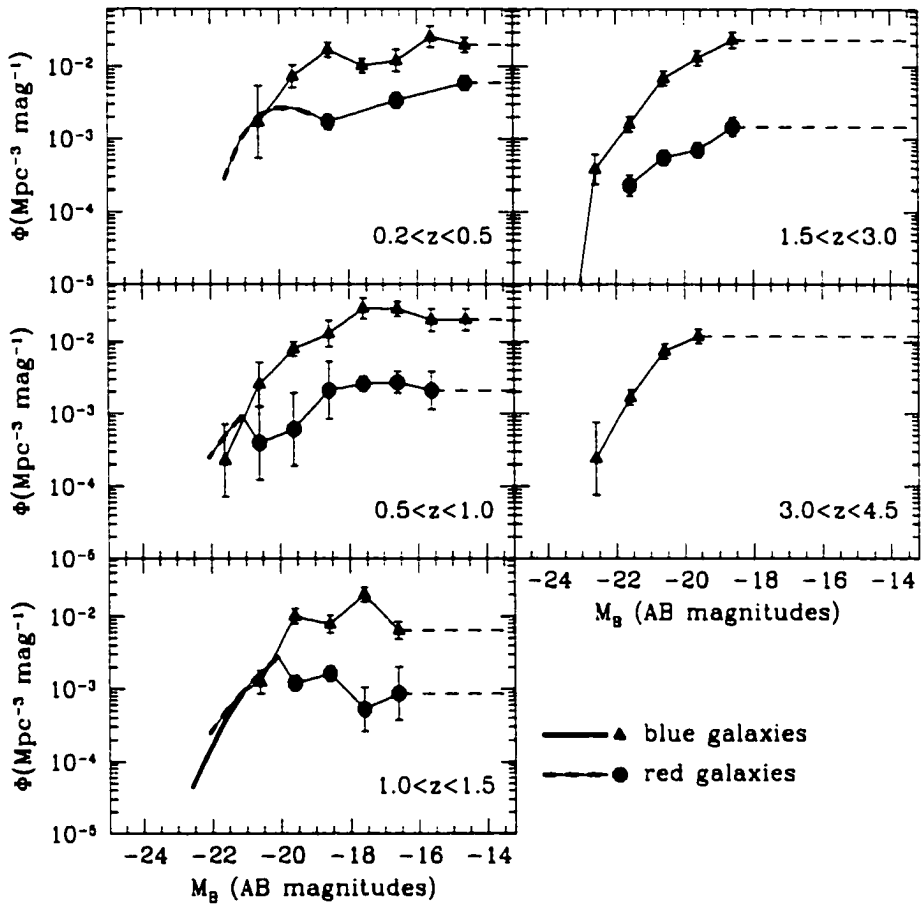

Figure 6.2: The B band luminosity functions for different redshift slices. The heavy lines at the bright ends of the lower redshift slices show the CFRS extensions. The dashed lines at the faint ends show an $\alpha = -1$ extrapolation.

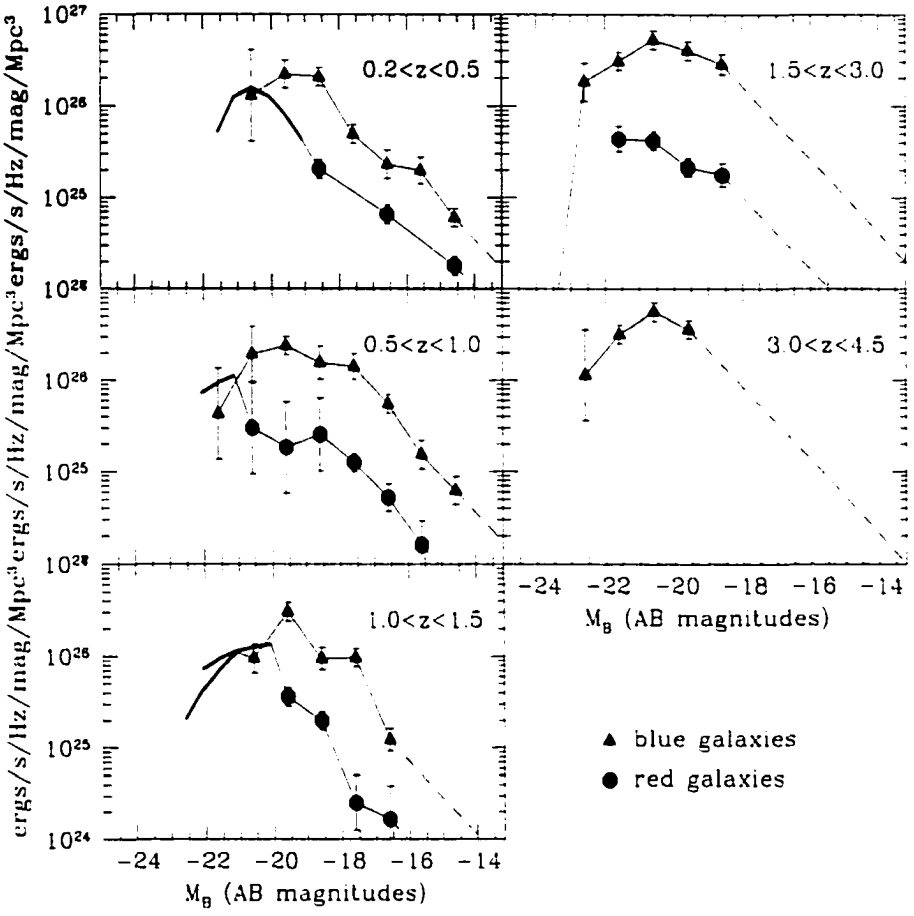

Figure 6.3: The B band luminosity density functions for different redshift slices. The heavy lines at the bright ends of the lower redshift slices show the CFRS extensions. The dashed lines at the faint ends show an $\alpha = -1$ extrapolation.

HDF luminosity functions and those from the CFRS, the former were used. Figure 6.2 shows the extensions to the HDF luminosity functions as heavy lines. At the faint end, the luminosity functions were extended by assuming a Schecter function with $\alpha = -1$; that is to say, the LF was assumed to be flat.

The B band luminosity functions were converted into luminosity density functions by multiplying the luminosity function by the flux corresponding to each absolute magnitude, as described previously in Section 5.8. Figure 6.3 shows the luminosity density functions. Now the importance of extending the HDF luminosity functions brightwards with the CFRS luminosity functions becomes apparent. Especially in the lowest redshift bin, the peak of the luminosity density function — which contributes the most to the integrated luminosity density — lies in the CFRS extension. At high redshift, the details of the extrapolation at the faint end of the luminosity density function have a small effect but are not particularly important. Assuming $\alpha = -1.5$ instead of $\alpha = -1$ changes the integrated luminosity density by 25%. For the lower redshift bins, changing the extrapolation has no significant effect.

Integrating over the B band luminosity density function, one obtains the total luminosity density. As mentioned earlier, both the HDF and CFRS luminosity functions are combined to get the luminosity density. Figure 6.5 shows the evolution of luminosity density with redshift. Least-squares fits to the data are shown. The luminosity density due to blue galaxies increases with redshift, while that from red galaxies decreases with redshift. Overall, the total B band luminosity density drops by a factor of ~ 2.5, from $z = 5$ to $z = 0.2$, as calculated from the fit.

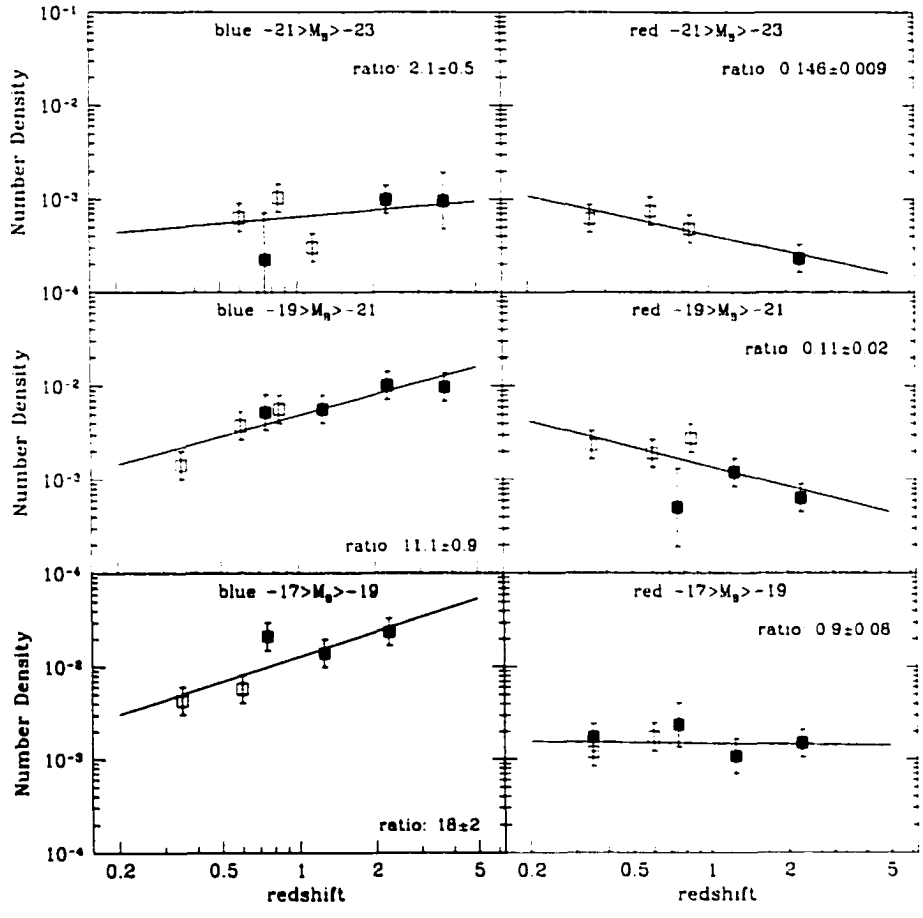

Figure 6.4: The evolution of B band number density of galaxies per cubic megaparsec from z=5 to z=0.2 for red and blue galaxies in three different absolute magnitude bins. The solid symbols are from this work, based on the HDF's. The open symbols are from the CFRS. The lines show linear fits to the data. The ratio of the number of galaxies at z=5 over that at z=0.2 as determined from the linear fit is shown for each colour/magnitude bin.

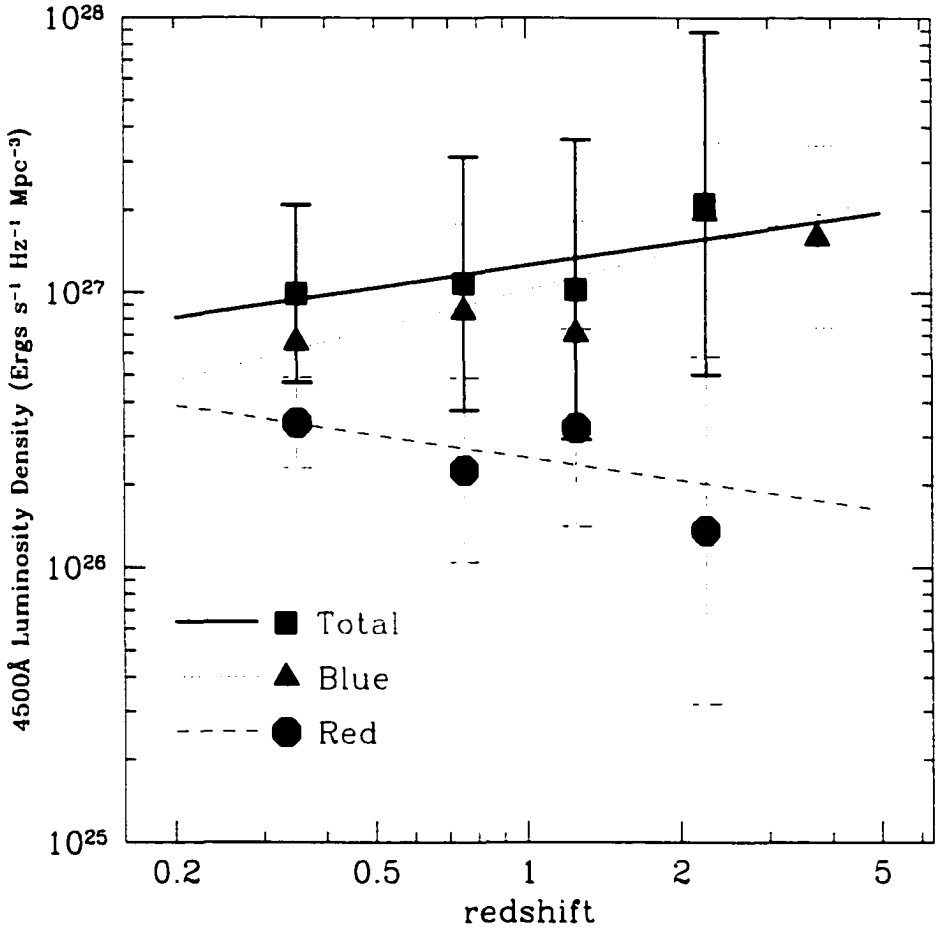

Figure 6.5: The evolution of B band luminosity density from z=5 to z=0.2. The data points show measured luminosity density from the combined HDF and CFRS luminosity functions. The lines are linear fits to the data. The squares and the heavy solid line show the total luminosity density, the triangles and the dotted line show the luminosity density of blue galaxies, and the circles and the dashed line show that of red galaxies. Overall, B band luminosity density drops by a factor of ~ 2.5.

To better trace the evolution of the number density of galaxies, one must plot the luminosity functions in slightly different way. Normally, luminosity functions are shown as number density plotted against absolute magnitude for various redshift cuts, as shown in Figure 6.2. Instead, one should plot number density against redshift for various absolute magnitude cuts. Figure 6.4 shows the evolution of number density in this way. The left-hand panels show the number density of blue galaxies steadily increasing with redshift, while the right-hand panels show that the red galaxies are steadily decreasing in number at higher redshifts. Each panel shows a least-squares fit to the data. The ratio of number density of galaxies at $z = 5$ over that at $z = 0.2$ as determined from the fit is also noted in each panel.

6.3 Interpretation

There are three processes affecting the number and luminosity density of galaxies, as illustrated schematically by Figure 6.6:

- **Merging** converts two fainter galaxies into a single brighter one. Merging causes a drop in the number of distinct galaxies but does not cause a drop in the total luminosity density. In an individual merger, the number of galaxies involved goes from two to one, but no stars are lost so the net effect on the luminosity density is nil. Indeed, if there is merger-induced star formation, the total luminosity of the final product will increase.

- **Fading** changes a bright galaxy into a fainter one. Disk galaxies will fade as they deplete their reservoir of gas and their star formation

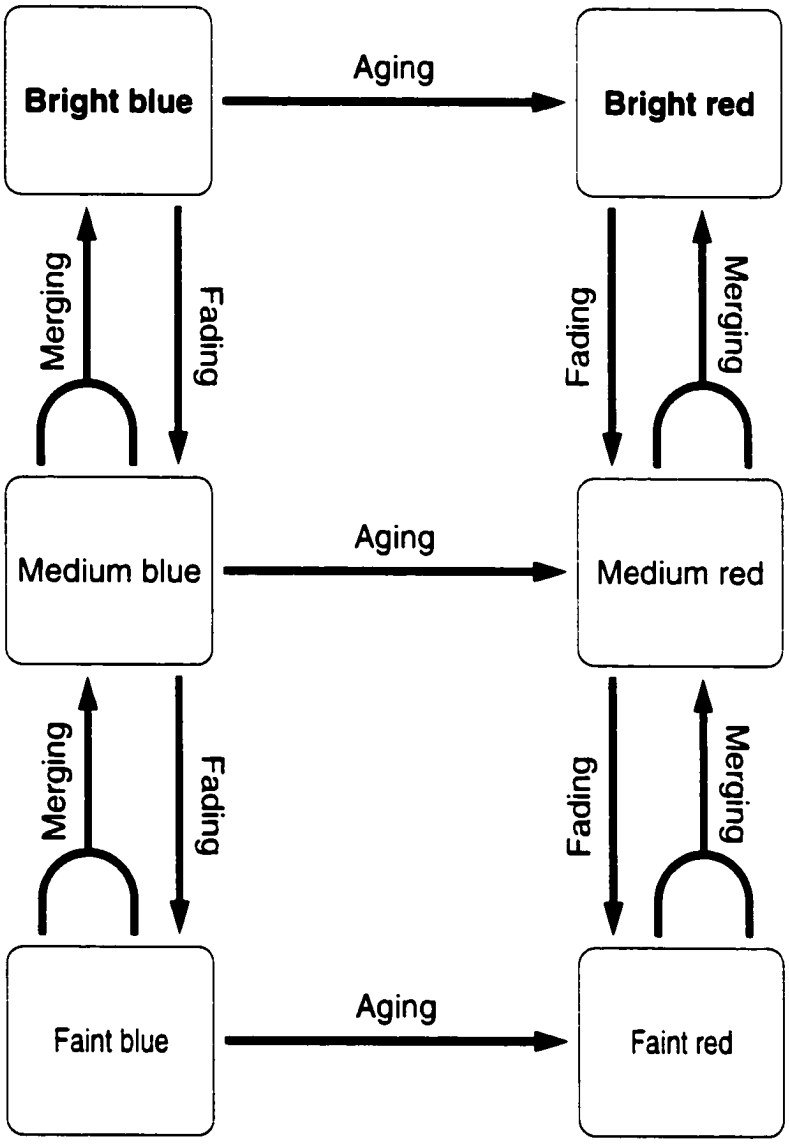

Figure 6.6: The processes of galaxy evolution

rates fall. A galaxy with a simple, single burst population will fade more rapidly as its more massive stars die off. Fading decreases the total luminosity density, but leaves the total number density of galaxies intact.

- **Aging** turns a blue galaxy into a red galaxy. Aging will occur when a galaxy is stripped of gas and dust and can no longer form new stars.[2] Aging increases the number density of red galaxies at the expense of blue galaxies. Aging and fading are different aspects of the same process: as galaxies become redder through aging, they will also become fainter.

Clearly, fading and aging must be occurring to some degree. On the whole, galaxies cannot continuously pump out stars at a constant rate for all time. Even if individual galaxies brighten due bursts of star formation, and even if the star formation rates of some galaxies remain relatively constant over the age of the Universe, Figure 6.5 shows that the total amount of B band light from all galaxies has decreased by a factor of two or three since $z = 5$. Therefore, some fading is occurring.

Further, the amount of B band light from blue galaxies has decreased by a factor of three or four since z=5, while the light from red galaxies is increasing, from no measurable light at z=5 to about a third of the total at low redshift. Therefore some aging is occurring. Plausibly, reverse processes

[2]Note that not all such evolved galaxies are elliptical in morphology. Even if a galaxy has a significant disk, as long as its red bulge dominates (*ie.* it is of type Sbc or earlier) it will still be classified as a red galaxy.

may be occuring too. Old red galaxies may be rejuvenated by starbursts and become bluer. The net trend, however, is that galaxies are growing older.

Some merging must be occurring too. The brightest blue galaxies (the top left panel of Fig. 6.4) do not appear to evolve in number density at all. Since they are being depleted by aging and fading, their numbers must be replenished at the same rate by the merging of fainter blue galaxies.

The fainter blue galaxies show a significant drop in number. Although some fading is occurring, as evidenced by the factor of three drop in luminosity density of the overall population shown in Figure 6.5, the drop in number density of individual objects is greater still: a factor of 8 to 18, as shown in the lower left-hand panels of Figure 6.4. Some aging is occurring too: the red galaxies in the corresponding magnitude bins are steadily increasing. But their numbers are relatively small (note the log scale) and should not have a large effect on the numbers of blue galaxies. Therefore, the fainter blue galaxies are being depleted by merging.

The red galaxies show a ten-fold increase in numbers since $z = 2$ (the highest redshift at which red galaxies are measurable). However merging also affects the red galaxies: the faintest magnitude bin remains almost constant, even though it must be gaining some galaxies through the aging of blue galaxies.

It is worth noting that, locally, the brightest red galaxies have the same absolute magnitudes as their blue counterparts: $M_B = -23$. According to the PEGASE galaxy stellar population models (Fioc & Rocca-Volmerange, 1997), as a galaxy with a simple, single burst population changes in colour

from blue to red it will fade by 2 magnitudes.[3] Therefore, if red galaxies formed solely through the aging of blue galaxies, there would have to be a population of $M_B = -25$ bright blue galaxies, because aging also implies a fading of 2 magnitudes. Thus it would take 7 or so of the brightest $M_B = -23$ progenitors to produce one of the brightest present day red galaxies. Alternatively of course, the progenitors of the brightest elliptical galaxies could be single, massive objects whose B band light is almost completely absorbed by dust. These objects would be visible at submillimetre wavelengths but not in the optical. However, Adelberger & Steidel (2000) have shown that the vast majority of the observed 850μm flux can be attributed to fairly normal galaxies that can be detected in the UV.

The balance is different for the different absolute magnitude bins. The change in number density is greater for the faintest galaxies in the sample, those with magnitude $-17 > M_B > -19$, than for the galaxies with $-19 < M_B < -21$. This suggests that merging affects the number density of smaller galaxies more than the larger galaxies. However, this does not necessarily mean that faint galaxies are involved in more mergers. Since mergers turn two fainter galaxies into a brighter one, the brighter magnitude bins gain at the expense of the fainter bins.

These qualitative statements can be put on a more quantitative footing with a simple model. The basic idea is to replace each of the boxes in the diagram in in Figure 6.6 with the number density, N, of an absolute

[3]Here "from blue to red" means from a typical blue galaxy, of type Im ($B - R$=0.5 in the Vega system, $V - I_{AB}$=0.17) to the corresponding typical red galaxy, an Sa ($B - R$=1.5 Vega, $V - I_{AB}$=0.70).

magnitude bin and replace each of the arrows in the diagram with a rate-of-change term, dN/dt, in a differential equation describing the evolution of galaxies. An arrow leaving a box means a decrease in the number density in that absolute magnitude bin; an arrow entering a box means a corresponding increase.

Assume the following:

- A merger causes two galaxies of the same magnitude to become a single object that is 0.75 (=2.5 log(2)) magnitudes brighter.
- All galaxies fade at the same rate — that of the decrease in total luminosity density.
- Aging can be described simply as the movement of a galaxy from a blue bin to a red bin and is independent of fading. Further, the aging process remains constant with redshift.
- Initially, there are no red galaxies at all.

Then one can calculate a detailed balance. Note that only the forward processes (aging and fading) are considered. Including the reverse processes (rejuvenation and rebrightening through star bursts) is functionally equivalent to reducing the strength of the forward processes. Moving diagonally in Figure 6.6 is equivalent to a vertical (fading/brightening) move followed by a horizontal (aging/rejuvenation) move.

Brightening and fading are, of course, incremental processes. Reconciling this with the discrete magnitude bins is handled in the following way: If a process causes a change in magnitude of δM and the bins are ΔM wide, then

a fraction $\delta M/\Delta M$ are deemed to have moved into the next bin and the rest $(1 - \delta M/\Delta M)$ are deemed to remain in the original bin.

Formally:

- let N_{b22} be the number of blue galaxies with $-23 < M_B < -21$.
  let N_{b20} be the number of blue galaxies with $-21 < M_B < -19$.
  let N_{b18} be the number of blue galaxies with $-19 < M_B < -17$.
  let N_{r22} be the number of red galaxies with $-23 < M_B < -21$.
  let N_{r20} be the number of red galaxies with $-21 < M_B < -19$.
  let N_{r18} be the number of red galaxies with $-19 < M_B < -17$.

- let M be the merger rate for galaxies as measured in units of mergers per individual galaxy per gigayear or — equivalently — the fraction of the galaxy population that undergoes a merger per Gyr. M depends on redshift:

$$M(z) = \begin{cases} M_0 \times (1+z)^3 & \text{if } z < 1 \\ M_0 \times 8 & \text{if } z \geq 1 \end{cases} \tag{6.3}$$

- let B, the brightening parameter, be the ratio of the increase in luminosity due to merging (measured in magnitudes) divided by the width of each magnitude bin. Since it is assumed that a galaxy doubles in brightness after a merger and the bins are 2 magnitudes wide, $B = 2.5\log_{10}(2)/2 \cong 0.38$.

- let F, the fading parameter, be the ratio of the decrease in luminosity (measured in magnitudes) per gigayear divided by the width of each magnitude bin. The global decrease in luminosity density from $z = 5.0$

to $z = 0.2$ is a factor of ~ 2.4 over a span of 6.9 Gyr. Since it is assumed that all galaxies fade at the same rate, $F = 2.5 \log_{10}(2.4)/6.9\mathrm{Gyr}/2 \simeq 0.069\mathrm{Gyr}^{-1}$.

- let A, the aging parameter be the fraction per gigayear of blue galaxies that become old enough (or bulge-dominated enough) to be classified as red galaxies.

- let the age of the Universe, t, and redshift, z, be related by

$$t(z) = H_0 \int_0^{\frac{1}{1+z}} \left[\Omega/x - k_0 + \Lambda x^2\right]^{-1/2} dx, \text{ where } x = \frac{1}{1+z}. \quad (6.4)$$

A $H_0 = 65\,\mathrm{km\,s^{-1}Mpc^{-1}}$, $\Omega = 1$, $\Lambda = 0$ cosmology is assumed.

Then one has:

		Merging:			Fading:		Aging:	
		numeric losses	out to brighter	in from fainter	out to fainter	in from brighter	out to red	in from blue
$\frac{dN_{b22}}{dt}$	$=$	$-\frac{M}{2}N_{b22}$	$-B\frac{M}{2}N_{b22}$	$+B\frac{M}{2}N_{b20}$	$-FN_{b22}$		$-AN_{b22}$	
$\frac{dN_{b20}}{dt}$	$=$	$-\frac{M}{2}N_{b20}$	$-B\frac{M}{2}N_{b20}$	$+B\frac{M}{2}N_{b18}$	$-FN_{b20}$	$+FN_{b22}$	$-AN_{b20}$	
$\frac{dN_{b18}}{dt}$	$=$	$-\frac{M}{2}N_{b18}$	$-B\frac{M}{2}N_{b18}$	$+B\frac{M}{2}N_{b16}$	$-FN_{b18}$	$+FN_{b20}$	$-AN_{b18}$	
$\frac{dN_{r22}}{dt}$	$=$	$-\frac{M}{2}N_{r22}$	$-B\frac{M}{2}N_{r22}$	$+B\frac{M}{2}N_{r20}$	$-FN_{r22}$			$+AN_{b22}$
$\frac{dN_{r20}}{dt}$	$=$	$-\frac{M}{2}N_{r20}$	$-B\frac{M}{2}N_{r20}$	$+B\frac{M}{2}N_{r18}$	$-FN_{r20}$	$+FN_{r22}$		$+AN_{b20}$
$\frac{dN_{r18}}{dt}$	$=$	$-\frac{M}{2}N_{r18}$	$-B\frac{M}{2}N_{r18}$	$+B\frac{M}{2}N_{r16}$	$-FN_{r18}$	$+FN_{r20}$		$+AN_{b18}$

(6.5)

The five free parameters in this equation are the initial ($z = 5$) values of the number densities in each magnitude bin for the blue galaxies, N_{b22}, N_{b20} and N_{b18}, the aging parameter, A, and the merging parameter, M_0. For a given set of parameters, Equation 6.5 can be solved, predicting the evolution of the number density of galaxies as a function of redshift. In principle, since it is a system of first order linear differential equations, Equation 6.5 can be solved analytically using eigenfunctions for any fixed set of parameters. In practice, the equation was solved numerically using a fourth-order Runge Kutta method.

In reality, there are more than just 3 magnitude bins: the luminosity function extends to much fainter magnitudes. The number of galaxies in the next fainter bin ($-17 < M_B < -15$) is in fact included in these calculations (N_{b16} and N_{r16} in equation 6.5) but not compared to the observations. The exact values of N_{b16} and N_{r16} have almost no effect on the final results.

The 5-dimensional parameter space was explored thoroughly. For each point in the parameter space, the predicted number densities at different redshifts were compared to the observations shown in Figure 6.4. The difference between the predictions and the observations was quantified using a χ^2 statistic. The best values of the parameters are found by minimizing χ^2.

Figure 6.7 shows slices through the 5-dimensional parameter space. In each panel, one of the five parameters (N_{b22}, N_{b20}, N_{b18}, A, M_0) is varied throughout its range. For each panel, χ^2 is minimized with respect to the other four parameters and plotted on the vertical axis. Figure 6.7 allows one to examine the sensitivity of the fit to each of the parameters. The fit is relatively insensitive to initial ($z = 5$) values of the number densities, but

fairly sensitive to the evolutionary parameters A and M_0.

The best fit for the parameters gives χ^2=27. There are 34 data points in Figure 6.4 and five free parameter in Equation 6.5 so there are $34 - 5 = 29$ degrees of freedom. This means that the reduced χ^2 is $27/29 = 0.93$, reassuringly close to the expected value of 1. Figure 6.8 shows the best model fit to the data of Figure 6.4. The curves accurately describe the data within the uncertainties.

It is important to note that this simple description is not a "model" in the same sense as hierarchical clustering simulations are "models". For example, in the simple case where all galaxies have the same magnitude, and aging and fading can be ignored, Equation 6.5 simplifies to

$$\frac{dN}{dt} = -\frac{M}{2}N. \tag{6.6}$$

Which has the simple solution:

$$N(t) = N_0 e^{-M/2} \tag{6.7}$$

In this case, deriving the merger rate is quite simple. The ratio of the number density at two different epochs gives the merger rate. While Equation 6.5 is considerably more complex than Equation 6.6, the spirit is the same: the intent is to deduce the merger rate from the data, not to see if a given theory fits the data.

Figure 6.9 shows the relative importance of the different evolutionary effects for each colour-magnitude bin. Rate of change for each of the three processes, either positive or negative, is plotted against redshift. Rate of change is measured by the size of the relevant terms in Equation 6.5 for the

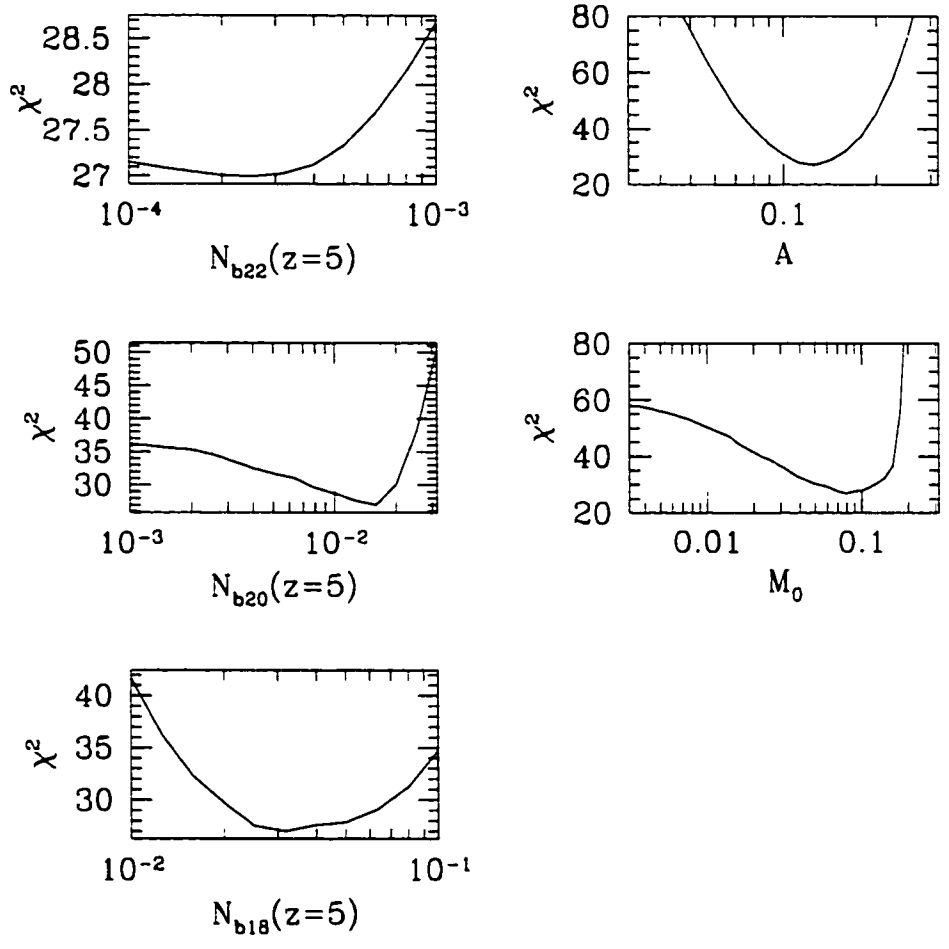

Figure 6.7: χ^2 minimization of the evolutionary parameters for Equation 6.5. In each panel, one parameter is varied systematically while χ^2 is minimized with respect to the other four. This minimal value of χ^2 is plotted against the parameter in question.

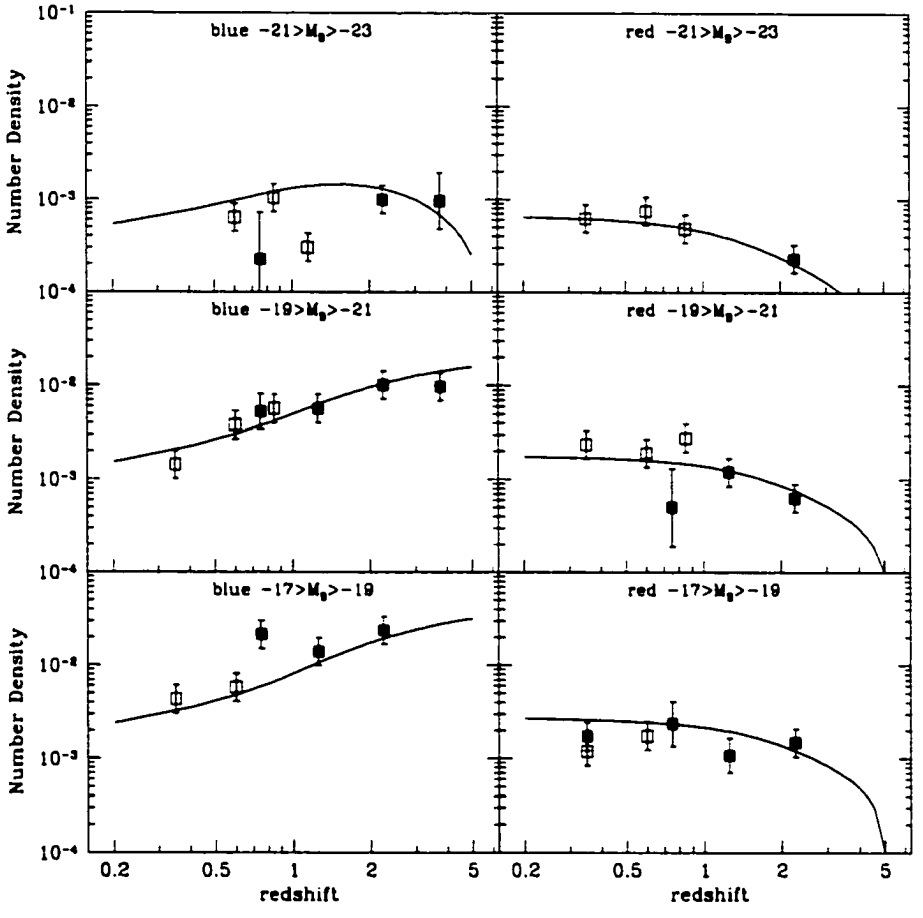

Figure 6.8: A model for the evolution of B band number density from z=5 to z=0.2. The symbols have the same meaning as Figure 6.4: the lines show the simple merging, fading and aging model described in the text.

best fitting parameters. For example, the negative merging terms for the brightest blue galaxies are $-\frac{M}{2}N_{b22} - B\frac{M}{2}N_{b22}$ while the positive fading term for the faintest red galaxies is $+FN_{r20}$. From Figure 6.9 it can be seen that merging (the solid line) is the dominant process, more important than either fading (dashed line) or aging (dotted line).

Integrating over the merger rate from $z = 5$ to the present, one finds that, on average, a present day galaxy is the product of 3.2 galaxies. This result is in line with analysis of the merger trees of the semi-analytic models of Taylor & Babul (in preparation) and Somerville *et al.* (2000). Taylor & Babul follow present day galaxies backwards in time, noting when a major merger occurs. A major merger is defined as one where the galaxy being accreted has a mass at least 50% of that of the main galaxy. Based on their results, a present day galaxy undergoes an average of 2.2 such mergers since z=6, implying the average number of progenitors is 3.2, remarkably similar to the observations. Figure 6.10 shows the distribution of the number of major mergers for 100 simulated galaxies. Somerville *et al.* (2000) followed dark matter halos in a similar fashion. Their Figure 6 shows the probability that a present day galaxy had N progenitors at z=2 as a function of N. The distribution has a mean of N=2.3 and peaks at N=2. Of course, these theoretical results from hierarchical clustering models are not directly comparable to the data at hand. The underlying assumption in deducing the merger rate from the data is that only galaxies of equal mass merge, while in the more detailed models, a range of galaxy masses are involved in a merger. Also note that it is the dark matter halos which are being followed in the merger trees, not the galaxies themselves, although one can assume that the galaxies themselves

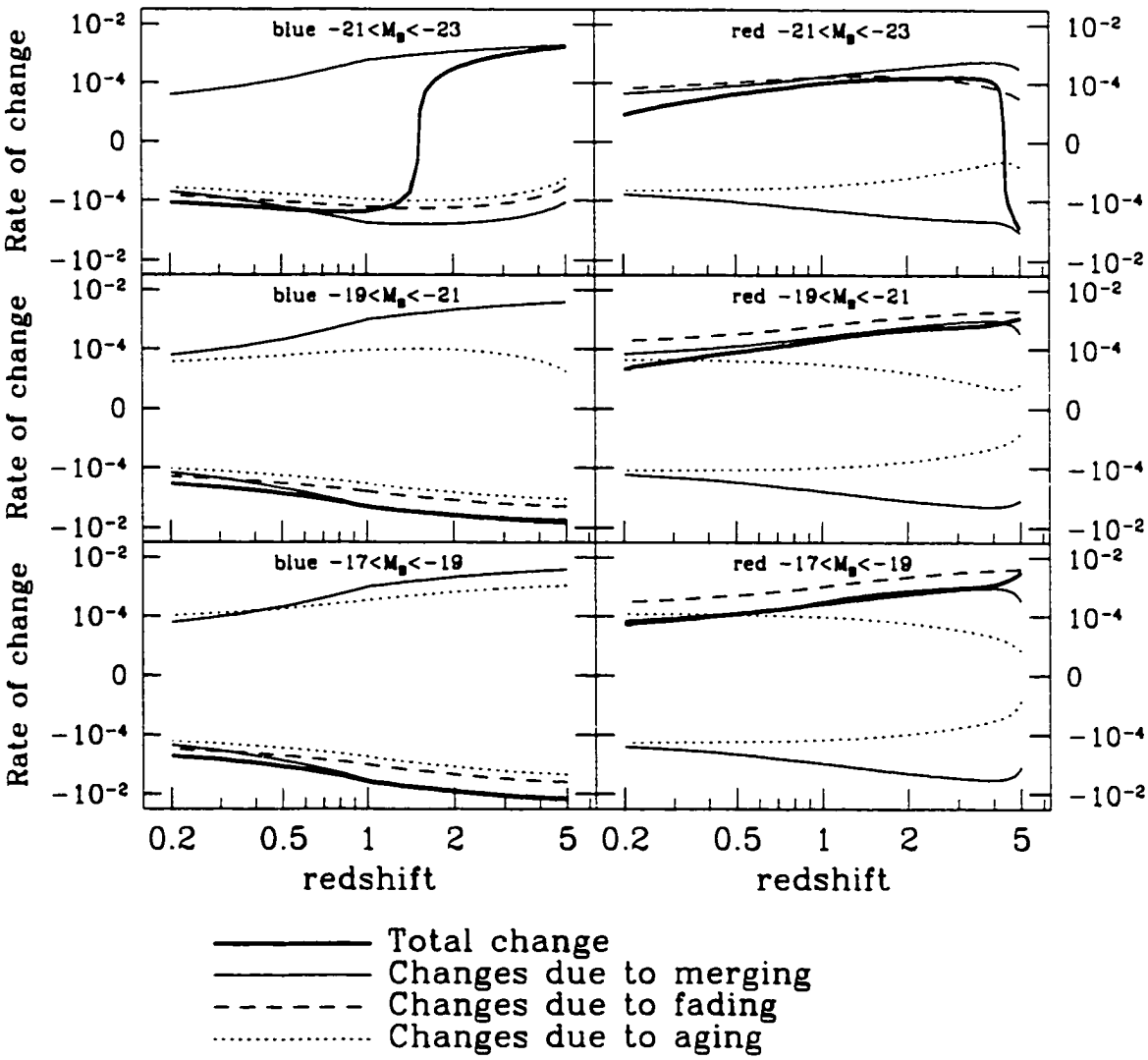

Figure 6.9: The relative importance of different evolutionary effects. The rate of change of the number density of galaxies in different magnitude bins is from the model plotted against redshift. The heavy solid line shows the overall rate of change. The thin solid line shows the rate of change due to merging. The dashed and dotted lines show the rate of change due to fading and aging respectively. Note the discontinuity in the vertical axis at zero.

merge shortly after their halos. Notwithstanding these caveats. the general agreement between the models and the data is interesting.

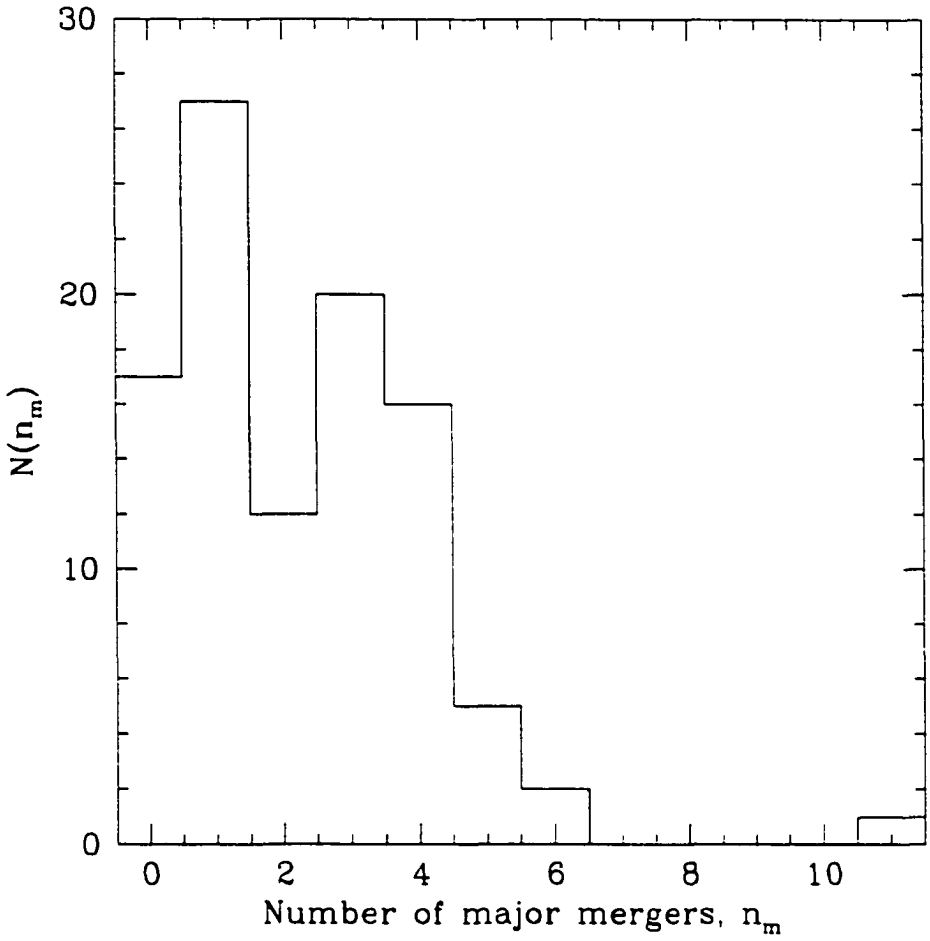

Figure 6.10: Merger frequency. Distribution of the number of mergers in the models of Taylor & Babul. 100 realizations of their models are shown.

Chapter 7

Morphologies

This chapter examines the evolution of the morphologies of galaxies. An objective measure of morphology, "lumpiness" (denoted L) is introduced. To avoid the observational effects caused by redshift, the $UBRI$ images of the Hubble Deep Fields are used to make rest B images of the fields by applying k-corrections on a pixel-by-pixel basis. L is then measured for the galaxies in this rest B image.

7.1 The L parameter

Traditionally, the appearance of galaxies, described by Hubble type, has been measured by eye. Expert observers would examine an image of a galaxy and classify its morphology based on various distinguishing characteristics (van den Bergh, 1998). Although these characteristics (presence/prominence of spiral arms, size of bulge, disturbed shape etc.) are generally agreed on by all the experts concerned, there is no way to quantify the Hubble type directly and objectively.

One aspect of the appearance of a galaxy that changes in a systematic way along the Hubble sequence is a galaxy's "lumpiness". Elliptical galaxies have a smooth appearance, while late type spirals have numerous knots of star formation. These knots are essentially local peaks in the spatial luminosity distribution of a galaxy. Hence, one can define a "lumpiness" parameter, L, as the number of local maxima associated with an object. An elliptical galaxy would have $L = 1$, while a star-forming galaxy with many HII regions might have $L = 50$. L is not an absolute number for a given galaxy. Different images of the same object may give different values of L as more lumps are revealed. For example, a higher resolution image or an image with a longer exposure time of the same galaxy may yield a higher value of L. This is not a concern, of course, for the Hubble Deep Fields where the image quality is consistent.

To measure L for a given galaxy image, one must decide what are the criteria that define a local maximum. That is to say, how many neighbouring pixels should be considered when measuring a local maximum and what is the minimum contrast that pixel must have with respect to its neighbours. Further, one must decide what parts of the image of a galaxy are actually associated with that galaxy and are not sky or parts of other nearby galaxies. To measure L for the Hubble Deep Field galaxies, two approaches were used:

In the first approach, the image is smoothed with a 5×5 kernel. Then, each pixel within the isophotes of the galaxy in question is examined in turn. Each pixel is deemed to be a local maximum if it is the brightest pixel in a 5×5 pixel area. The isophotes in question are those produced by SExtractor when the initial catalog was generated (see Chap. 2). This method is quite

simple but will not detect as lumps those maxima which lie near a galaxy in space, but not quite near enough on the image to be within its isophote.

The second approach is somewhat different. The image is processed using SExtractor with its deblending contrast parameter (see section 2.2) set to a very low level (10^{-8} instead of 0.005). This means that every luminosity enhancement is detected as a separate object. Note that, since SExtractor convolves the image with a kernel as part of the detection process, spurious noise peaks are not detected. To measure L for a given galaxy in the original (normally extracted) catalog, one adds up the number of detected objects that are near that galaxy. An object is "near" a galaxy in the original catalog if the difference in photometric redshifts is less than $\Delta z = 0.1$. Further, it must lie less than 15 kpc in projected separation from the catalog galaxy or lie within 15 kpc of an object which is "near" a catalog galaxy. That is to say, the neighbour-of-a-neighbour is also a neighbour. This method takes advantage of the fact that, for photometric redshifts, the internal scatter (z_{phot} to z_{phot}) is much lower than their external scatter (z_{phot} to z_{spec}).

Of course, since the deblending parameter has been set so low, many more objects will be detected, most of which will not be in the original catalog. To determine which galaxies are neighbours, photometric redshifts must be assigned. For the most part, these new objects lie within the isophotes of a galaxy in the original catalog. That is to say, it is not a new object but rather part of an old object which is now more segmented. In this case, the photometric redshift of the lump is just the same as the original galaxy. Less often, the newly-found lump is an object that lies outside the isophote of any galaxy in the original catalog. These galaxies were detected originally but

did not make the I=28 magnitude cut. For these objects, photometry was done using the same algorithm as described in Chapter 2 and photometric redshifts were generated as before. The quality of these second run photometric redshifts is generally poorer than those of the first run: the galaxies are fainter, and sometimes the object is not detected in all 4 bands. On a few occasions, it was impossible to determine a photometric redshift at all because the galaxy was only detected in the I band and the lower limit on its $R - I$ colour was not large enough to identify it as an R band dropout. However, since these galaxies are a small minority, the inclusion of these lower quality photometric redshifts in the analysis should not alter the final conclusions.

In this second method of determining L, all lumps near a given galaxy are counted properly; this justifies the additional complications. In particular, objects like those shown in Figure 4.4, which are not uncommon at high redshift, are properly described. In fact, although the two methods often give different values for L for the same galaxy, the overall conclusions on the evolution of morphology are the same, regardless of which method is used. Figure 7.1 shows four examples of this technique implemented on the I band image of the HDFN.

As a first test, the second method of measuring L was applied to the I band images of the two HDF's. Lumpiness was measured for each galaxy in the catalog described in Chapter 2. The galaxy catalog was split into three groups: galaxies with but a single local maximum, those with two to four local maxima and those with five or more. For each of these groups, number counts were calculated. Figure 7.2 shows the results. At bright magnitudes,

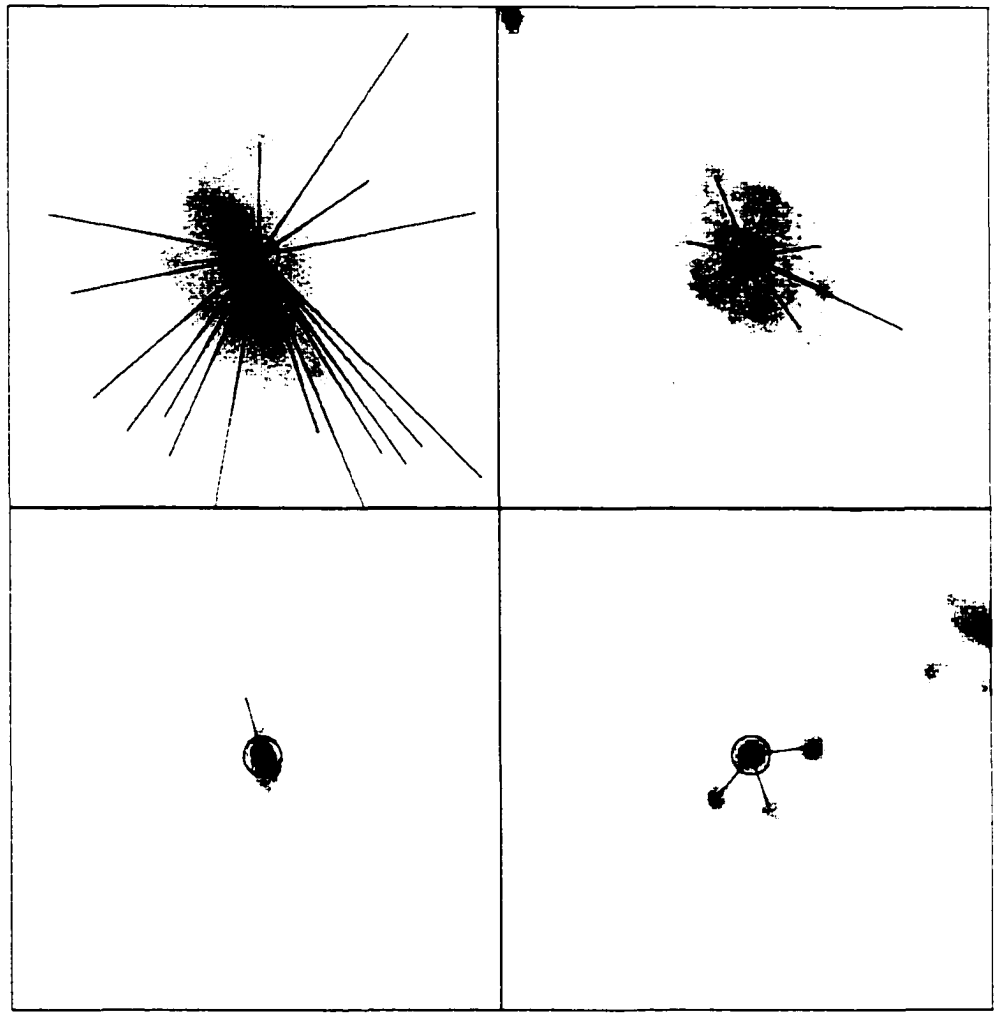

Figure 7.1: Four examples of lump finding and grouping. The circles show the central galaxy. The rays link the centre to the various sub-lumps. The redshifts of the objects are (clockwise from the upper left) z = 0.199, z = 0.089, z = 3.216, and z = 3.181.

most galaxies have multiple maxima. At faint magnitudes most have but a single maximum. The main conclusion to be drawn from this graph is that lumpiness correlates strongly with magnitude: bright objects are lumpier.

7.2 Rest B images

The problem with working solely within one observed band is that that band is sampling different parts of the spectrum at different redshifts. Since galaxies do not generally have the same appearance at different rest wavelengths, it is not valid to compare the morphology of galaxies viewed in the same band but at different redshifts. For example, an I band image of a galaxy at $z = 0$ shows that galaxy at ~ 8000Å. This wavelength is dominated by the light of older stars, which are, generally speaking, evenly distributed about the galaxy. At $z = 2$, the I band shows the galaxy at ~ 2700Å. At this wavelength, most of the light comes from tight knots of young stars and HII regions, lending the galaxy a much less regular appearance. Thus, a galaxy at $z = 0$ might have a lumpiness of $L = 1$, while the same galaxy viewed in the I band at $z = 2$ might have $L = 30$. Therefore, it highly desirable to construct a image where all the galaxies are viewed at the same wavelength.

The B band was chosen for much the same reasons discussed in Chapter 6. It represents the best compromise between straying too far into the UV where the light is dominated by transient features while limiting the required amount of extrapolation beyond the observed wavelengths.

To make a rest B band image of the Hubble Deep Fields, each pixel must be individually k-corrected to the B band based on its photometric redshift.

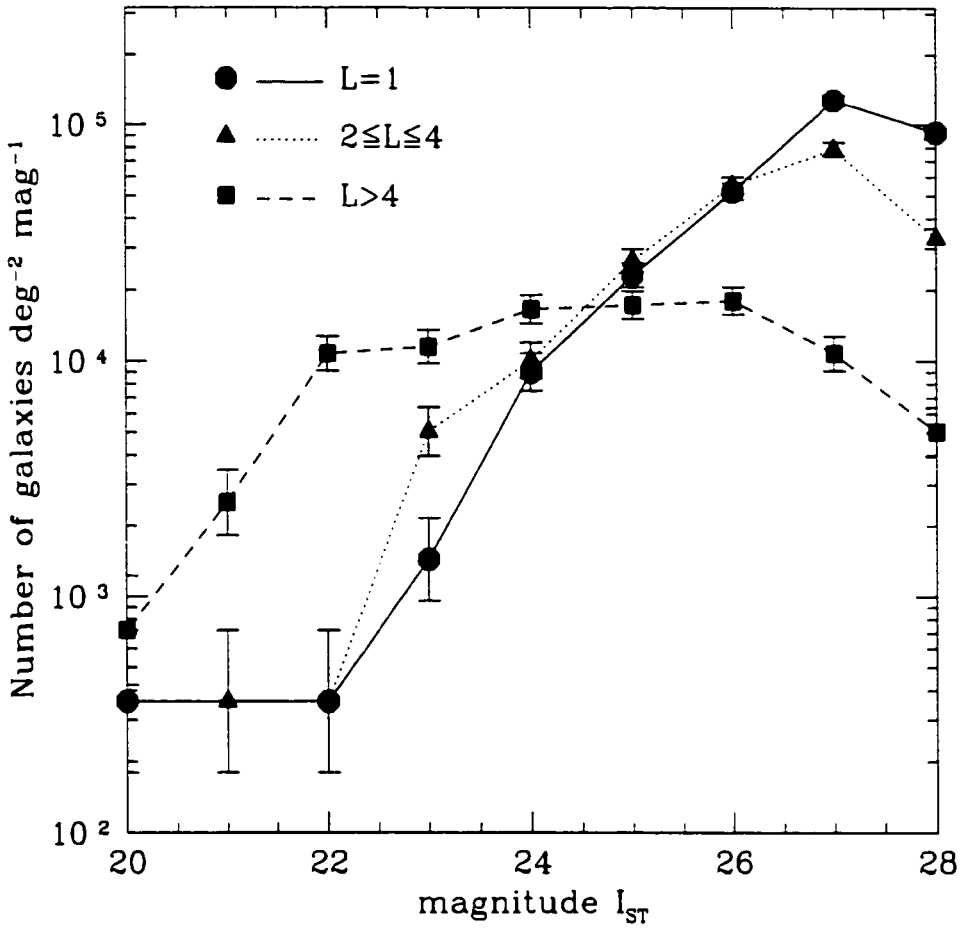

Figure 7.2: I band galaxy number counts split by "lumpiness", L. At faint magnitudes, the galaxy counts are dominated by galaxies with a single local maximum.

If a pixel lies within the isophote of a galaxy whose redshift is known, it is assigned that redshift. If a pixel does not lie within an isophote, it is assumed to be a sky pixel and is assigned a redshift of $z = 0$. Similarly, if a pixel lies within the isophote of a galaxy whose redshift is not known (for example if the galaxy was so faint a photometric redshift could not be measured) it is assigned a redshift of $z = 0$. If a pixel's redshift is $z = 0$, then it does not need to be k-corrected at all; here the observed B image is the same as the rest B image.

Several different methods of increasing complexity were tried in order to k-correct the non-zero redshift pixels. The simplest is to take the image of the galaxy in the band nearest the correct rest wavelength. Thus if the galaxy lies at $z = 0.89$, the B band image would be used; if the galaxy lies at $z = 0.35$ the $4500 \times (1 + 0.35) = 6075$Å or R band would be used. This method is robust in as much as it uses the original unmodified images. While ideal in this respect and also very simple, this method cannot be used beyond $z \sim 1$, when B shifts beyond the I band.

The next simplest method is to use the flux in each band at each pixel to construct a spectral energy distribution for that pixel. This SED can be transfered to the rest frame by dividing the wavelength of each band by $(1 + z)$. Given flux as a function of rest wavelength, one can interpolate or extrapolate as appropriate to the B band (4500Å). This is still fairly simple. However, Figure 5.1 shows that this is not always very accurate. As was shown in Section 5.3, k-correcting using template fitting is superior, if more complicated.

A template type must be determined for each pixel in order to make the

k-correction. A type is assigned at the same time the photometric redshift is measured for a galaxy. In principle, one could use this type to k-correct each pixel belonging to that galaxy. While this method is relatively simple, using it will not actually change the appearance of the galaxy in question. It will merely make the galaxy brighter or fainter as a whole, rather than smoothing out any peaks.

Therefore, it is necessary to determine a type for each pixel of each galaxy to determine the k-corrections. A spectral energy distribution was constructed for each pixel. The templates described in Section 3.3 were compared to this SED using χ^2 fitting. Redshift was not left as a free parameter; the fitting was done at the redshift of the galaxy.

Initially, only the flux of the pixel in question was used to determine the template. However, it was found that there is not always enough signal in a single pixel to determine a type robustly. Near the fringes of a galaxy in particular, sky noise can have a non-negligible effect on the flux of a single pixel, altering the SED — and hence the derived type — significantly. This shows up on the rest B images as isolated spikes, pixels with very different fluxes than their neighbours. Therefore, the average flux of the 9 nearest pixels (in a 3×3 grid) in each band are used to make the SED and this SED is used to determine the type of the central pixel. This smooths the k-corrections and eliminates the spikes. Note that the k-corrections could not meaningfully be determined on a smaller scale in any case since the FWHM of the HDF's is about 3.5 pixels. In some cases, even with the increased signal-to-noise, there was no measurable flux in two or more bands and a type could not be measured. In this case, the type of parent galaxy was used

to determine k-corrections for that pixel.

Once the template type was fit to the fluxes in a pixel, the rest B flux was determined by interpolating or extrapolating as required along the SED of the template to 4500Å. Finally, the $(1+z)^4$ surface brightness dimming correction was applied to each pixel. This whole procedure is analagous to determining the absolute magntiude for a galaxy as a whole. The template fitting k-correction procedure is the same in both cases and the $(1+z)^4$ term corresponds to the distance modulus.

Figure 7.3 shows an example of the rest B image. The original observed-frame B image is shown in the left panel and the rest-frame B image is shown in the right. The rest B image is noticably smoother and brighter. The galaxies are smoother, because rest B is redder than the observed frame. They are brighter because of the brightness dimming correction. Lyman break galaxies have large positive k-corrections: the galaxy at $z = 4.540$ lying near the right bottom corner of each panel in Figure 7.3 is invisible in observed B but is quite prominent in rest B.

7.3 Results

The lumpiness parameter was measured on the rest B images described in the previous section. Figure 7.4 shows the results for bright galaxies. It shows the lumpiness of each galaxy brighter than $I = 25$ (the limiting magnitude of Abraham *et al.* , 1996) as points. The median value of L is plotted as a heavy line. Based on this plot, the lumpiness of galaxies would appear to correlate strongly with redshift. The median value of lumpiness

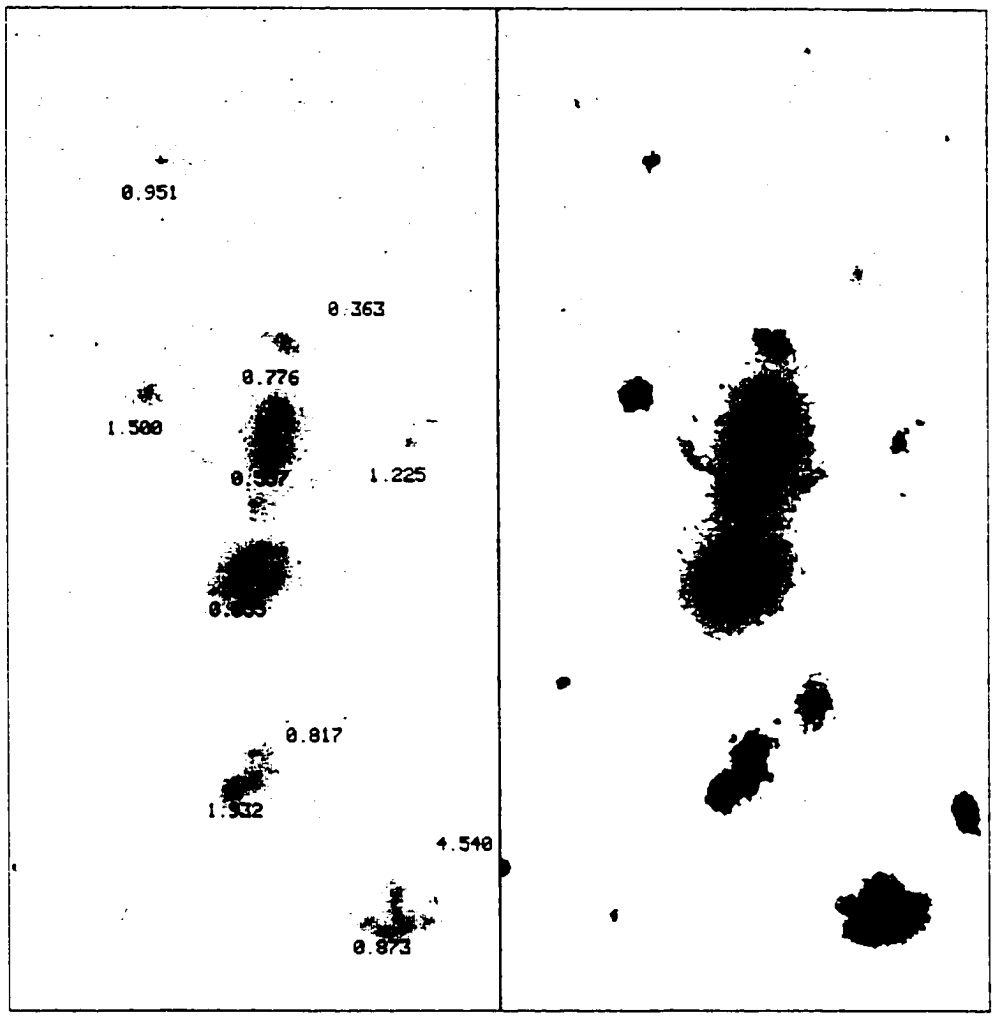

Figure 7.3: A section of the rest B image of the HDFN. The left panel shows the original, observed B, image while the right panel shows the rest B image of the same image section.

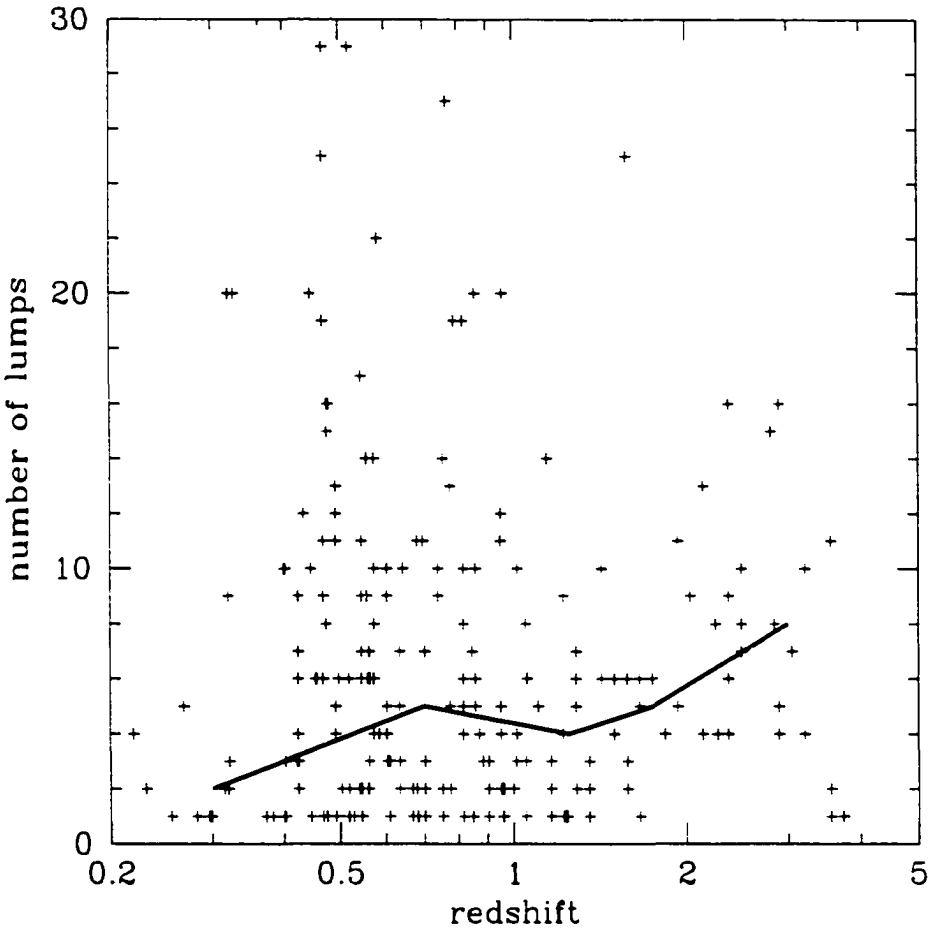

Figure 7.4: The lumpiness of galaxies as a function of redshift for $I < 25$. The points are individual galaxies. The heavy line shows the median lumpiness.

goes from $L = 2$ at low redshift to $L = 8$ at high redshift, a four-fold increase.

The correlation shown in Figure 7.4 is potentially misleading. The HDF sample is magnitude-limited. This means at each redshift a different range of absolute magnitudes will be present in the sample. At high redshifts, only the brightest galaxies will be present. These galaxies may or may not have the same value of L as their fainter counterparts. For example, bright galaxies will have a larger surface area and the potential for more local maxima. This will tend to exagerate the lumpiness at high redshifts.

In short, lumpiness is expected to increase with:

- increasing apparent brightness
- increasing absolute brightness
- increasing redshift.

That is to say $L = L(I, M_B, z)$. Since it is fairly difficult to view a four-dimensional surface, to disentangle these effects one must slice the sample by each of these three parameters and note the trends within each slice. The following three figures (Figs. 7.5, 7.6, 7.7) show slices of the four-dimensional surface.

Figure 7.5 shows the lumpiness of galaxies as a function of apparent I magnitude for different slices in redshift and in absolute B magnitude. Following the individual lines for each slice as denoted by the different symbols in each panel, one can see the correlation of L with apparent magnitude. Clearly, the brighter galaxies do indeed have higher values of L. This effect is purely an observational one.

Figure 7.6 shows the lumpiness of galaxies as a function of absolute B

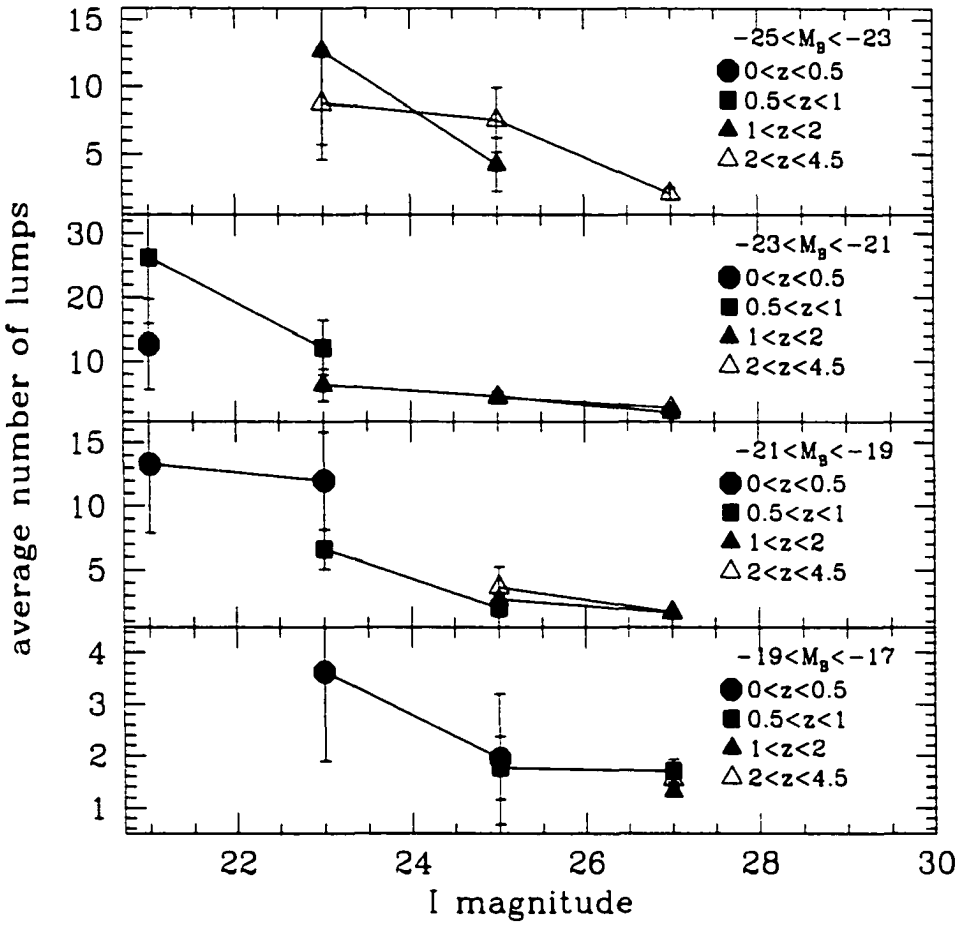

Figure 7.5: The lumpiness of galaxies as a function of apparent I magnitude. The different panels and point types indicate different absolute magnitude and redshift ranges, as labeled. By following lines from a single $z - M_B$ bin, it can be seen that lumpiness correlates with apparent magnitude. Brighter galaxies are lumpier.

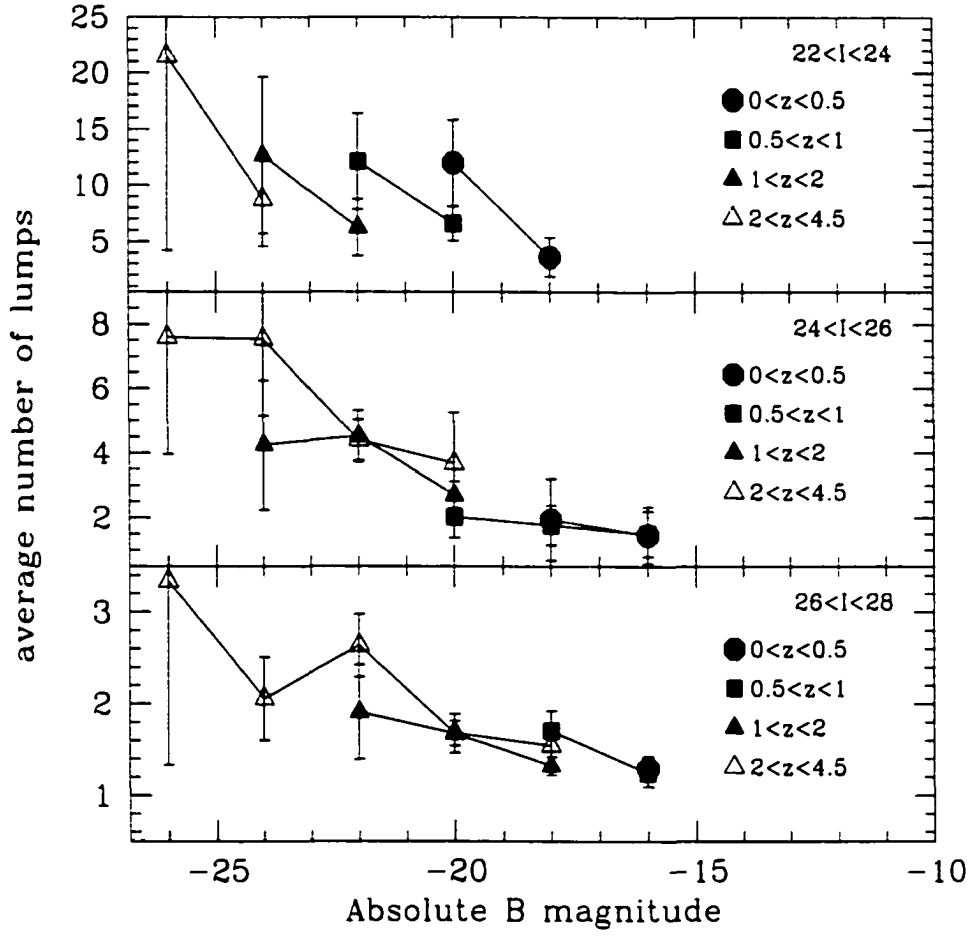

Figure 7.6: The lumpiness of galaxies as a function of absolute B magnitude. The different panels and point types indicate different apparent magnitude and redshift ranges, as labeled. By following lines from a single $z - I$ bin, it can be seen that lumpiness correlates with absolute magnitude. Brighter galaxies are lumpier.

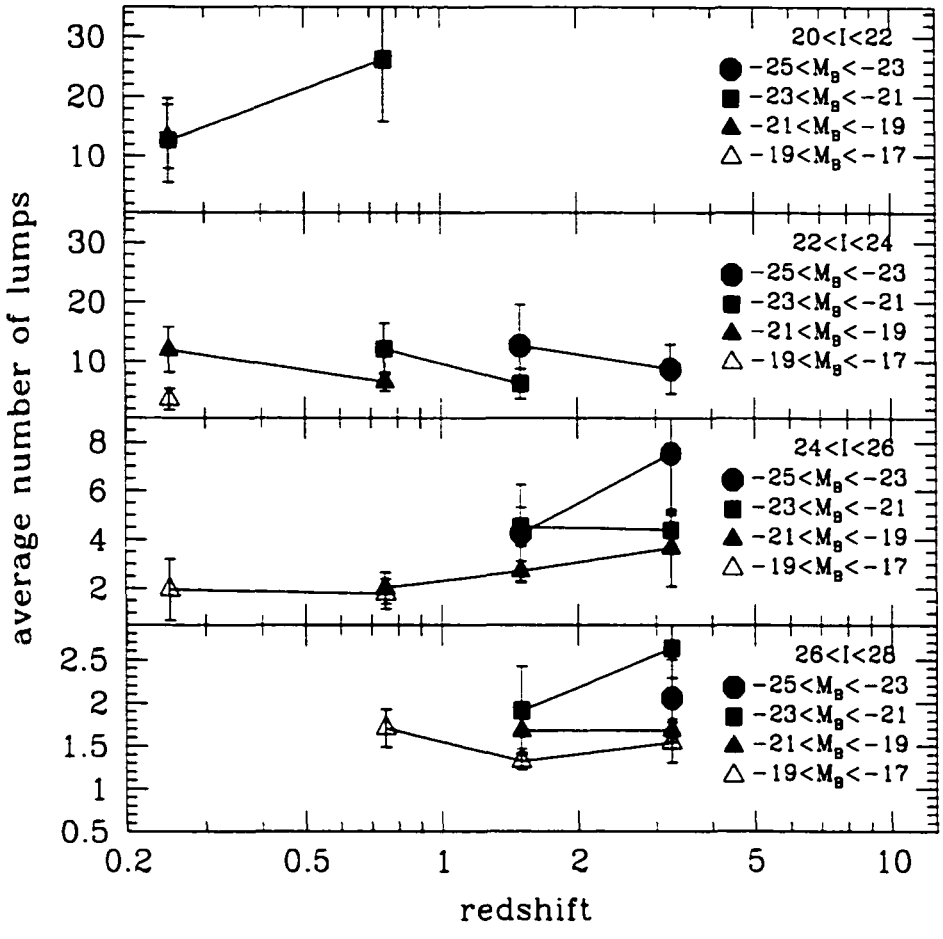

Figure 7.7: The lumpiness of galaxies as a function of redshift. The different panels and point types indicate different apparent magnitude and redshift ranges, as labeled. By following lines from a single $M_B - I$ bin, it can be seen that lumpiness correlates with redshift, albeit slightly. High redshift galaxies are lumpier.

magnitude for different slices in redshift and apparent magnitude. Again, by following each slice, one can see that at a given redshift and for given observational conditions, L correlates with absolute magnitude. Intrinsically bright galaxies are lumpier. Faint galaxies tend to be single compact sources.

Finally, Figure 7.7 shows the lumpiness of galaxies as a function of redshift for fixed slices in apparent and absolute magnitude. Overall, the trend of increasing lumpiness with increasing redshift is apparent. Galaxies at high redshift are more irregular than those at low z. This correlation, however, is not nearly as striking as it was in Figure 7.4. In particular, the trend in the $22 < I < 24$ panel suggests the reverse. Further, the intrinsically faintest galaxies ($-19 < M_B < -17$, shown by open triangles) show little trend with redshift. The bulk of these faint galaxies have $L = 1$. In short, although the trend for high redshift galaxies to have more disturbed morphologies is real, it is exaggerated by observational effects. When these effects are removed, the correlation is moderated considerably.

Chapter 8

Conclusion

8.1 Summary

The photometric redshift method was used in the HDF's down to a magnitude limit of I=28. The large sample and the unprecedented depth of the Hubble Deep Fields allow one to trace the evolution of several properties of galaxies from $z = 5$ to the present in a statistically significant manner. This thesis studied several such aspects.

The clustering of galaxies was examined by measuring the projected spatial correlation function. The clustering signal is rather weak in the small area of the Hubble Deep Fields except on the scale of individual galaxies. There is a slight increase in clustering around z=0.5 in the HDF-North relative to the HDF-South. When the redshift distributions of the HDFN and the HDFS are compared, one finds a significantly greater number of galaxies at this same redshift, which also shows as a very narrow peak in the spectroscopic redshift distribution. This suggests the presence of a structure (on the scale of a very weak cluster or a very strong group) in the HDF-North. The

size of this inhomogeneity is not out of line with the predictions of numerical simulations of structure formation.

The star formation rate density (SFRD) was determined by measuring the UV-luminosity density. After correcting for dust extinction, the star formation rate was found to decrease exponentially with time with an e-folding period of about 4 Gyr. This result, based on a single method of determining the SFRD and measured from a homogeneous sample extending from $z = 0$ to $z = 4.5$, is consistent with the various results in the literature, which are based on a wide variety of methods and samples at different redshifts. Further, three low-redshift samples of galaxies were used to study the dependence of the amount of dust extinction with galaxy type. Although there is considerable scatter, the average extinction is the same for all galaxy types.

The B band galaxy number and luminosity densities were studied simultaneously to examine the merging history of the Universe. While the total B band luminosity density of the Universe decreases only slightly with time since $z = 4.5$, the number density of galaxies drops considerably more. This difference in rates of declines makes it possible to quantify the merger rate. It was found that, on average, a present day galaxy is the product of ~ 3 progenitors.

The morphology of galaxies was quantified using a "lumpiness" parameter, L. L was measured on rest-frame, B band images made by k-correcting each pixel of each galaxy. It was found that L increases with increasing apparent brightness, increasing absolute brightness and increasing redshift. The first correlation is an observational effect while the second two are physically meaningful. While the brightest high redshift galaxies have disturbed

morphologies, the more typical object is more uniform and compact.

8.2 Future work

There are several obvious extensions to this thesis concerning high redshift galaxies and photometric redshifts:

8.2.1 Galaxies at $1 < z < 2$

Although over 300 redshifts for Lyman break ($z > 2$) galaxies have been measured by Steidel *et al.* (1998) and considerably larger number have been studied at $z < 1$, very few galaxies have been observed at intervening redshifts. The galaxies in this gap are interesting because they lie at a transition point in galaxy evolution. The galaxies at higher redshifts are all very young star-forming galaxies. Those at lower redshifts are more evolved objects. The galaxies at $z \sim 1$ are basically similar to those at $z = 0$, albeit slightly younger (on average) and hence bluer and brighter. While all galaxies at $z > 2$ are actively forming stars, many at $z \sim 1$ are already passively evolving. The intermediate redshift galaxies presumably are at an intermediate state of evolution. Of particular interest is when the first evolved (that is to say, non-star forming) objects appear.

Very few redshifts have been measured in this range because of the lack of spectral features in galaxies at these redshifts in the optical region used by most telescopes. Therefore, it is necessary to follow the usual lines used for redshift determination ([OII], [OIII] Balmer lines) into the infrared.

Infrared spectroscopy is considerably more time-consuming than optical

spectroscopy. Further, most galaxies do not lie at redshifts $1 < z < 2$. In any magnitude-limited sample, the bulk of galaxies lie at low redshift. It is necessary to separate the high redshift galaxies from these less interesting objects with photometric redshifts. Galaxies at higher redshifts ($z > 2$) are relatively easy to select. At those redshifts, intergalactic Hydrogen causes a very pronounced break in the SED's of galaxies which is easily measurable with broad band filters. Simple colour cuts are all that is required to select $z > 2$ galaxies. At lower redshifts one must use photometric redshifts to select one's sample.

This project was attempted (as part of this thesis) at CFHT using OSIS-IR multi-object spectroscopy. The required exposures were quite long (10 or so 45 minute integrations per mask). Regrettably, the bias level of the Red-eye detector used on this instrument was not stable over the long integrations and so the individual images could not be co-added. With the advent of infrared spectrographs on 8-metre telescopes, this project becomes much more feasible.

8.2.2 Dust at high redshift

Currently, most high redshift determinations of the SFRD (including those in Chapter 5) are made by measuring the UV flux of galaxies which is a measurement of the number of massive stars into those galaxies, which in turn is a measure of star formation. These measurements are susceptible to uncertainties due to dust obscuration of the UV light.

However, if Hα is observed, one can make a measurement of the star formation rate which is not subject to dust obscuration to nearly the same

degree. Further, if both the Hβ and the Hα line are observed it is possible to make a direct measurement of the dust obscuration, as discussed at length in Section 5.9

An application for time on NIRSPEC on Keck (through GEMINI) has been submitted for this project. Obviously, the small fraction of a night that will be available for this project on Keck is insufficient for an extensive survey. However, a small sample of galaxies in the Hubble Deep Field North has been assembled. The galaxies are chosen to have $K < 20.5$ and to have measured spectroscopic redshifts in the range $2 < z < 2.9$ (at higher redshifts, the Hα line is shifted into a region of greatly reduced atmospheric transmission). Further, the redshift has to be such that neither the Hα line nor the Hβ line lies on top of one of the OH night sky emission lines. Avoiding the night sky lines in this way dramatically decreases the required exposure times. There are 4 galaxies in the sample, two of which lie close enough to each other that they can be observed in a single pointing.

8.2.3 Large scale structure in the ACS parallel fields

When the Advanced Camera for Surveys (ACS) is installed on HST in 2001, one of its projects will be the ACS default pure parallel program (Sparks *et al.*, 2000). In this project, parallel observations will be made through the HST equivalents of the SDSS *griz* filters with the ACS while other HST instruments are making primary observations. This will generate a large number of fields comparable in depth to the Hubble Deep Fields. Potentially all of the aspects of galactic evolution investigated in this thesis (clustering, star formation, merging and morphology) could be further investigated in

these fields. Larger samples along several different lines of sight would greatly improve the study of each of these four galaxy properties. The absence of a U filter makes photometric redshifts slightly harder to measure at very low redshift. On the other hand, the presence the z (F850LP) filter makes it possible to follow the Balmer break in galaxies to higher redshifts.

In particular, one interesting result from this thesis is the difference in number counts and photometric redshift distributions between the HDF North and the HDF South described in Chapter 4. However, this pair of observations gives only a single measure of the variance. The large number of diverse lines of sight afforded by the ACS parallel program will greatly expand on this result. The number and redshift of these over dense regions is a measure of the evolution of the hierarchical clustering of galaxies. Currently, there are several theoretical N-body/semi-analytic model projects underway whose goal is to predict the amount of variation along such lines of sight (Colberg *et al.*, 1998, among many others). It will be very interesting to compare the results from the ACS fields with these simulations.

8.2.4 Improved spectral templates

As discussed in Section 3.2.2, one of the major problems when doing photometric redshifts is the lack of adequate templates. The ideal set of templates would:

1. span the full range of galaxy types, from the bluest irregulars to the reddest ellipticals,

2. have a large spectral range, from the K band to the Lyman break,

3. be empirical or at least accurately match the SED's of real galaxies.

Currently, the available sets of templates meet 2 out of 3 of these criteria. The theoretical templates (Bruzual & Charlot, 1993, for example) are available for a range of galaxy types and have excellent spectral coverage but do not always match the observed SED's. The empirical templates (Coleman *et al.*, 1980; Kinney *et al.*, 1993, for example) are available for many galaxy types but only extend bluewards to 1200Å and redwards to 10000Å.

Besides photometric redshifts, improved empirical templates would also be useful for:

1. Making galaxy number count predictions.

2. Comparing local galaxy SED's with those at high redshift.

3. Comparing with theoretical model galaxy spectra.

These ideal templates can be generated in two ways:

First, templates can be generated from observations of high redshift galaxies. Ironically, the UV spectra of high redshift galaxies have been studied more thoroughly than those of nearby galaxies because it has been shifted into the more easily observed optical region of the spectrum. The photometry of a high redshift galaxy can be converted into a observed-frame SED. If the redshift of this object is known, this SED can be converted into a rest-frame SED. By combining the rest-frame SED's of several galaxies at different redshifts, a library of SED's with full spectral coverage can be made. Multi-passband (*UBVRIJHK*) photometry is available for over 100 high-redshift galaxies with spectroscopic redshifts in the Hubble Deep Fields alone. There

are also numerous other surveys which can be incorporated into such a study. Note that the data set does not need to be homogeneous in any way. This means that archival data from many sources can be used.

Second, templates can be measured locally at the missing rest wavelengths. There exists a lot of broad-band photometric data in the infrared for local galaxies. This can be matched with the optical fairly easily although there are some concerns about correctly matching apertures. The UV portion is harder to measure directly since it cannot be measured from the ground. Some data from the Hopkins Ultraviolet Telescope have been published for elliptical galaxies (Brown *et al.*, 1997). Unpublished data (Ferguson 1999, private communication) is also available. Again, it is a question of carefully matching the photometric data from different spectral regions in order to produce a complete SED.

Bibliography

Abraham, R. G., Tanvir, N. R., Santiago, B. X., Ellis, R. S., Glazebrook, K., & van den Bergh, S.: 1996, *M.N.R.A.S.* **279**, L47

Adelberger, K. L. & Steidel, C. C.: 2000, *Astrophys. J.* **544**, 218

Barger, A. J., Cowie, L. L., & Richards, E. A.: 2000, *Astron. J.* **119**, 2092

Baum, W. A.: 1957, *Astron. J.* **62**, 6

Baum, W. A.: 1962, in G. C. McVittie (ed.), *Problems of extra-galactic research*, p. 390, IAU Symposium No. 15

Belloni, P. & Röser, H.-J.: 1996, *Astron. & Astrophys. Supp.* 118

Benítez, N.: 1998, *Bayesian photometric redshift estimation*, Preprint [astro-ph/9811189]

Benítez, N.: 1999, in R. Weymann, L. J. Storrie-Lombardi, M. J. Sawicki, & R. J. Brunner (eds.), *Photometric Redshifts & High Redshift Galaxies*, ASP Conference Series

Bershady, M. A., Majewski, S. R., Koo, D. C., Kron, R. G., & Munn, J. A.: 1997, *Astrophys. J. Let.* **490**, L41

Bertin, E. & Arnouts, S.: 1996, *Astron. & Astrophys. Supp.* **117**, 393

Brown, T. M., Ferguson, H. C., Davidsen, A. F., & Dorman, B.: 1997, *Astrophys. J.* **482**, 685

Brunner, R. J., Connolly, A. J., & Szalay, A. S.: 1997, *Towards more precise photometric redshifts: calibration via CCD photometry*, Preprint [astro-ph/9804195]

Bruzual, G. A.: 1983, *Astrophys. J.* **273**, 105

Bruzual, G. A.: 1985, *Rev. Mex. Astron. Astrof.* **10**, 55

Bruzual, G. A. & Charlot, S.: 1993, *Astrophys. J.* **405**, 538

Calzetti, D.: 1997, in *The Ultraviolet Universe at Low & High Redshift: Probing the Progress of Galaxy Evolution*, p. 403, astro-ph/9706121

Code, A. D., Holm, A. V., & Bottemiller, R. L.: 1980, *Astrophys. J. Supp.* **43**, 501

Cohen, J. G., Cowie, L. L., Hogg, D. W., Songaila, A., Blandford, R., & Hu, E. M.: 1996, *Astrophys. J. Let.* **471**, L5

Colberg, J. M., White, S. M. D., Macfarland, T. J., Jenkins, A., Frenk, C. S., Pearce, F. R., Evrard, A. E., Couchman, H. M. P., Efstathiou, G., Peacock, J. A., & Thomas, P. A.: 1998, in *Wide Field Surveys in Cosmology, 14th IAP meeting held May 26-30, 1998, Paris, Publisher: Editions Frontieres, ISBN: 2-8 6332-241-9, p. 247.*, p. 247

Coleman, G. D., Wu, C.-C., & Weedman, D. W.: 1980, *Astrophys. J. Supp.* **43**, 393

Colless, M. M., Ellis, R. S., Broadhurst, T. J., & Peterson, B. A.: 1993, *M.N.R.A.S.* **244**, 408

Colless, M. M., Ellis, R. S., Taylor, K., & Hook, R. N.: 1990, *M.N.R.A.S.* **244**, 408

Connolly, A. J., Csabai, I., Szalay, A. S., Koo, D. C., Kron, R. G., & Munn, J. A.: 1995a, *Astron. J.* **110**, 2655

Connolly, A. J., Szalay, A. S., Bershady, M. A., Kinney, A. L., & Calzetti, D.: 1995b, *Astron. J.* **110**, 1071

Connolly, A. J., Szalay, A. S., Dickinson, M. E., SubbaRao, M. U., & Brunner, R. J.: 1997, *Astrophys. J.* **486**, 11

Cowie, L. L., Clowe, D., Fulton, E., Cohen, J. G., Hu, E. M., , Songaila, A., Hogg, D. W., & Hodapp, K. W.: 1996, *Redshifts, colors & morphologies of the K selected galaxy sample in the Hubble Deep Field*, in preparation

Cowie, L. L., Songaila, A., & Barger, A. J.: 1999, *Astron. J.* **118**, 603

da Costa, L. N., Nonino, M., Rengelink, R., S. Zaggia, C. B., Erben, T., Wicenec, A., Scodeggio, M., Olsen, L. F., Guarnieri, M., E. Deul, S. D., Hook, R. N., Moorwood, A., & Slijkhuis, R.: 1998, *ESO Imaging Survey. Hubble Deep Field South: Optical-Infrared Observations, Data Reduction & Photometry*, submitted to Astronomy & Astrophysics

Dickinson, M. E.: 2000, *NICMOS observations of the HDFN*, in preparation

Dickinson, M. E., Bershady, M. A., Eisenhardt, P., Elston, R., Stanford, A., Connolly, A. J., Fazio, G., abd Mauro Giavalisco, H. C. F., Koo, D. C., Lauer, T., Postman, M., Steidel, C. C., Szalay, A. S., Tollestrup, E., Wright, N., & Wyckoff, E.: 1998, *Near Infrared Properties of the Hubble Deep Field*, in preparation

Driver, S. P. & Cross, N.: 2000, in R. C. Kraan-Korteweg, P. A. Henning, & H. Andernac (eds.), *Mapping the Hidden Universe*

Eddington, A. S.: 1913, *M.N.R.A.S.* **73**, 359

Eddington, A. S.: 1940, *M.N.R.A.S.* **100**, 354

Efstathiou, G., Ellis, R. S., & Peterson, B. A.: 1988, *M.N.R.A.S.* **232**, 431

Ellis, R. S., Couch, W. J., MacLaren, I., & Koo, D. C.: 1985, *M.N.R.A.S.*

217, 239

Ferguson, H. C. & McGaugh, S. S.: 1994, *Astrophys. J.* **440**, 470

Fernández-Soto, A., Lanzetta, K. M., & Yahil, A.: 1999, *Astrophys. J.* **513**, 34

Fioc, M. & Rocca-Volmerange, B.: 1997, *Astron. & Astrophys.* **326**, 950

Flores, H., Hammer, F., Thuan, T. X., Césarsky, C., Desert, F. X., Omont, A., Lilly, S. J., Eales, S., Crampton, D., & Le Fèvre, O.: 1999, *Astrophys. J.* **517**, 148

Fruchter, A. S. & Hook, R. N.: 1998, *A method for the linear reconstruction of undersampled images*, submitted to PASP [astro-ph/9808087]

Fukugita, M., Ichikawa, T., Gunn, J. E., Doi, M., Shimasaku, K., & Schneider, D. P.: 1996, *Astron. J.* **111**, 1748

Fukugita, M., Shimasaku, K., & Ichikawa, T.: 1995, *PASP* **107**, 945

Furusawa, H., Shimasaku, K., Doi, M., & Okamura, S.: 1999, *New improved photometric redshifts of galaxies in the HDF*, Preprint [astro-ph/9912447]

Gallego, J., Zamorano, I., Aragón-Salamanca, A., & Rego, M.: 1995, *Astrophys. J. Let.* **455**, L1

Giallongo, E., D'Odorico, S., Fontana, A., Cristiani, S., Egami, E., Hu, E., & McMahon, R. G.: 1998, *Astron. J.* **115**, 2169

Glass, I. S.: 1973, *M.N.R.A.S.* **164**, 155

Glazebrook, K.: 1998, in preparation

Glazebrook, K., Blake, C., Economou, F., Lilly, S., & Colless, M.: 1999, *M.N.R.A.S.* **306**, 843

Gwyn, S. D. J.: 1995, *Master's thesis*, University of Victoria

Gwyn, S. D. J. & Hartwick, F. D. A.: 1996, *Astrophys. J. Let.* **468**, L77

Hipparchus: 130 BC. *Commentary on Aratus & Eudoxus*. publisher unkown

Hogg, D. W., Cohen, J. G., Blandford, R., Gwyn, S. D. J., Hartwick, F. D. A., Mobasher, B., Mazzei, P., Sawicki, M. J., Lin, H., Yee, H. K. C., Connolly, A. J., Brunner, R. J., Csabai, I., Dickinson, M. E., SubbaRao, M. U., Szalay, A. S., Fernández-Soto, A., Lanzetta, K. M., & Yahil, A.: 1998. *Astron. J.* **115**, 1418

Hogg, D. W., Neugebauer, G., Armus, L., Matthews, K., & Pahre, M. A.: 1997. *Astron. J.* **113**, 474

Hogg, D. W., Neugebauer, G., Cohen, J. G., Dickinson, M. E., Djorgovski, S. G., Matthews, K., & Soifer, B. T.: 1999. *Three-micron imaging of the Hubble Deep Field*, accepted for publication in AJ

Hudson, M. J., Gwyn, S. D. J., Dahle, H., & Kaiser, N.: 1998. *Astrophys. J.* **503**, 531

Hughes, D. H., Serjeant, S., Dunlop, J., Rowan-Robinson, M., Blain, A., Mann, R. G., Ivison, R., Peacock, J., Efstathiou, A., Gear, W., Oliver, S., Lawrence, A., Longair, M., Goldschmidt, P., and Jenness, T.: 1998. *Nature* **394**, 241

Infante, L. & Pritchet, C. J.: 1995. *Astrophys. J.* **439**, 565

Johnson, H. L.: 1966. *Annual Review of Astronomy & Astrophysics* **4**, 193

Kennicutt, R. C.: 1998. *Annual Review of Astronomy & Astrophysics* **36**, 189

Kennicutt, R. C. J.: 1992. *Astrophys. J.* **388**, 310

Kinney, A. L., Bohlin, R. C., Calzetti, D., Panagia, N., & Wyse, R. F. G.: 1993. *Astrophys. J. Supp.* **86**, 5

Kinney, A. L., Calzetti, D., Bohlin, R. C., McQuade, K., Storchi-Bergmann,

T., & Schmidt, H. R.: 1996, *Astrophys. J.* **467**, 38

Kodama, T., Bell, E. F., & Bower, R. G.: 1999, *M.N.R.A.S.* **302**, 152

Koo, D. C.: 1985, *Astron. J.* **90**, 418

Kron, R.: 1980, *Astrophys. J. Supp.* **43**, 305

Landy, S. D. & Szalay, A. S.: 1993, *Astrophys. J.* **412**, 64

Lanzetta, K. M., Yahil, A., & Fernández-Soto, A.: 1996, *Nature* 386

Lilly, S. J., Fèvre, O. L., Hammer, F., & Crampton, D.: 1996, *Astrophys. J. Let.* **460**, L1

Lilly, S. J., Le Fèvre, O., Crampton, D., Hammer, F., & Tresse, L.: 1995a, *Astrophys. J.* **455**, 50

Lilly, S. J., Tresse, L., Hammer, F., Crampton, D., & Fèvre, O. L.: 1995b, *Astrophys. J.* **455**, 108

Liu, C. T. & Green, R. F.: 1998, *An optical multicolor system for measuring galaxy redshifts and spectral types*, Preprint [astro-ph/9806040]

Loh, E. D. & Spillar, E. J.: 1986a, *Astrophys. J. Let.* **307**, L1

Loh, E. D. & Spillar, E. J.: 1986b, *Astrophys. J.* **303**, 154

Loveday, J., Peterson, B. A., Efstathiou, G., & Maddox, S. J.: 1992, *Astrophys. J.* **390**, 338

Lowenthal, J. D., Koo, D. C., Guzmán, R., Gallego, J., Phillips, A. C., Vogt, N. P., Faber, S. M., Illingworth, G. D., & Gronwall, C.: 1997, *Keck Spectroscopy of Redshift $z \sim 3$ Galaxies in the Hubble Deep Field*, Preprint [astro-ph/9612239]

MacLaren, I., Ellis, R. S., & Couch, W. J.: 1988, *M.N.R.A.S.* **230**, 249

Madau, P.: 1995, *Astrophys. J.* **441**, 18

Madau, P., Ferguson, H. C., Dickinson, M. E., Giavalisco, M., Steidel, C. C.,

& Fruchter, A. S.: 1996, *M.N.R.A.S.* **283**, 1388

Madau, P., Pozzetti, L., & Dickinson, M.: 1998, *Astrophys. J.* **498**, 106

Maddox, S. J., Efstathiou, G., & Sutherland, W. J.: 1990, *M.N.R.A.S.* **246**, 433

McCracken, H. J., Metcalfe, N., Shanks, T., Campos, A., Gardner, J. P., & Fong, R.: 2000, *M.N.R.A.S.* **311**, 707

Meegan, C. A., Fishman, G. J., Wilson, R. B., Horack, J. M., Brock, M. N., Paciesas, W. S., Pendleton, G. N., & Kouveliotou, C.: 1992, *Nature* **355**, 143

Meurer, G. R., Heckman, T. M., & Calzetti, D.: 1999, *Astrophys. J.* **521**, 64

Miralles, J.-M., Pelló, R., & Le Borgne, J.-F.: 1996, *Photometric Analysis of the Hubble Deep Field*, Preprint

Mobasher, B., Rowan-Robinson, M., Georgakakis, A., & Eaton, N.: 1996, *The nature of the faint galaxies in the Hubble Deep Field*, Preprint [astro-ph/9604118]

Mould, J. R., Huchra, J. P., Freedman, W. L., Kennicutt, R. C., J., Ferrarese, L., Ford, H. C., Gibson, B. K., Graham, J. A., Hughes, S. M. G., Illingworth, G. D., Kelson, D. D., Macri, L. M., Madore, B. F., Sakai, S., Sebo, K. M., Silbermann, N. A., & Stetson, P. B.: 2000, *Astrophys. J.* **529**, 786

Osterbrock, D. E.: 1989, "*Astrophysics of gaseous nebulae & active galactic nuclei*", University Science Books, Mill Valley, California

Pascarelle, S. M., Lanzetta, K. M., & Fernández-Soto, A.: 1998, *Astrophys. J. Let.* **508**, L1

Patton, D. R.: 1999, *Ph.D. thesis*, University of Victoria

Pelló, R., Miralles, J.-M., Picat, J.-P., Soucail, G., & Bruzual, G. A.: 1996, *Identification of a high redshift cluster in the field of Q2345+007 through deep BRIJK' photometry*, Preprint [astro-ph/9603146]

Pence, W.: 1976, *Astrophys. J.* **203**, 39

Perlmutter, S., Aldering, G., Goldhaber, G., Knop, R. A., Nugent, P., Castro, P. G., Deustua, S., Fabbro, S., Goobar, A., Groom, D. E., Hook, I. M., Kim, A. G., Kim, M. Y., Lee, J. C., Nunes, N. J., Pain, R., Pennypacker, C. R., Quimby, R., Lidman, C., Ellis, R. S., Irwin, M., McMahon, R. G., Ruiz-Lapuente, P., Walton, N., Schaefer, B., Boyle, B. J., Filippenko, A. V., Matheson, T., Fruchter, A. S., Panagia, N., Newberg, H. J. M., Couch, W. J., & The Supernova Cosmology Project: 1999, *Astrophys. J.* **517**, 565

Poggianti, B. M.: 1997, *Astron. & Astrophys. Supp.* **122**, 399

Pogson, N. R.: 1856, *M.N.R.A.S.* **17**, 12

Ptolemy: 140, *Almayest*, publisher unkown

Rixon, G. T., Wall, J. V., & Benn, C. R.: 1991, *M.N.R.A.S.* **251**, 243

Salpeter, E. E.: 1955, *Astrophys. J.* **121**, 161

Sandage, A.: 1999, *Astrophys. J.* **527**, 479

Sawicki, M. J., Lin, H., & Yee, H. K. C.: 1997, *Astron. J.* **113**, 1

Sawicki, M. J. & Mallen-Ornelas, G.: 2001, in preparation

Scalo, J. M.: 1986, *Fundamentals of Cosmic Physics* **11**, 1

Schmidt, M.: 1968, *Astrophys. J.* **151**, 393

Schmidt, M., Higdon, J. C., & Hueter, G.: 1988, *Astrophys. J. Let.* **329**, L85

Seaton, M. J.: 1979, *M.N.R.A.S.* **187**, 73P

Somerville, R. S., Lemson, G., Kolatt, T. S., & Dekel, A.: 2000, *M.N.R.A.S.*

316, 479

Sparks, W., Postman, M., & Ferguson, H. C.: 2000, *ACS Default (Archival) Pure Parallel Program*, Instrument Science Report ACS 2000-02, Space Telescope Science Institute

Spinrad, H., Stern, D., Bunker, A., Dey, A., Lanzetta, K. M., Pascarelle, A. Y. S., & Fernández-Soto, A.: 1998, *A z=5.34 Galaxy Pair in the Hubble Deep Field*, Preprint [astro-ph/9809145]

Steidel, C. C., Adelberger, K. L., Dickinson, M., Giavalisco, M., Pettini, M., & Kellogg, M.: 1998, *Astrophys. J.* **492**, 428

Steidel, C. C., Adelberger, K. L., Giavalisco, M., Dickinson, M., and Pettini, M.: 1999, *Astrophys. J.* **519**, 1

Steidel, C. C., Giavalisco, M., Pettini, M., Dickinson, M. E., & Adelberger, K. L.: 1996a, *Astron. J.* **112**, 352

Steidel, C. C., Giavalisco, M., Pettini, M., Dickinson, M. E., & Adelberger, K. L.: 1996b, *Astrophys. J. Let.* **462**, L17

Steidel, C. C. & Hamilton, D.: 1993, *Astron. J.* **105**, 2017

SubbaRao, M. U., Connolly, A. J., Szalay, A. S., & Koo, D. C.: 1996, *Luminosity Functions from Photometric Redshifts I: Techniques*, Preprint [astro-ph/9606075]

Sullivan, M., Treyer, M. A., Ellis, R. S., Bridges, T. J., Milliard, B., & Donas, J. .: 2000, *M.N.R.A.S.* **312**, 442

Thompson, R. I., Storrie-Lombardi, L. J., Weymann, R. J., Rieke, M. J., Schneider, G., Stobie, E., & Lytle, D.: 1999, *Astron. J.* **117**, 17

Tresse, L. & Maddox, S. J.: 1998, *Astrophys. J.* **495**, 691

Tresse, L., Rola, C., Hammer, F., Stasinska, G., Le Fèvre, O., Lilly, S. J., &

Crampton, D.: 1996, *M.N.R.A.S.* **281**, 847

Treyer, M. A., Ellis, R. S., Milliard, B., Donas, J., & Bridges, T. J.: 1999, *M.N.R.A.S.* **300**, 303

van den Bergh, S.: 1998, *Galaxy morphology & classification*, Cambridge University Press

VandenBergh, D. A., Hartwick, F. D. A., Dawson, P., & Alexander, D. R.: 1983, *Astrophys. J.* **266**, 747

Villumsen, J. V., Freudling, W., & da Costa, L. N.: 1997, *Astrophys. J.* **481**, 578

Wang, Y., Bahcall, N., & Turner, E. L.: 1998, *A catalog of color-based redshift estimates for z<4 galaxies in the Hubble Deep Field*, Preprint [astro-ph/9804195]

Weymann, R., Storrie-Lombardi, L. J., Sawicki, M. J., & Brunner, R. J. (eds.): 1999, *Photometric Redshifts & High Redshift Galaxies*, A. S. P. Conference Series

Weynmann, R. J., Stern, D., Bunker, A., Spinrad, H., Chaffee, F. H., Thompson, R. I., & Storrie-Lombardi, L. J.: 1998, *Astrophys. J.* **505**, 95

Williams, R. E., Blacker, B. S., Dickinson, M. E., Dixon, W. V. D., Ferguson, H. C., Fruchter, A. S., Giavalisco, M., Gilliland, R. L., Heyer, I., Katsanis, R., Levay, Z., Lucas, R. A., McElroy, D. B., Petro, L. D., Postman, M., Adorf, H.-M., & Hook, R. N.: 1996, *Astron. J.* 112

Worthey, G.: 1994, *Astrophys. J. Supp.* 95

Yan, L., McCarthy, P. J., Freudling, W., Teplitz, H. I., Malumuth, E. M., Weymann, R. J., & Malkan, M. A.: 1999, *Astrophys. J. Let.* **519**, L47

Yee, H. K. C., Ellingson, E., & Carlberg, R. G.: 1996, *Astrophys. J. Supp.*

102. 269

Yee, H. K. C., Morris, S. L., Lin, H., Carlberg, R. G., Hall, P. B., Sawicki, M., Patton, D. R., Wirth, G. D., Ellingson, E., and Shepherd, C. W.: 2000, *Astrophys. J. Supp.* **129**, 475

Yoshii, Y. & Takahara, F.: 1988, *Astrophys. J.* **326**, 1

Zepf, S. E., Moustakas, L. A., & Davis, M.: 1997, *Astrophys. J. Let.* 474